1.0

2.8   2.5

3.2   2.2

2.0

1.1   1.8

1.25   1.4   1.6

MICROCOPY RESOLUTION TEST CHART

AD A098140

THE EFFECT OF INLET TURBULENCE AND STRUT
GENERATED DISTURBANCES ON TURBOMACHINERY
NOISE.

R. Trunzo

Technical Memorandum
File No. TM 80-197
25 Sep 80
Contract No. N00024-79-C-6043

Copy No. 38

The Pennsylvania State University
APPLIED RESEARCH LABORATORY
Post Office Box 30
State College, PA 16801

NAVY DEPARTMENT

NAVAL SEA SYSTEMS COMMAND

81 4 23,047

REPORT DOCUMENTATION PAGE		READ INSTRUCTIONS BEFORE COMPLETING FORM
1. REPORT NUMBER TM 80-197 ✓	2. GOVT ACCESSION NO. AD-A098 140	3. RECIPIENT'S CATALOG NUMBER
4. TITLE (and Subtitle) THE EFFECT OF INLET TURBULENCE AND STRUT GENERATED DISTURBANCES ON TURBOMACHINERY NOISE		5. TYPE OF REPORT & PERIOD COVERED Technical Memorandum
		6. PERFORMING ORG. REPORT NUMBER
7. AUTHOR(s) R. Trunzo		8. CONTRACT OR GRANT NUMBER(s) N00024-79-C-6043 ✓
9. PERFORMING ORGANIZATION NAME AND ADDRESS Applied Research Laboratory Post Office Box 30 State College, PA 16801		10. PROGRAM ELEMENT, PROJECT, TASK AREA & WORK UNIT NUMBERS
11. CONTROLLING OFFICE NAME AND ADDRESS Naval Sea Systems Command Washington, DC 20362		12. REPORT DATE 25 September 1980
		13. NUMBER OF PAGES 156
14. MONITORING AGENCY NAME & ADDRESS(If different from Controlling Office)		15. SECURITY CLASS. (of this report) UNCLASSIFIED
		15a. DECLASSIFICATION/DOWNGRADING SCHEDULE

16. DISTRIBUTION STATEMENT (of this Report)

Approved for Public Release. Distribution Unlimited
Per NAVSEA - Oct. 29, 1980.

17. DISTRIBUTION STATEMENT (of the abstract entered in Block 20, If different from Report)

18. SUPPLEMENTARY NOTES

19. KEY WORDS (Continue on reverse side if necessary and identify by block number)

thesis, turbomachinery, rotor, noise, aerodynamic, measurements

20. ABSTRACT (Continue on reverse side if necessary and identify by block number)

Results of an investigation in which turbomachine rotor sound spectra variations were correlated with aerodynamic measurements of the inlet turbulence strut wake, and vortex flow strength, are presented, in this thesis. Aerodynamic measurements that were made included mean velocity and turbulence intensity profiles, and the axial length scales. Inlet turbulence data indicate that the major effect of the flow contraction appears to be the elongation of atmospheric turbulent eddies from 20 cm to 200 cm. Eddies of this size

DD FORM 1473, EDITION OF 1 NOV 65 IS OBSOLETE
1 JAN 73

20. dominate the generation of blade passing frequency (BPF) noise. Reducing the eddy size by the use of a grid revealed the vortex flow strength to be the second major source of noise at BPF. A doubling of vortex flow strength produced a 6 dB increase in the source pressure level (SPL) of the first BPF. The variation of the SPL with the decay of the strut wake was small. The SPL showed less than a 2 dB change with a doubling of the wake turbulence intensity or the velocity defect. The measured sound spectra were compared with predicted trends from two different analyses. The results of this comparison further supported the conclusion that the strut wake structure was not as effective in producing noise at the vortex strength or the inlet turbulent eddies. A discussion of the relative importance of various sources of noise due to the flow field is given.

ABSTRACT

Results of an investigation in which turbomachine rotor sound
spectra variations were correlated with aerodynamic measurements of the
inlet turbulence, strut wake, and vortex flow strength are presented in
this thesis. Aerodynamic measurements that were made included mean
velocity and turbulence intensity profiles, and the axial length scales.
Inlet turbulence data indicate that the major effect of the flow con-
traction appears to be the elongation of atmospheric turbulent eddies
from 20 cm to 200 cm. Eddies of this size dominate the generation of
blade passing frequency (BPF) noise. Reducing the eddy size by the use
of a grid revealed the vortex flow strength to be the second major source
of noise at BPF. A doubling of vortex flow strength produced a 6 dB in-
crease in the sound pressure level (SPL) of the first BPF. The variation
of the SPL with the decay of the strut wake was small. The SPL showed
less than a 2 dB change with a doubling of the wake turbulence intensity
or the velocity defect. The measured sound spectra were compared with
predicted trends from two different analyses. The results of this com-
parison further supported the conclusion that the strut wake structure
was not as effective in producing noise at the vortex strength or the
inlet turbulent eddies. A discussion of the relative importance of
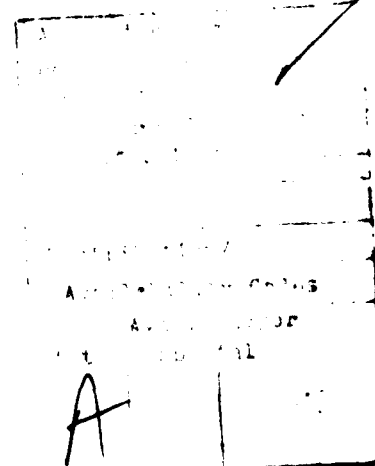various sources of noise due to the flow field is given.

TABLE OF CONTENTS

LIST OF FIGURES

LIST OF TABLES

NOMENCLATURE

a_o speed of sound

B slope in King's Law Equation for hot wire sensors

$$(E_1 + e_1)^2 = E_o^2 + B(\bar{V})^\eta$$

B_o number of rotor blades

b one-half blade chord

BPF   blade passing frequency

C a constant

C_D rotor design drag coefficient

C_L rotor design lift coefficient

c blade chord

$E + e$ instantaneous anemometer voltage

E DC part of anemometer voltage

e AC part of anemometer voltage

$F_1(r_t/L_x, kr_t)$ radiation function

f frequency (Hz)

G nondimensional sound power parameter

SPF   strut passing frequency

$g(\Gamma)$ frequency parameter

I intensity

IGV   inlet strut

k wavenumber (χS)

k_x, k_y axial and tangential component of the nondimensional wavenumber

L_x, L_θ axial and tangential integral length scales

L_w wake width based on semi-depth nondimensionalized by rotor blade spacing

ℓ	characteristic length $(2bC_D)$
ℓ_1	axial velocity upstream of contractions divided by axial velocity downstream of contraction
ℓ_2	width of stream before contraction divided by width after contraction
M_a	axial Mach number, U_x/a_o
M_{rel}	relative Mach number, U/a_o
M_t	tip Mach number, U_T/a_o
N	number of rotor blades
$\bar{n}$	vector normal to axial and radial vectors
NBL	natural boundary layer
P_1, P_2	sound pressures
P_o	reference sound pressure, 2×10^{-5} N/m^2
q, $\sqrt{\overline{q^2}}$	fluctuating turbulent velocity, $\overline{q^2} = (\overline{u^2} + \overline{w^2})$
q_o	turbulent velocity component normal to the chord
r, r_t, r_h	local, tip and hub radius of the rotor blade
S	rotor blade spacing, $2\pi r/N$
S_r	rotor blade area, $s \cdot c \cdot B_o$
s	blade span
$\bar{s}$	axial velocity vector
SPL	sound pressure level
T	integral time scale
t	time
U	velocity
U_c	mean axial velocity at $r/r_t = 0.75$

U_L	local mean axial velocity between struts
U_m	local mean axial velocity
U_r	local mean radial velocity
U_{rel}	relative velocity
U_{rx}	resultant mean velocity, $U_{rx} = \sqrt{U_x^2 + U_r^2}$
U_T	blade tip speed
U_x	local mean axial velocity with no strut present
U_θ	local mean tangential velocity
u, v, w	fluctuating turbulent velocity in the axial, tangential and radial directions
$\overline{u^2}$	mean square of axial turbulent velocity fluctuations
$\sqrt{\overline{u^2}}/U_x$	axial turbulence intensity
V	component of velocity normal to hot wire sensor
$\sqrt{\overline{v^2}}/U_x$	tangential turbulence intensity
x	axial distance
W	total acoustic power
Y	tangential probe distance nondimensionalized with respect to local rotor blade spacing $[(r\beta)/S]$
Z	distance between hot wire and strut trailing edge for aerodynamic measurements and distance between rotor blade leading edge and strut trailing edge for acoustic measurements, nondimensionalized with respect to strut chord
α	strut incidence angle
β	tangential probe location (radians)
β_2	exit relative flow angle

β_1', β_2'	inlet, exit rotor blade angles
Γ	nondimensional frequency $(2\pi f L_x/U_x)$
γ	angle between hot wire and axial direction
ε	contraction parameter, $\varepsilon = (\ell_2^2/\ell_1^2)$
ζ	stagger angle
η	exponent in King's Law Equation $(E_1 + e_1)^2 = E_o^2 + B(v)^\eta$
θ	tangential direction
κ	angle of probe separation in the circumferential direction
λ	probe arc location upstream of inlet
λ_o	sound wave number
ξ	strength of vortex
π	3.14 ...
ρ	fluid density
$\rho_{uu}(\tau)$	autocorrelation coefficient
σ	rotor blade solidity, c/s
τ	delay time
ϕ	flow coefficient, U_c/U_T
χ	acoustic wave number
ψ	average lift slope, $(C_L/q_o U)$
ψ_o	stage loading coefficient
ψ_c	static pressure coefficient
Ω	shaft speed

ACKNOWLEDGMENTS

CHAPTER I

INTRODUCTION

1.1 Statement of the Problem

The use of a fan or rotor to impart energy to a fluid (air or water) invariably results in the generation of noise. This noise is a major problem in aircraft turbomachinery (propellers, compressors, and fans). Aircraft power plants expose a large portion of the general population in the areas around airports to high levels of noise. The sound spectrum of fan or compressor noise is characterized by a broadband signal on which is superimposed discrete peaks at blade passing frequency and its multiples. This characteristic sound spectrum is also found in other applications. It is therefore important to understand the sources of rotor noise.

Several sources of rotor noise have been identified. They are generally classified into two groups. The first group are those time random disturbances which contribute to the broadband signal. Included in this group are boundary layer turbulence (walls, blades, etc.), separated flows, shed vorticity from blade trailing edges, and general inlet turbulence. The second group of disturbances are those which appear to be periodic from the rotor frame of reference. This type of disturbance contributes mainly to tone noise. Included in this class are free stream elongated turbulent eddies, upstream blade wake, velocity defects, and upstream vortex flow generated by struts.

This thesis is concerned mainly with this second group of sources and their relative importance in noise generation. Important parameters that will be experimentally measured and correlated with the sound

spectra are inlet turbulence and its length scale, mean velocity and turbulence profiles downstream of a strut row, and the vortex flow generated at the root of a strut. The data gathered here, in conjunction with an analytical approach, will be used to identify the dominant flow related sources of noise.

1.2 Engineering Inportance

A variety of mechanisms are responsible for the generation of noise by a low speed fan or turbomachinery rotor. Atmospheric turbulence, wall boundary layer turbulence, and strut-generated disturbances (wake turbulence and velocity defect, vortex flow regions at the strut tip and root) are some of the sources that contribute to the rotor noise. Of these noise sources, the effect of turbulence has been intensively investigated. Results of these investigations have shown that turbulence is a major source of broadband noise in low speed rotors. This conclusion led to the development of successful noise reducing techniques. These include removal of turbulence generating structures (grilles, support rods, struts, etc.) from upstream of the rotor. Active removal of the wall boundary layer by suction has also reduced the level of broadband noise. These techniques, however, are not without drawbacks. Penalties incurred by use of these methods include increased engine complexity and weight, as well as degraded aerodynamic performance.

These methods for reducing noise were the direct result of implementation of data gathered in the study of the noise-generating mechanisms. It must therefore follow that further reductions in the levels of turbomachinery noise can be associated with the study of the remaining sources. These include inlet eddy size and turbulence levels, strut

wake parameters of velocity defect and turbulence structure, and the generation of vortex flow in the centerbody and blade tip regions.

1.3 Scope and Method of Investigation

The investigation reported here can be broadly classified into three phases. During the first phase, the effort was directed toward an understanding of the atmospheric turbulent eddy elongation process as it travels from upstream of the inlet to a position upstream of the rotor. The second phase of the investigation consisted of the study of the strut generated noise. This study was carried out using four upstream struts, operated at various strut-to-rotor spacings. Flow field parameters, as well as the radiated noise levels, were measured. The mean velocity and turbulence data from the wake and end wall regions were correlated with the far field acoustic levels in order to identify the effects of various strut disturbances on noise generation. Trends of acoustic spectra were also compared to the predicted levels obtained by an analytical noise prediction technique and an unsteady thrust analysis. Results of these comparisons were used to support the trends derived from the experimental data.

The final phase of this investigation concentrated on the rotor noise generated by the formation of vortex flow at the root section of the strut. In this phase, the strength of the vortex flow was altered by varying the incidence angle of the strut. The span of the strut was truncated to reduce the effect of the wake on the sound spectra. Mean velocity and turbulence data in the region of the inner wall were correlated with the measured far field BPF acoustic levels in order to identify the mechanisms that are responsible for the rotor noise in low speed turbomachinery.

CHAPTER II

NOISE SOURCES, GENERATING MECHANISMS,
AND PREVIOUS INVESTIGATIONS

2.1 Sources of Rotor Noise

The generation of noise by a fan or rotor can be related to the non-uniform flow field in which it operates. The fluctuating velocities of the nonuniform flow field produce time dependent pressure on the rotor blade. Tam[1] distinguished between two components of surface pressure fluctuations due to blade surface turbulent boundary layers. Subsonic and supersonic regimes exist which dictate radiation or decay of the broadband components. The present investigation considers only the radiated sound at blade passing frequency and its multiples. Therefore, this phenomenon is unimportant for this investigation.

The variations in an unsteady flow field are classified into two categories: (1) a spatially varying disturbance caused by upstream wakes, vortices, boundary layer, etc.; and (2) temporal disturbances such as atmospheric turbulence. Atmospheric turbulence is a three-dimensional flow characterized by velocity fluctuation intensities, as well as an eddy size. These turbulent eddies are by nature distributed randomly in space. Therefore, as an aircraft moves through the atmosphere, the compressor will encounter various eddies at different times.

The spatial variations in the inlet velocity field are typically generated downstream of blade rows, support struts, grilles, casing walls, or any other proturberance into the flow. Wall boundary layer gradients, blade or strut wakes, and blade generated vortices are examples of spatially nonuniform flow disturbances. Unlike spatial variations in the velocity field, the temporal component of the nonuniform

flow field varies with respect to time. The disturbances in the velocity field which fluctuate with time can be attributed to rotating upstream blade rows, random turbulence present in the inflow stream, and the motion of the vehicle in which the rotor is housed.

2.2 Previous Investigation on Noise Generating Mechanisms

The discussion which follows is a condensed version of the literature reviews written by B. Lakshminarayana[2], B. E. Robbins[3] and N. A. Moiseev et al.[4]. Various sections are expanded to update this material.

The mechanisms by which such disturbances as incident turbulence, upstream blade wakes, and vortices generate noise are twofold.

2.2.1 Quadrupole sources.
The interaction of turbulence with the potential flow field of the rotor is known to produce a random quadrupole source about the rotor blade. Ffowcs-Williams and Hawkings[5] were the first to investigate this noise source. In their investigation, they noted that inhomogeneities of the homogeneous wave equation caused by a finite velocity field in the vicinity of the fan induced a quadrupole source distribution. This type of source was later investigated in detail by Chandrashekara[6]. Chandrashekara developed a theoretical estimate of the sound power due to the quadrupole sources, then compared the results with experimental measurements of turbulent velocity fluctuations and the rotor potential flow field. The conclusion reached by Chandrashekara and by Ffowcs-Williams and Hawkings was that quadrupole sources are insignificant noise generators for low speed fans at low blade loadings.

2.2.2 <u>Dipole sources</u>. A dipole source is generated on the blade when the rotor encounters nonuniformities in the flow field. The oscillating velocities of the nonuniform flow produces fluctuations in the angle of attack of the blade row. The changes in the angle of attack lead to unsteady blade forces which radiate noise. This type of source has been studied by many investigators. The following is a brief synopsis of their work.

Sofrin and McCann[7] first showed qualitative evidence that the radiated sound intensity was dependent on the level of inlet turbulence. In their investigation, they examined the noise due to the viscous interaction of the inlet guidevane (IGV) and the rotor as a function of the axial spacing between these two blade rows. Their data showed the noise level decreasing as the axial spacing increased. This trend continued until a certain distance was reached, where the noise level remained unchanged with increased rotor-IGV separation. Beyond this separation distance, the noise level could only be lowered by the complete removal of the IGV. From these data, Sofrin and McCann concluded that the presence of the IGV upstream of the rotor raised the turbulence level in the duct, and the drop in the noise level on removal of the IGV was due to the lowering of the turbulence level incident on the rotor.

The production of noise by turbulence was further investigated by Sharland[8]. Sharland experimentally studied the noise produced by a flat plate in an open jet. Sharland found that with the plate in the potential core, the noise level was due to lift fluctuations resulting from vortex shedding at the trailing edge. This, however, was not the case when the plate was in the turbulent mixing region of the jet. In

this region, the length scale of the turbulence was on the order of the plate chord, and the turbulent velocity fluctuations were the dominant noise source. Sharland further observed that the noise due to boundary layer pressure fluctuations was insignificant when compared to vortex shedding and turbulence noise. Sharland provided an estimate of the level of noise produced due to incident turbulence induced airfoil lift fluctuations. He derived this equation by combining the acoustic theory due to Curle[9] with Liepmann's[10] statistical unsteady airfoil lift ideas.

$$W = \frac{\rho}{48\pi a_o^3} \int \psi^2 c \ U_{rel}^4 \ \overline{(q_o)^2} \ dy \ , \tag{2.1}$$

where W = total acoustic power,

ρ = fluid density,

a_o = velocity of sound,

ψ = average lift slope defined by $C_L = \psi q_o/U$,

q_o = turbulent velocity component normal to the chord,

c = blade chord at spanwise location y

and U_{rel} = relative mean velocity of the blade section at y.

Morfey[11] narrowed the scope of the problem by choosing to study only the broadband noise due to the interaction of the turbulent wakes from upstream blade rows with a downstream blade row. Morfey measured and analyzed the noise levels from a number of multistage compressors and obtained several important correlations. He found that the frequency spectra collasped reasonably well using the nondimensional parameter ℓ/λ_o [the characteristic length ℓ is related to the upstream blade drag

coefficient (C_D) and blade chord (2b) by the equation $\ell = 2b\ C_D$, λ_o is

the sound wave length]. This was unexpected since, up to this point,

the frequency collapse would have been expected to depend on the Strou-

hal number, $f\ell/U$. The importance of this last statement should not be

overlooked. Instead of the sound power varying as M_{rel}^6 as predicted

using Strouhal number scaling, ℓ/λ_o frequency scaling results in sound

power varying as M_{rel}^5. Morfey analyzed the semi-empirical collaspe of

the sound power data and arrived at the following nondimensional sound

power parameter

$$G = \frac{dW}{df} \cdot \frac{f^3 s^2 \csc^4 \beta_2}{\rho a_o^5 S_r M_{rel}^5} \,, \qquad (2.2)$$

where B_o = number of rotor blades,

     f = frequency,

     G = nondimensional sound power parameter,

     M_{rel} = relative Mach number, U_{rel}/a_o,

     s = blade span,

     S = blade spacing, $2\pi r/B_o$,

     S_r = rotor blade area s.c.B_o,

and β_2 = exit relative flow angle.

Mugridge and Morfey[12] analyzed the experimental and theoretical results

obtained from various axial flow fan noise sources and reached some im-

portant conclusions regarding the physical mechanisms involved in the

generation of unsteady blade lift noise. They determined that the broad-

band noise radiated from subsonic fans was related to random fluctuations

in the blade loading. The fluctuations in the blade loading were found

to be the result of the blade encountering random turbulence. As was shown by Morfey's[11] experimental work, the inlet turbulence noise mechanisms dominate all other sources in most applications. This inlet turbulence may originate in the wall or blade boundary layers or be convected with the mean flow.

Mugridge and Morfey concluded the following from their investigations:

1. Fan noise at subsonic speeds may be due to dipole or quadrupole source. The predominant source of noise in lightly loaded or low speed fans is the dipole type, arising from fluctuating blade forces.

2. Noise from incident turbulence can be estimated from the blade surface spectrum and the turbulent velocities entering the blade row.

3. Vortex flows associated with blade tip clearances and duct boundary layers are a source of turbulence and, consequently, broadband noise. Because they have opposing effects on the vortex flow, tip clearance and boundary layer thickness can be balanced to reduce the noise radiation.

An exact analytical procedure for predicting the radiated noise from a fan due to turbulence was first provided by Sevik[13] and Mani[14]. Their procedure consisted of first assuming a turbulence model, then calculating the turbulence generated unsteady lift. After calculating the unsteady lift, the force distribution was determined to predict the acoustic radiation of the fan.

Sevik[13] began his analysis by assuming the turbulence to be homogeneous and isotropic. The unsteady lift on the rotor blade was then calculated by using Sears'[15] gust function. Based on these assumptions, Sevik obtained the following equation for the spectral density of the sound power:

$$\frac{dW}{d\Gamma} = \pi^3 \left[\frac{\overline{u^2}}{U_x^2}\right] M_a^3 \left[\frac{\rho U_x^3 r_t^2}{1+\phi^2}\right] \left(\frac{r_t}{L_x}\right)^2 \left[1 - \left(\frac{r_h}{r_t}\right)^2\right]^2 \cdot g(\Gamma) F_1 \left(\frac{r_t}{L_x}, kr_t\right), \quad (2.3)$$

where

$\Gamma = \dfrac{2\pi f L_x}{U_x}$, nondimensional frequency,

W = sound power in watts,

$\overline{u^2}$ = mean square of axial turbulent velocity fluctuations, $\sqrt{\overline{u^2}}$,

a_o = speed of sound,

ρ = fluid density,

U_x = axial flow velocity,

r_t = tip radius of the rotor,

L_x = turbulent axial integral length scale,

$g(\Gamma)$ = frequency parameter defined in Reference 12,

$F_1(r_t/L_x, kr_t)$ = radiation function given in Reference 12,

M_a = axial Mach number, U_x/a_o,

ϕ = flow coefficient,

r_h/r_t = hub-to-tip ratio,

and f = frequency (Hz).

Sevik's expression predicts that the radiated sound spectrum depends on the turbulence intensity, a characteristic time scale defined as the

ratio of the integral length scale of turbulence to the axial flow velocity, and the characteristic length scales of blade chord, radius of the rotor, and the ratio of the integral scale of turbulence to acoustic wavelength. It is important to note that the spectrum predicted by this theory does not exhibit the characteristic peaks at blade passing frequency and its harmonics. This is due to Sevik's theory not including any blade-to-blade correlations of unsteady lift.

Mani's[14] approach to the problem of rotor generated sound due to incident free stream turbulence was similar to that taken by Sevik[13]. Mani's model, like Sevik's model, assumed the turbulence to be homogeneous and isotropic. Mani extended his model by assuming the turbulence to be weak and that it could be characterized by a longitudinal velocity correlation function of the type $\exp(-r/L_x)$. In this expression, r is the separation between points in the turbulence field, and L_x is the length scale of turbulence. Using these assumptions, Mani derived the following expression for the radiated sound:

$$\chi \frac{dI}{d\chi} = \frac{3}{2} \rho U_x \overline{u^2} \cdot \frac{\pi^2 \sigma^2 \chi S}{24 L_x \cos^2 \zeta} \cdot \left[\frac{(1-M_a^2)^{1/2}}{2\pi c \chi \sin \zeta} \cdot \log \left\{ \frac{1+2\pi\omega_{r+}}{1+2\pi\omega_{r-}} \right\} \right] \cdot$$

$$\left\{ \int \frac{(1+3\cos^2\zeta)k_x^2 + L_x^{-2} + 6k_x k_y \cos\zeta\sin\zeta + (1+3\sin^2\zeta)k_y^2}{(L_x^{-2} + k_x^2 + k_y^2)^{1/2}} \, dk_y \right\} \cdot$$

$$\sin^2\zeta \left\{ \frac{\pi}{2} + \frac{(1-M_a^2)(\cot^2\zeta-1)}{2} \cdot \left(-\frac{\pi}{2M_a^2} + \frac{\pi}{2M_a^2(1-M_a^2)^{1/2}} - \right. \right.$$

$$\left. \left. \frac{\arcsin M_a}{M_a^2(1-M_a^2)^{1/2}} + \frac{1}{M_a} \right) \right\} , \qquad (2.4)$$

where I = intensity,

$\overline{u^2}$ = mean square of axial turbulent velocity fluctuations,

χ = acoustic wave number,

ζ = stagger angle of cascade,

L_x = longitudinal integral length scale of turbulence,

M_a = axial Mach number,

σ = blade row solidity, c/S,

c = blade chord,

$$\omega_{r\pm} = (c\chi/2M_{rel}\sqrt{1-M_a^2}) \cdot \{\sqrt{1-M_a^2} \pm M_t\},$$

M_{rel} = flow Mach number relative to the rotor,

M_t = rotor tip Mach number,

k = χS, wave number,

S = blade spacing,

and k_x, k_y = axial, tangential component of the nondimensional wave number.

The above expression indicates that the acoustic energy per unit frequency is dependent on intensity of the incident turbulence, axial flow Mach number M_a, rotor blade tip Mach number M_t, blade row solidity σ, and most importantly, the ratio of turbulence length scale to blade spacing L_x/S. The spectrum predicted by Mani's expression exhibits broadband peaks at the blade passing harmonics when the value of L_x/S exceeds 0.5. The peaks become sharper as the value of L_x/S becomes larger. This is important since Sevik's[13] theory did not predict these peaks. For values of L_x/S less than 0.5, although Mani's expression indicates the peaks disappear, it does predict a general increase in the nondimensional sound level.

Sevik's[13] and Mani's[14] theories were later modified by Robbins and Lakshminarayana[16] to include the aerodynamic transfer function of a cascade developed by Whitehead[17]. Robbins and Lakshinarayana conducted an experimental investigation in which the measured sound spectrum generated by a rotor operating at several tip speeds and in different intensity levels of inlet turbulence were compared to the predicted spectra. The major conclusions they reached are listed below.

1. The total sound power is dependent not only on turbulent intensity but the length scale as well. The sound power is proportional to $\overline{u^2} \, U_{rel}^4 / L_x^2$.

2. The sound spectrum had a shape similar to the turbulent energy spectrum.

3. The sound spectrum levels produced can be accurately predicted over a limited frequency range. The Sevik-Sears theories overestimation of noise intensity at lower frequencies can be attributed to interference effects due to a cascade.

4. The use of the cascade gust function did not affect the sound pressure level at moderate frequencies (0.7 to 2.0 kHz). At higher frequencies, the predictions with the cascade gust function were closer to measured sound levels, particularly with Mani's theory.

A more recent extension of Sevik's[13] analysis has been done by Thompson[18]. Thompson has extended Sevik's analysis to include blade-to-blade correlations so that the time dependent thrust of a propeller could be predicted.

Pickett[19] has extended Mani's theory to include anisotropic turbulence. The aerodynamic response function Pickett used was the function developed by Mugridge[20] for a three-dimensional flow. Pickett reached the following conclusions.

1. The frequency distribution of radiated sound is primarily dependent on the axial length scale, L_x. Large L_x leads to discrete tones at blade passing frequency and its harmonics.

2. Sound power levels depend on turbulent intensity and circumferential and radial length scales.

3. The division of sound radiation upstream and downstream is strongly dependent on the circumferential and radial length scales.

Lowson[21] eliminates the need to model the turbulence and finds an appropriate aerodynamic forcing function by assuming that the time dependent lift on a blade is known. Beginning with the single blade case, Lowson expanded his analysis with a weighting function to the multibladed case. This weighting function consists of two parts, a delta function at the blade passing frequency, BPF, and a background level part due to random blade-to-blade variations. When these two parts are correlated, a peak appears at BPF. Lowson concluded that, based on these variations, a greater effort to achieve uniformity in the flow field would be justified.

Like Lowson, Hanson[22] also assumed that the time dependent lift is known. Hanson's model permits exact solutions for the power spectral densities of the blade and the sound field by the use of the pulse modulation theory. The turbulence is assumed to consist of eddies which are

discrete but whose characteristics (intensity, width, and length) are random variables. Hanson further assumes that the force due to each eddy acts at a point along the radius of each blade. Radial distribution of the force was neglected so long as the radial dimension of the eddy is smaller than the wavelength of the sound. In his experimental data, he found that inlet turbulent eddies are elongated as they are sucked into a static fan and are chopped by each blade at least once per revolution. This chopping of the eddy gives rise to a train of lift pulses on the blade at rotational frequency. The irregularities of the eddies were modeled by varying the pulse amplitude and pulse position. These pulse functions, as well as the distribution function of the turbulent eddies, were determined from direct measurements of the instantaneous lift on the blade. Although Hanson's theory is in good agreement with his experimental data, the difficulty in measuring the blade loading in many installations is a major drawback.

The importance of the turbulence on the generation of noise was also shown by Moiseev, Lakshminarayana, and Thompson[23] in their experimental investigation of boundary layer turbulence noise. They verified that the intensity and length scale of turbulence were controlling factors in noise generation. Their work also verified Mani's[14] prediction that, with decreasing L_x/S (for nearly isotropic turbulence), the general noise level will increase and the BPF peaks will broaden. Finally, Moiseev et al. concluded that the long eddies were primarily responsible for discrete tone prediction.

Homicz and George[24] studied the effect on noise of compressibility and distributed loading from the interaction of isotropic, homogeneous turbulence on a rotor. During the course of their investigation, they

proposed the parameter $U_x/L_x \Omega$, where U_x is the axial velocity, L_x is the turbulent length scale, and Ω is the rotor shaft speed. This parameter is important because large values lead to a broadband noise, while progressively smaller values were found to give rise to an increasingly discrete noise spectrum. Homicz and George found that the main influence of the compressibility and distributed loading effects was the lowering of high frequency noise.

Lowson, Whatmore and Whitefield[25] investigated the rotor tip noise. They found that the flow irregularities generated at the blade tip interacted with the rotor to produce high frequency noise. Lowson et al. concludes that, although several source mechanisms were involved in the generation of noise, they were easily controlled. When these data are compared to Homicz and George's[24] theory, good agreement was achieved.

Dittmar[26] also investigated rotor tip flow irregularities as a noise source. He found that the magnitude of the rotor tip noise was on the same order as the rotor wake-stator noise mechanism. Dittmar concluded that a 6 dB noise reduction could be expected to occur if the rotor tip defect stator noise mechanism was removed.

Cumpsty and Lowrie[27] made noise measurements for various rotor tip speeds inflight and compared the results to noise measurement made during static conditions. The major conclusions they reached are listed below:

1. Under typical static test conditions, there are enough
   unsteady distortions in the inflow to dominate the blade
   passing frequency, BPF, sound at subsonic rotor tip
   speeds. These unsteady distortions cause the variation
   of sound pressure level with time usually associated with
   rotor BPF tones.

2. Boundary layer intake is the dominant source of distortion at low Mach numbers. The momentum thickness of the boundary layer appears to be the best correlating parameter. At higher Mach numbers, low order turbulent eddies become the dominant source.

3. There is a significant change in noise between static and in-flight tests. Greater care must therefore be taken in interpreting static noise tests.

Goldstein et al.[28] included in their theoretical model the compressibility effect, convection of eddies by the mean flow, and anistropic inlet turbulence. From their investigation, they concluded that when turbulence correlation lengths become equal to blade spacing, the predicted spectra exhibits peaks at tonal frequencies. They also found that the quadrupole noise source contributes mainly to the broadband spectrum until the correlation lengths of the turbulence become quite large.

A critical review of turbomachinery noise is presented by Cumpsty[29]. Cumpsty covers the present base of experimental data and notes the lack of application of present theories. Theoretical models are described with emphasis on the assumptions they make. The overall conclusion drawn by Cumpsty is that very little is known about the noise mechanisms of high speed machinery.

CHAPTER III

EXPERIMENTAL APPROACH AND TECHNIQUE

3.1 Test Facility

An existing aero-acoustic test facility at the Applied Research Laboratory was used for this investigation. Originally designed by Robbins and Lakshminarayana[16], the facility was modified by Moiseev et al.[23] to include a larger anechoic chamber, and an extended inlet annulus. For this investigation, the test facility was basically in the same configuration as employed by Moiseev. However, two modifications were made: the addition of a new probe survey ring for circumferential traverses upstream of the rotor, and a fiberglass baffle upstream of the anechoic chamber air inlet. A detailed description of these changes will be given later.

The facility is shown in Figure 1. It consists of four major sections: the anechoic chamber, the test rotor, the screen diffuser and baffle chamber, and the Joy Axivane axial flow fan. The anechoic chamber surrounds the rotor inlet and offers a known acoustic environment in which to measure the acoustic performance of the test rotor. Downstream of the rotor, a screen diffuser and a baffle chamber are utilized to prevent flow separation with its attendant noise and to inhibit the propagation of Joy fan radiated noise. The Joy fan was used to control the mass flow through the test rotors. Only a brief description of the facility will follow. For the detailed design philosophy, the reader is referred to Reference [3].
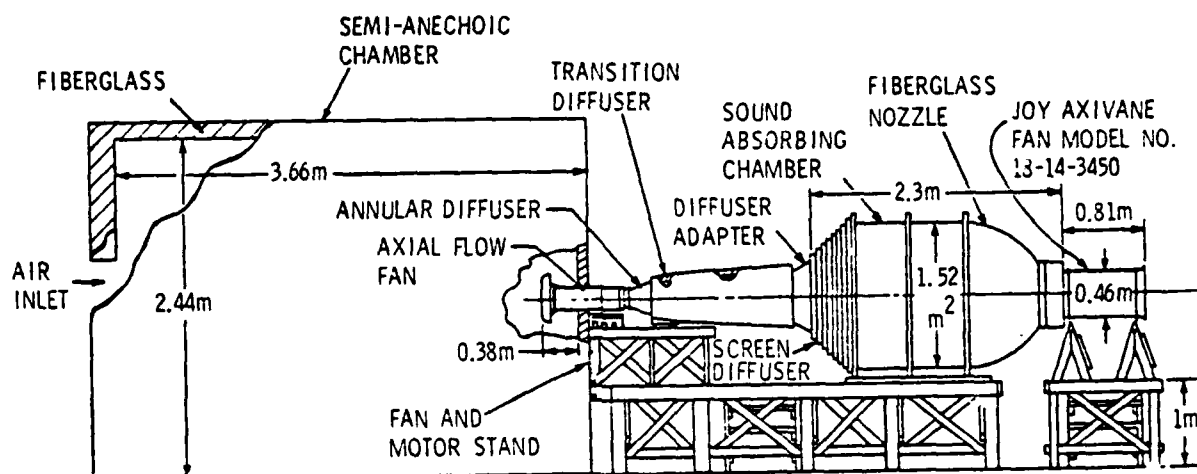
Figure 1. Aero-Acoustic Test Facility.

3.1.1 <u>Anechoic chamber</u>. The anechoic chamber consists of a basic wooden frame supported from the floor by 12 spring-vibration isolators. The ceiling and floor of the chamber were formed by an 18.25 cm layer of Owens-Corning Type 705 industrial fiberglass. The walls were constructed in a bookcase fashion, where the spaces between shelves were filled with a 15.5 cm thick layer of fiberglass. To further attenuate extraneous outside noise, a 5.08 cm airspace was formed by covering the exterior wood frame with tar paper. Finally, the entire chamber was isolated from ambient room noise by a composite 1.91 cm lead foil covered plywood partition. The interior dimensions of the chamber are 3.35 m x 3.66 m x 2.44 m.

From this baseline configuration, special modifications were made to permit the use of the test rotor facility with the anechoic chamber. To minimize the ingestion of turbulence from the walls of the chamber, the inlet annulus of the rotor was centered in the wall and extended 38 cm out from the wall. Special attention was given to the region where the annulus entered the chamber, so as to prevent exterior air from being ingested. In the wall opposite the inlet, a two-meter diameter air inlet hole was cut concentric with the inlet annulus as shown in Figure 1. Finally, a thin porous foam rubber sheet covered the hole to filter and diffuse the air.

To verify that free field acoustic conditions existed inside the anechoic chamber, a series of tests were conducted. The procedure consisted of driving a speaker at selected pure tones and measuring the sound field with a condensor microphone at various distances from the source. Ideally, a good free field condition is indicated by a 6 dB drop

in sound pressure level (SPL) with a doubling of separation distance.

The results of these tests are plotted in Figure 2. The first experiment was a repeat of Moiseev's et al.[23] test where the anechoic chamber air inlet was closed and the inlet duct was removed. The results shown in Figure 2a indicated that good free field conditions existed. In the second configuration, the inlet annulus was replaced and the chamber air inlet hole was opened. The fiberglas baffle was not in place on the plywood partition for this set of measurements. The speaker was centered at the inlet annulus lip and the microphone traversed along the annulus centerline. When the data is plotted against ideal free field results, a ±3.0 dB scatter was observed (Figure 2b). It was felt that this scatter was the result of sound reflections off the plywood partition which was located directly in front of the chamber air inlet hole. To rectify this situation, a 5.08 cm thick fiberglas baffle was fastened to the plywood partition (as shown in Figure 1) and the test repeated. As indicated in Figure 2c, a 6 dB drop in SPL was measured with a doubling of separation distance, thus verifying a good free field acoustic environment.

3.1.2 Fan and inlet annulus. The design and operating characteristics of the rotor are summarized in Table 1. The tip diameter of the rotor is 17.53 cm. The centerbody diameter is 8.74 cm. This results in a centerbody-to-tip ratio of 0.482. The variation of blade chord and stagger angle as a function of radius are presented in Table 2. Lastly, the blade profiles and flow angles are shown in Figure 3.

The standard configuration of the rotor employed 17 blades. This resulted in a blade spacing of 2.43 cm at mid-radius. The rotor was

TABLE 1

ROTOR DESIGN AND OPERATING CHARACTERISTICS

Number of rotor blades 17

Rotor diameter . . . . 17.53 cm

Rotor operating speed . . . . 5440 rpm

Inlet air velocity . . . . 39.0 m/sec

Flow coefficient (ϕ), ... 0.75

Blade pressure coefficient (ψ_s), (design at
    mid-span) 0.25

Blade drag coefficient (C_D), (design at mid-span) . 0.04

Blade lift coefficient (C_L), (design at mid-span) . 0.43.

Stage loading coefficient (ψ_o), (design at
    mid-span) 0.38

Blade chord (at $r/r_t = 0.75$) . . . . 4.06 cm

Blade spacing (at $r/r_t = 0.75$) . . . . 2.43 cm

Stagger angle (at $r/r_t = 0.75$) . . . . 34.95 degrees

Solidity (at $r/r_t = 0.75$) 1.67
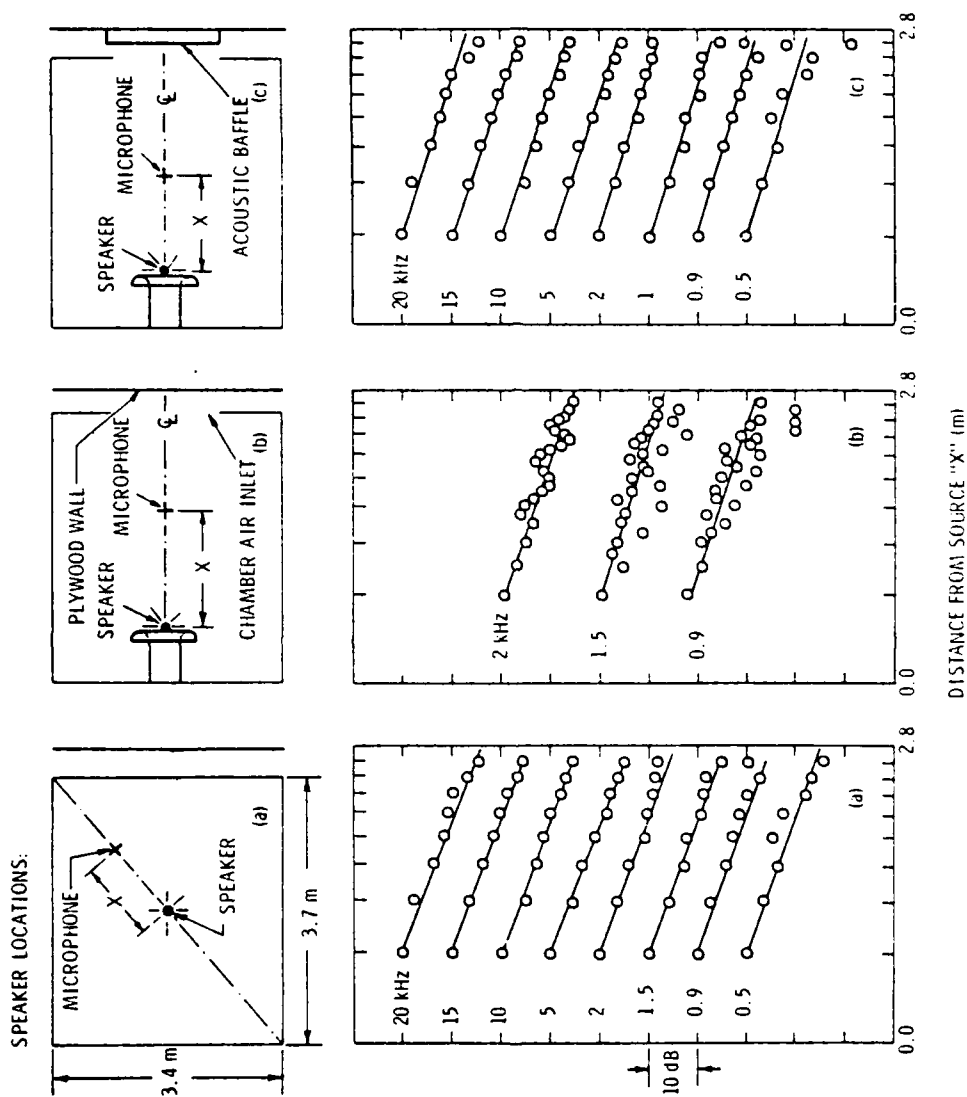
Figure 2. Inverse Square Law for Semi-Anechoic Chamber.

24
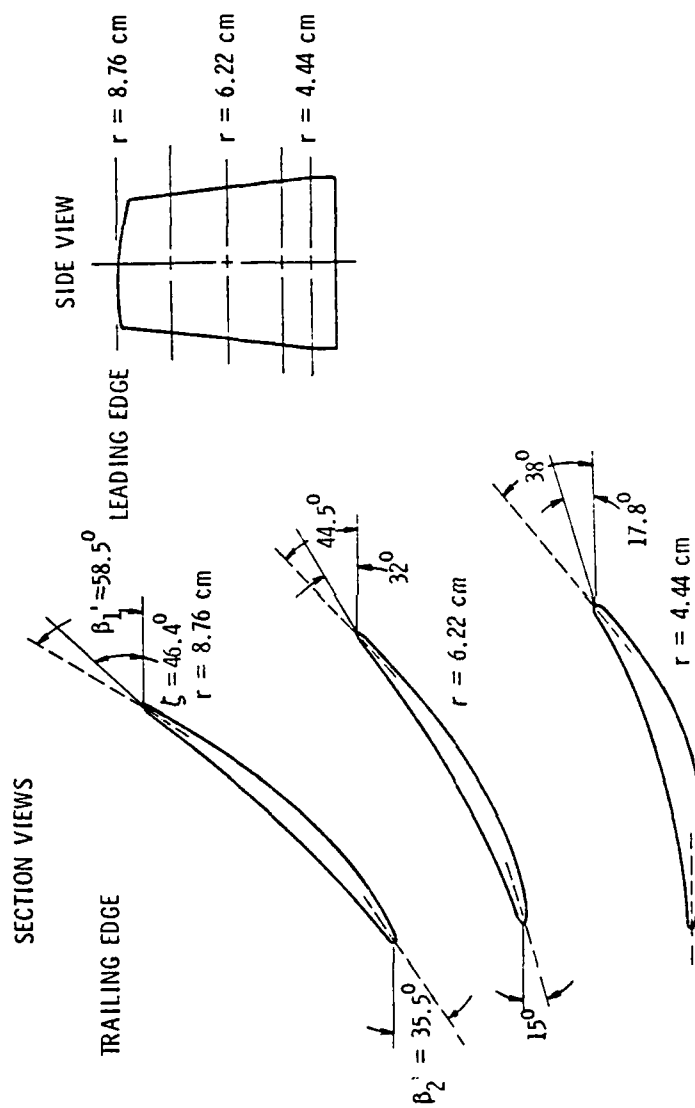
Figure 3. Rotor Blade Profiles at Three Radii.

TABLE 2

ROTOR CHORD AND STAGGER ANGLE VARIATION WITH RADIUS

Radius (cm)	Chord (cm)	Stagger Angle (radians)
4.57	3.99	0.31
5.08	3.94	0.38
5.59	3.99	0.46
6.10	4.04	0.54
6.60	4.06	0.61
7.11	4.09	0.66
7.62	4.09	0.72
8.13	4.11	0.77
8.64	4.14	0.81

operator at a flow coefficient of $\phi = 0.75$. This corresponds to a design advance ratio of 2.35. The axial velocity at blade mid-span was held constant at 39.0 m/sec. The rotor operated at 5440 rpm. The steady state aerodynamic response of the rotor at mid-span is presented in Table 1. For a detailed summary of the rotor's steady state aerodynamic response, see Moiseev et al.[4].

The section of the facility forward of the test rotor is the inlet annulus. It consists of a bellmouth inlet, a 60.64 cm long inlet annulus, and a variable length centerbody. The centerbody was supported by two sets of three thin, aerodynamically shaped tie rods tangentially spaced 120 degrees apart. By altering the configuration of the center-body, the desired turbulent inflows to the rotor were obtained. A description of these configurations and the inflows produced are presented in Section 3.2.1 on inlet configurations. The last modification made was the addition of a new survey ring. As illustrated in Figure 1, the survey ring allowed the probe to make circumferential traverses at various radii at various axial locations upstream of the rotor.

3.1.3 _Screen diffuser and baffle chamber_. The exit flow from the rotor passes through an annular transition diffuser to the screen diffuser. The screens allow a rapid expansion of the flow without the risk of flow separation. From the screen diffuser, the flow enters the acoustic baffle chamber. The chamber was constructed of six parallel airfoil shaped baffles inside a 1.52 m square enclosure. The airfoil baffles and the enclosure walls were covered with a 5 cm thick layer of fiberglas sound sound absorption. Robbins[3] has provided a complete description of the design and construction of the screen diffuser and

baffle chamber.

3.2 Experimental Program and Instrumentation

3.2.1 Inlet configurations. For each phase of this investigation, the rotor inflow was generated by modifying the inlet configuration in conjunction with varying the rotor-to-strut spacing. The first phase, in which the effects of contraction on inlet turbulence were investigated, employed the configurations shown in Figure 4. In this cross-sectional view, the axial locations of flow measuring stations are indicated. The spinner over which station 1 is located is rotating with the rotor. The removable square mesh grid was used to alter the level and structure of the inlet turbulence. The grid has a mesh size of 2.86 cm and a rod diameter of 0.556 cm. This grid was used throughout the investigation.

The second phase of the investigation considered the noise spectra due to the rotor operating in strut-generated flow disturbances. The struts used had a NACA 0021 symmetric airfoil profile with a chord length of 13.97 cm and a span of 4.38 cm. Measurements were made with four struts on two different stationary centerbodies, one extending forward of the rotor 26.35 cm and the other 47.63 cm. Data were also taken with no struts present. When the struts were used, they were symmetrically spaced 90 degrees apart at zero incidence. The upstream location of the struts for each centerbody are illustrated in Figures 5 and 6. Measurements were taken with and without a grid.

In the final phase of the investigation, the radiated noise due to a rotor operating in a flow field with a dominant vortex flow near the centerbody was studied. The struts used were the same as those in the
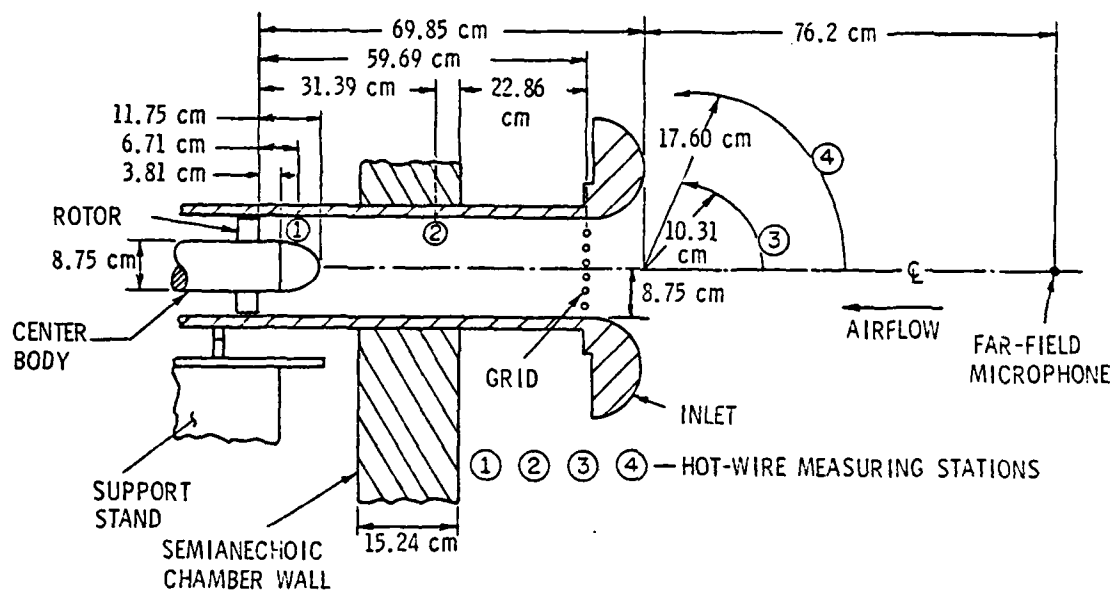
Figure 4.   Inlet Turbulence Annulus Configuration.
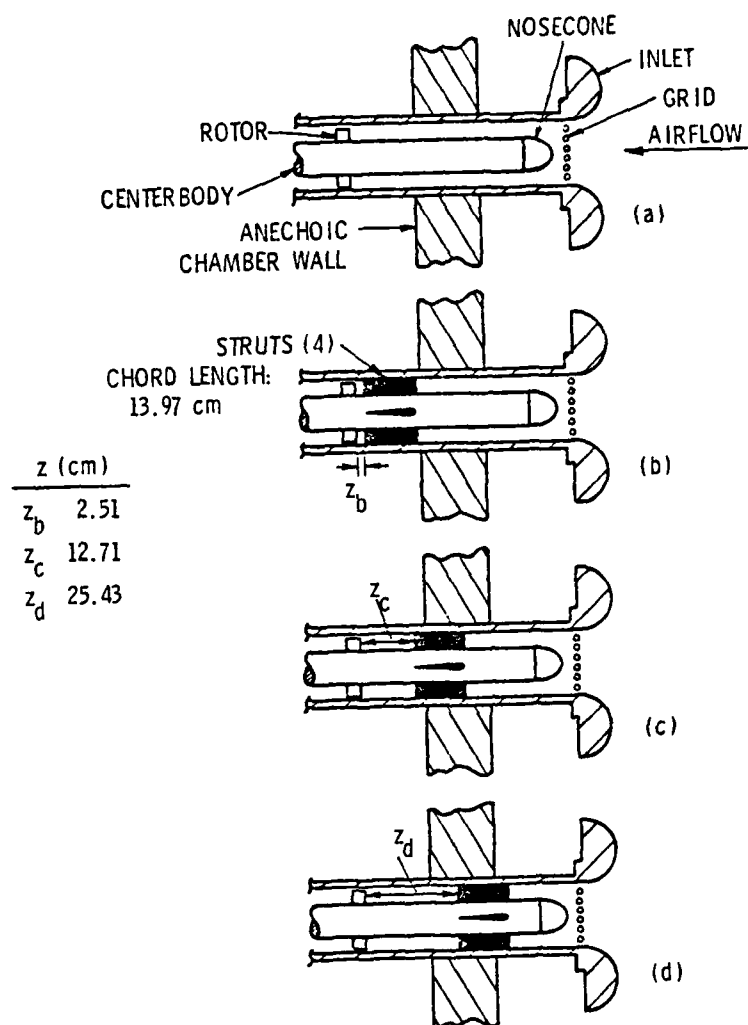
Figure 5. Inlet Annulus Configuration with 47.63 cm Long Centerbody.
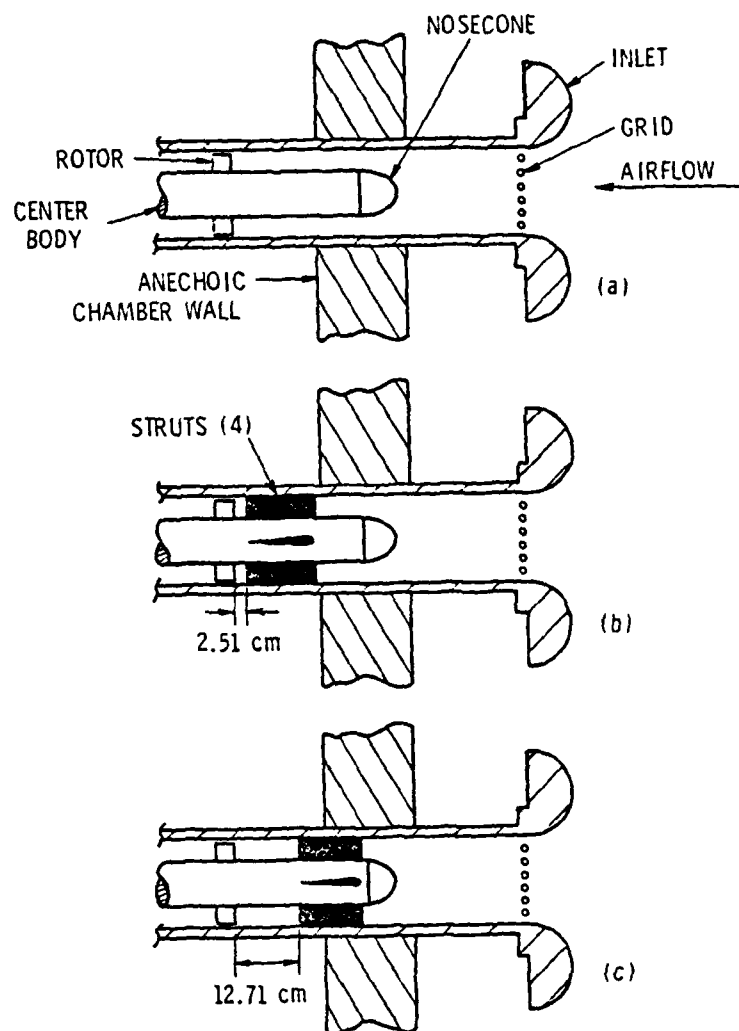
Figure 6. Inlet Annulus Configuration with 26.35 cm Long Centerbody.

above configuration except that the span was shortened to 1.19 cm to study the effect on the noise spectrum of vortex flow in the absence of the strut wake. Two shortened strut configurations were considered, one employing four struts space tangentially 90 degrees apart and the other employing a single strut. In both configurations, the grid was used to alter the inlet turbulence. The strength of the vortex flow was altered by changing the incidence angle of the strut from +12 degrees to -12 degrees. The mounting of the struts is shown in Figure 7.

3.2.2 Aerodynamic flow measurements

3.2.2.1 Inlet turbulence. Measurements of the inlet turbulence were conducted with an X-array hot wire probe. The mean velocities, turbulence intensities, and the axial length scale of turbulence were measured at several radii for four axial stations, see Figure 4. The axial and tangential components of turbulence intensity were determined by using the linearized King's Law equation. As stated by Von Frank[30], the axial and tangential turbulent velocities are calculated by Equations (3.1) and 3.2), respectively:

$$\sqrt{\overline{u^2}} = \frac{2\overline{E}\sqrt{U_x}}{B\sqrt{\sin \gamma}} \ \sqrt{\overline{(e_1 + e_2)^2}} \tag{3.1}$$

and

$$\sqrt{\overline{v^2}} = \frac{2\overline{E}\sqrt{U_x}}{B\sqrt{\sin \gamma}} \ \sqrt{\overline{(e_1 - e_2)^2}} \ , \tag{3.2}$$

where $\sqrt{\overline{u^2}}$ = axial turbulent velocity fluctuation,
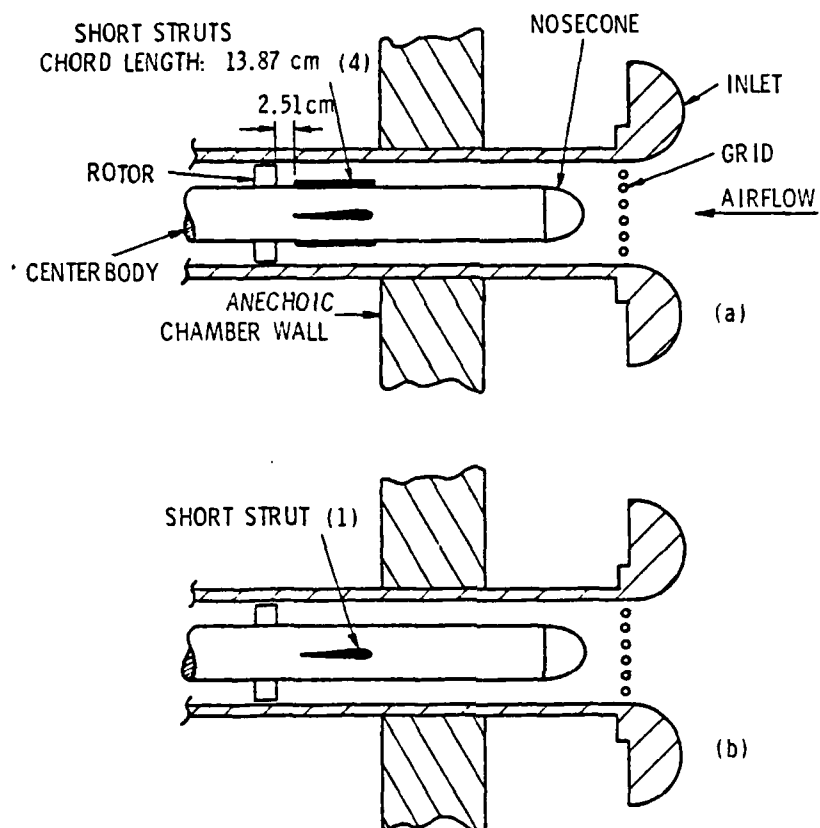
Figure 7. Inlet Annulus Configuration for Vortex Flow Noise Study.
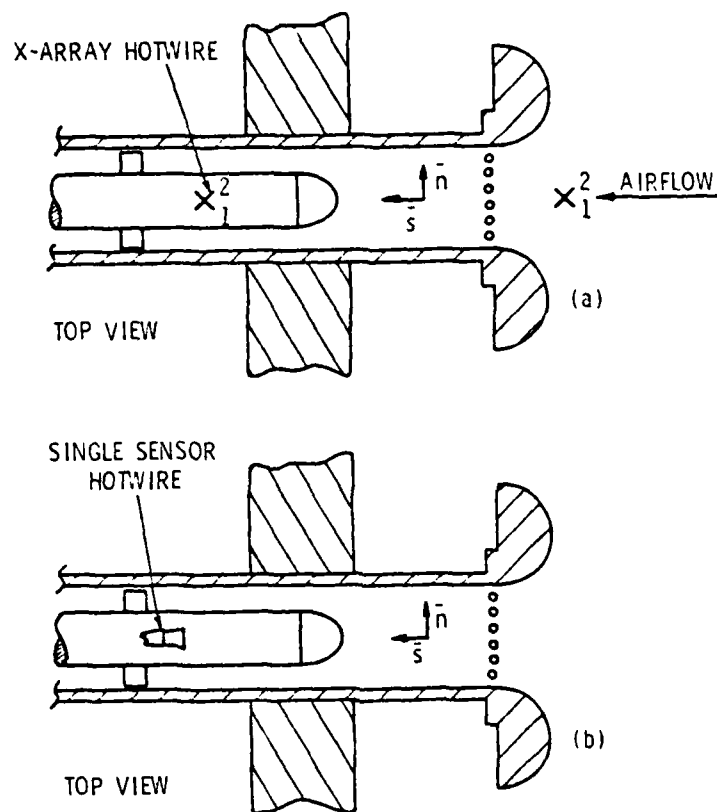
Figure 8. Probe Orientation for Inlet Turbulence Measurements.

$$T = \int\limits_{0}^{\infty} \rho_{uu}(\tau)d\tau \quad \cdot \qquad (3.3)$$

The term $\rho_{uu}(\tau)$ is defined as follows:

$$\rho_{uu}(\tau) = \overline{u(x,r,k,t)u[x,r,k,(t + \tau)]}/\overline{u^2} \qquad (3.4)$$

Assuming that turbulent eddies were convected at the same velocity as the mean flow, the length scale was determined by multiplying the integral time scale by the local mean axial velocity.

Figure 9 is a diagram of the hot wire instrumentation setup. All measurements were taken in the real time reference frame. Root mean square voltages were integrated over a 100 second time period, which resulted in a measurement error of less than 0.6 percent. The turbulent energy spectra were measured by averaging the signals over 1024 ensembles from 0-20 kHz with a 40 Hz bandwidth. This resulted in a 3.1 percent random error in the data.

        3.2.2.2 <u>Strut wake</u>. Measurements of the strut wake were conducted with a single sensor hot wire probe. With the probe oriented as shown in Figure 8b, the resultant mean velocity, turbulence intensity, and axial length scales were measured. The turbulent velocity was calculated as follows:

$$\sqrt{\overline{q^2}} = \frac{4\overline{E}\ \sqrt{\overline{e^2}}\ \sqrt{U_{rx}}}{B} \ , \qquad (3.5)$$

where $\sqrt{\overline{q^2}}$ = fluctuating turbulent velocity $(= \sqrt{\overline{u^2} + \overline{w^2}}$,

        $\overline{E}$ = DC part of anemometer voltage,

        $\overline{e}$ = AC part of anemometer voltage,
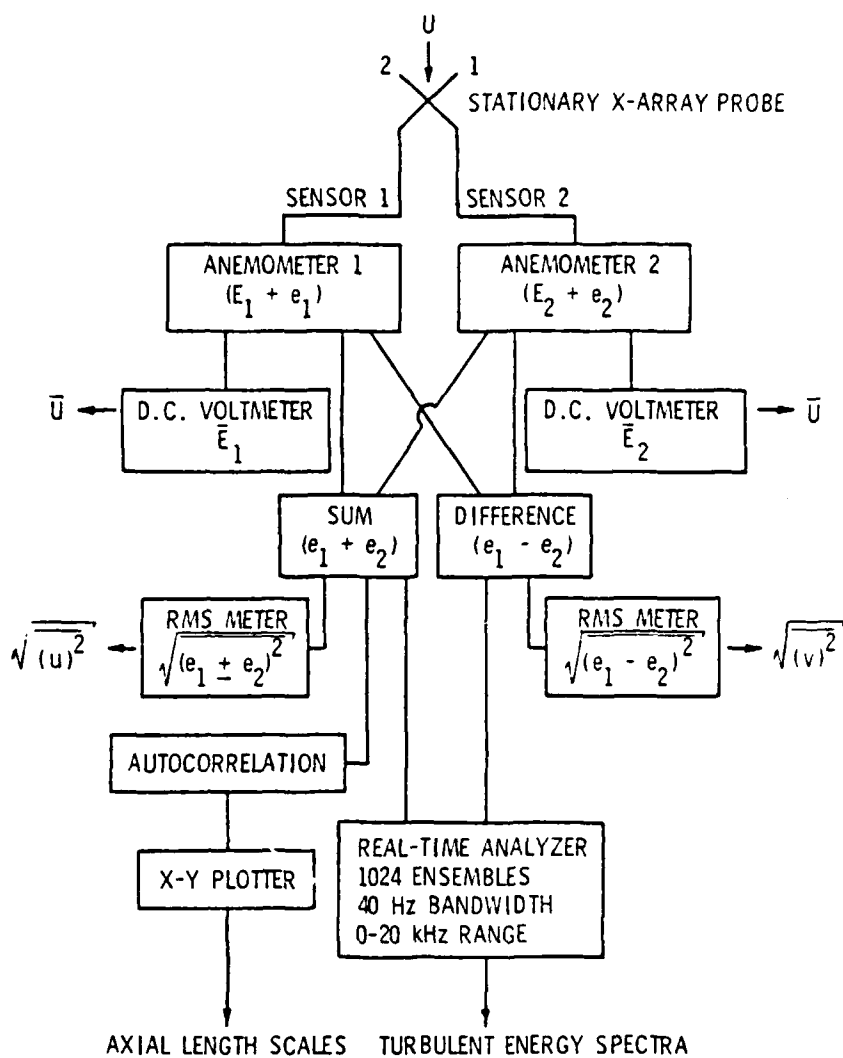
Figure 9. Diagram of Flow Instrumentation for Inlet Turbulence Measurements.

$\sqrt{\overline{v^2}}$ = tangential turbulent velocity fluctuation,

$\overline{E}$ = DC part of anemometer voltage (same for both sensors),

e_1, e_2 = AC part of anemometer voltages,

B = slope of King's Law equation for sensors

$$(\overline{E} + e_1)^2 = E_o^2 + B\sqrt{\overline{v}} ,$$

γ = angle between wire and axial direction,

U_x = local free stream axial velocity,

V = velocity normal to the wire,

and E_o = DC voltage at zero mean velocity.

Equations (3.1) and (3.2) were derived on the basis that the two sensor calibration curves are identical. This was accomplished by applying a DC bias to the output of one sensor's signal. The calibration curves of both sensors were checked before and after each set of measurements to ensure that no shift had occurred.

The orientation of the X-array probe is illustrated in Figure 8a. The probe was positioned such that the angle between the mean axial velo-city vector and the sensor was 45 degrees. Thus, for all measuring sta-tions, the plane containing the two sensors was defined streamwise $(\vec{s})$ and normal to the streamwise $(\vec{n})$ vectors.

The axial integral length scale of turbulence was obtained by ana-lyzing the sum of the two sensors' outputs with a correlation function computer to acquire the autocorrelation function. The correlation func-tion computer had a low-cutoff frequency of 0.16 Hz. From the correla-tion function compuer, the autocorrelation was recorded with an x-y plotter. As expressed by Tennekes and Lumley[31] in Equation (3.3), an integral time scale was calculated by integrating the autocorrelation curve:

$$B = \text{slope of King's Law equation,}$$

and $\quad U_{rx} = \text{resultant mean velocity} = \sqrt{U_x^2 + U_r^2}$.

The single sensor probe was calibrated before and after each set of measurements to ensure that no drift occurred.

The wake structures due to three rotor/strut spacings were measured. On the 47.63 cm long centerbody, the spacings between the rotor and strut were varied from 18 percent to 91 percent and 182 percent of the strut chord. The 18 percent and 91 percent chord settings were repeated with a shorter 26.35 cm centerbody. This shorter centerbody with its thinner boundary layer produced a weaker vortex flow. By comparing the same rotor-to-strut separation distances on the long and short center-bodies, the measured change in the vortex flow strength could then be correlated with the ovserved change in the noise spectra. The location of the probe is illustrated in Figure 10. In this figure, the probe/strut distance corresponds to the rotor/strut distance for which the noise spectra were obtained.

Two sets of measurements were made. In the first set, measurements were taken along a 90-degree arc bisected by the wake centerline at two radii-one at mid-span of the strut and the other within the inner wall boundary layer (8 percent of the strut span). Measurements were made with and without the inlet grid. The second set of measurements were to determine the wake structure for all four struts. This was accomplished by conducting a 360-degree tangential survey of the flow. The surveys were done at three radii--54 percent, 75 percent, and 95 percent of the rotor tip radius. Measurements were made for the three rotor-strut spac-ings on the long centerbody only. No grid was used to alter the inlet turbulence.
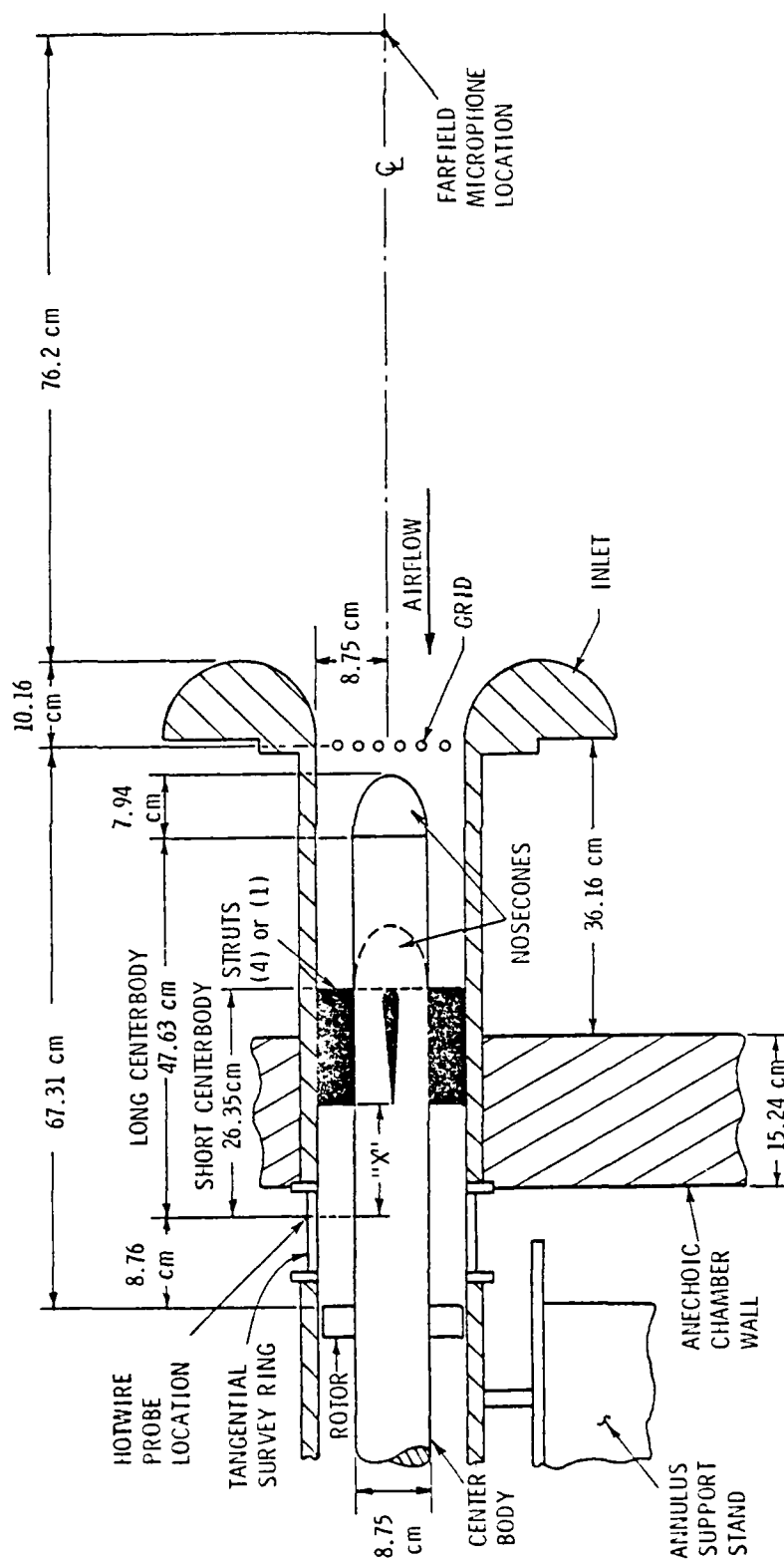
Figure 10. Probe Location for Strut Wake Measurements.

The flow instrumentation for the wake measurements is shown in Figure 11. The techniques used to obtain the rms values of the voltages, the axial length scales, and the turbulent energy spectra were the same as that used for the inlet turbulence measurements.

3.2.2.3 Vortex flow. Figure 12 shows the position of the X-array probe that was used in the final phase to measure vortex flow. As a result of the three dimensional nature of this flow, turbulence intensities could not be determined with Equations (3.1) and (3.2). These equations were derived on the assumption that the mean velocity vector formed a 45-degree angle with both hot wire sensors. This assumption is no longer valid for this type of flow. Consequently, the turbulence intensities were determined using Klatt's[32] equations for an X-array probe operating in an oblique flow. The components of turbulence intensity are calculated as follows:

$$\frac{\sqrt{\overline{q^2}}}{U_\infty} = \left[H_1^2 e_1^2 + H_1 H_2 \frac{K_{12}^2 - 1}{K_{12}^2 + 1} (\overline{e_1^2} + \overline{e_2^2}) + H_2^2 \overline{e_2^2} \right]^{1/2} \tag{3.6}$$

and

$$\frac{\sqrt{\overline{v^2}}}{U_\infty} = \left[H_1^2 e_1^2 - H_1 H_2 \frac{K_{12}^2 - 1}{K_{12}^2 + 1} (\overline{e_1^2} + \overline{e_2^2}) + H_2^2 \overline{e_2^2} \right]^{1/2} , \tag{3.7}$$

where

$$K_{12} = \sqrt{\frac{\overline{(e_1 + e_2)^2}}{\overline{(e_1 - e_2)^2}}} ,$$
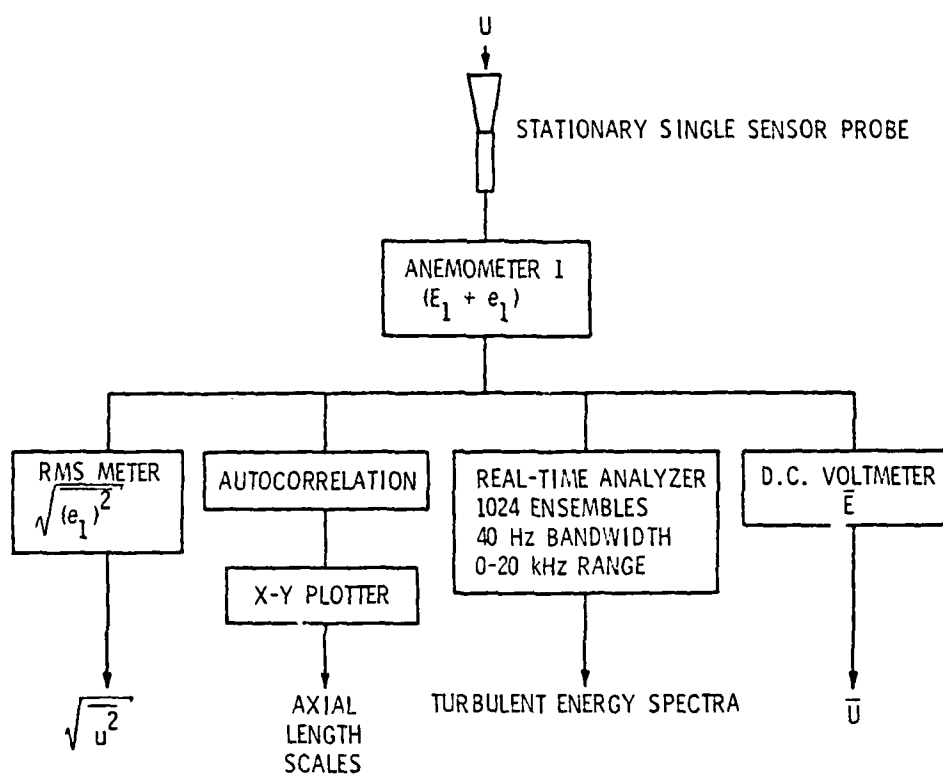
Figure 11.   Instrumentation for Strut Wake Measurements.
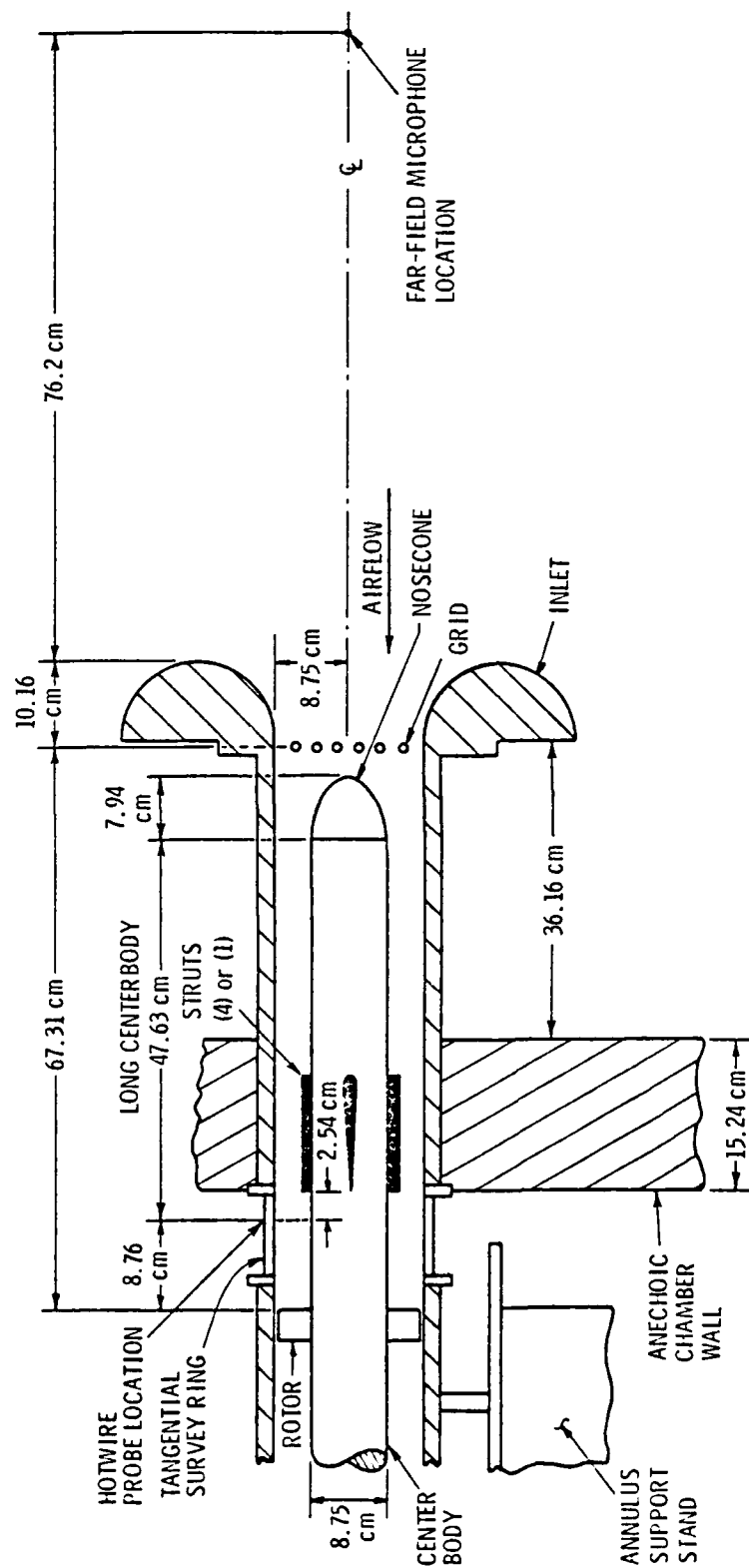
Figure 12. Probe Location for Vortex Flow Measurements.

$$H_1 = \frac{\overline{E_1}}{\eta_1 (\overline{E_1^2} - E_{o_1}^2)} \left[\frac{\overline{E_1^2} - E_{o_1}^2}{\overline{E_{1_\infty}^2} - E_{o_1}^2} \right]^{1/\eta_1} \quad ,$$

$$H_2 = \frac{\overline{E_2}}{2 (\overline{E_2^2} - E_{o_1}^2)} \left[\frac{\overline{E_1^2} - E_{o_2}^2}{\overline{E_{2_\infty}^2} - E_{o_2}^2} \right]^{1/\eta_2} \quad ,$$

and

$\frac{\sqrt{\overline{q^2}}}{U_\infty}$ = resultant turbulence intensity $\sqrt{\overline{q^2}} = \sqrt{\overline{u^2} + \overline{w^2}}$,

$\frac{\sqrt{\overline{v^2}}}{U_\infty}$ = tangential turbulence intensity ,

$\overline{e}$ = AC part of anemometer voltage ,

$\overline{E}$ = DC part of anemometer voltage ,

η = exponent in King's Law equation: $E^2 = E_o^2 + Bu^\eta$,

and

Subscripts

1,2 = distinguish the sensors 1 and 2 of the X-array probe.

The instrumentation and calibration procedures used were the same as those employed in the inlet turbulence phase of the investigation. Due to the three dimensional nature of the flow, the two sensor probes measure the vector sum of the radial and axial components of velocity and turbulence intensity. The tangential components were not altered.

3.2.2.4 <u>Error analysis for hot wire measurements</u>. For the
data obtained with the single and X-array hot wire probes, the following
sources of error may occur. The magnitude and the action taken to reduce
the error when necessary are presented.

1. An error results due to a deviation from the cosine law
   resulting from changes in the effective cooling velocity
   of the hot wire sensor. This error was eliminated by
   employing the appropriate correction factor described
   in Reference [18].

2. An error results due to flow interference due to probe
   geometry on the heat transfer characteristics of the
   sensor. For the probes used in this investigation, these
   error sources were negligible. The error was accounted
   for during the probe calibration.

3. Error from changes in the heat transfer characteristics
   of the hot wires due to wire aging, oxidation, and con-
   tamination can result. Errors resulting from this
   source were eliminated by calibrating the probes before,
   during, and after each experimental run.

4. Errors result in the hot wire calibration curves due to
   changes in the ambient air temperature. Errors of this
   type were eliminated by the technique mentioned above
   in Item 3.

5. Errors result from the spatial resolution of the probe.
   The expected maximum calculated errors in the mean velo-
   city and turbulence data are estimated to be ±2.0 per-
   cent and ±4.0 percent, respectively. The method used to

calculate the magnitude of these errors followed the procedure used by Anand and Lakshminarayana[33], and Reynolds and Lakshminarayana[34]. Analysis of the data indicated that the actual variation in the mean velocity and turbulence levels were well within these limits.

3.2.3 Acoustic measurements. Measurements of the noise produced by the rotor were conducted in the far field region with a 0.64 cm Brüel and Kjaer condensor microphone. The microphone was on the annulus centerline 76.2 cm in front of the inlet. The microphone signal was analyzed with a General Radio wave analyzer with a 10 Hz bandwidth to yield the sound pressure spectra and the relative dB levels of the rotor and strut blade passing harmonics. The sound pressure spectra were analyzed over a range of 0 to 5.0 kHz and the output recorded on a graphic level recorder. The relative dB levels of the harmonic peaks were measured by analyzing the sound pressure at a given rotor or strut blade passing harmonic, then taking the mean square average of the analyzer output voltage. Acoustic data were gathered for all the previously mentioned flow configurations with the exception of the inlet turbulence case.

The acoustic response of the inlet annulus was of great interest due to the significant length of the annulus. Because size prohibited the placing of an adequate source in the annulus, the principle of reciprocity was used. The reciprocity principle states that a source and receiver may exchange positions without altering the sound field. Thus, the receiving microphone was placed in the annulus where the rotor was

normally located and a speaker (source) was positioned in the anechoic chamber where the microphone was normally located.

Calibration of the inlet annulus was performed by driving the speaker at several pure tones in the frequency range of interest and recording the sound pressure measured by the microphone in the annulus. The procedure was repeated with the microphone for chamber calibration placed in the chamber with the speaker. The distance between the microphone and speaker was kept constant for both annulus and chamber measurements. The annulus response was calculated by taking the ratio of sound pressure response in the annulus to the sound pressure response in the chamber as given by the following equation:

$$\text{Annulus Response (dB)} = 20 \log \frac{P_2}{P_o} - 20 \log \frac{P_1}{P_o} = 20 \log \frac{P_2}{P_1}, \qquad (3.8)$$

where P_o = reference sound pressure 2×10^{-5} N/m^2,

P_1 = sound pressure when microphone is in the annulus,

and P_2 = sound pressure when microphone is in the chamber.

The basic configurations shown in Figures 5, 6, and 7 were tested with and without flow. Results of these tests indicate that the configuration changes had little effect on the acoustic response of the annulus. It was also found that presence of flow did not significantly alter the annulus response, which was due to the low Mach number of the flow. The acoustic response is shown in Figure 13. The peak at 3.8 kHz corresponds to the first radial mode of the annulus--roughly a wavelength of twice the size of the annulus. Since the measured spectra end at a frequency of 5.0 kHz, the peak of 6.3 kHz, which corresponds to a higher
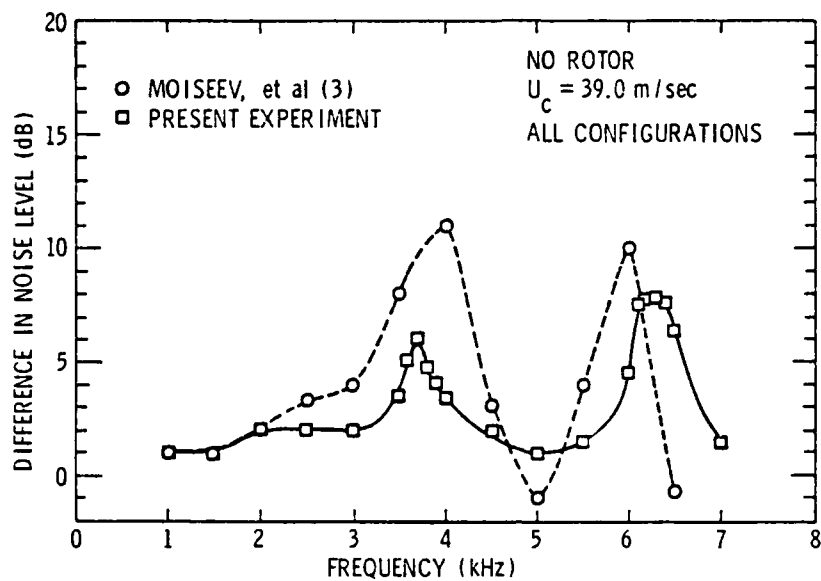
Figure 13. Acoustic Response of the Inlet Annulus.

annulus mode, is of no importance to this investigation. Finally, the
sound pressure spectra illustrated in the following chapter were not
corrected to remove the annulus effect.

3.2.4 Error analysis for acoustic measurements. The sources of
error which may occur in the acoustic data are listed below. The magni-
tude of each error was calculated and is presented below:

1. Microphone response error results due to changing ambient
   air temperature. The temperature coefficient for the con-
   densor microphone was ±0.01 dB/C degrees between 20 degrees
   C to 30 degrees C. This error was negligibly small.

2. Error due to ambient pressure changes result. This error
   was less than 0.1 dB for a 10 percent change in atmospheric
   pressure. Errors of this type were, therefore, negligibly
   small.

3. Errors result in acoustic measurements due to humidity
   changes. Magnitude of this error was ±0.1 dB and, thus,
   was negligibly small.

4. Errors result from the finite sampling time of the
   spectrum analyzer. The magnitude of this error was
   ±1.0 dB at blade passing frequency and its multiples.

5. Errors result from contamination of the sound spectrum
   by background noise. This error was negligibly small
   at frequencies above 200 Hz, based on measured signal-
   to-noise levels.

CHAPTER IV

INTERPRETATION OF EXPERIMENTAL RESULTS

A summary of the aerodynamic and acoustic measurements for each of
the three phases of this investigation are shown in Tables 3, 4, and 5.
In each table, information on probe location, annulus configuration and
inlet turbulence modification is presented. Also included are the free
stream values of mean axial velocity, axial and tangential components of
turbulence intensity, and axial length scale of turbulence at mid radius.
When the struts are present, the above values at the wake centerline are
also shown. All tests were done with a 17-bladed rotor operating at
5440 rpm and a flow coefficient of $\phi = 0.75$. A detailed description of
the aerodynamic and acoustic data follows.

4.1 Inflow Turbulence Characteristics

The results of the mean velocity profile measurements are shown in
Figures 14 and 15. In Figure 14, the axial velocities at stations 3 and
4 are nondimensionalized with respect to the axial velocity at the annu-
lus centerline $\lambda = 90$ degrees). At station 4 (17.6 cm upstream of inlet),
this velocity is $U_c = 1.79$ m/sec. The axial velocity corresponding to
station 3 (10.3 cm upstream of inlet) is $U_c = 4.04$ m/sec. The increase
of the velocity ratio as the probe moves from $\lambda = 90$ degrees to $\lambda =$
0 degrees indicates that the cross sectional area is decreasing. The
significance of this variation of the cross sectional area will be dis-
cussed later.

The axial mean velocity profiles at stations 1 and 2 are shown in
Figure 15. The free stream velocities at station 1 (6.7 cm upstream of
rotor) and station 2 (31.4 cm upstream of rotor) are 35.8 m/sec and

TABLE 5

SUMMARY OF VORTEX FLOW MEASUREMENTS

Incidence	r/r_t	Vortex Location Suction Side Y	Vortex Location Pressure Side Y	Wake Location Y	Wake Velocity Defect A	Vortex Max. Tangential Velocity Suction Side U_θ/U_c	Vortex Max. Tangential Velocity Pressure Side U_θ/U_c	Wake Turbulence $\sqrt{\bar{u}^2}/U_c$	Wake Turbulence $\sqrt{\bar{v}^2}/U_c$	Vortex Turb. Suction Side $\sqrt{\bar{u}^2}/U_c$	Vortex Turb. Suction Side $\sqrt{\bar{v}^2}/U_c$	Vortex Turb. Pressure Side $\sqrt{\bar{u}^2}/U_c$	Vortex Turb. Pressure Side $\sqrt{\bar{v}^2}/U_c$	One Guidevane 1st BPF Tone SPL (dB)	One Guidevane 2nd BPF Tone SPL (dB)	One Guidevane 3rd BPF Tone SPL (dB)	Four Guidevanes 1st BPF Tone SPL (dB)	Four Guidevanes 2nd BPF Tone SPL (dB)	Four Guidevanes 3rd BPF Tone SPL (dB)
12°	.52	0.6	1.9	1.6	0.14	.44	.06	.065	.046	.041	0.37	.071	.049	*	*	*	*	*	*
	.55				0.13	.42	-.03	.064	.055	.017	.038	.052	.05	*	*	*	*	*	*
	.57				0.14	.29	.01	.065	.053	.044	.041	.052	.044	*	*	*	*	*	*
	.59				0.18	.22	.03	.053	.047	.068	.048	.047	.035	*	*	*	*	*	*
	.61				0.24	.09	.04	.067	.046	.048	.043	.045	.023	83	NP[2]	NP	82.8	74	NP
4°	.65	-0.1	1.0	0.4	0.16	.27	.03	.061	.053	.032	.031	.06	.041	84.6	NP	NP	83.4	NP	NP
0°	.55	-0.6	0.6	0.0	0.24	.04	.08	.069	.053	.027	.02	.027	.02	81.9	NP	NP	83.6	NP	NP
-12°	.52	-0.6	-1.7	-0.6	0.16	-.49	-.09	.069	.049	.055	.039	.07	.053	87.6	NP	NP	85	NP	NP
	.55				0.14	-.41	-.06	.06	.06	.047	.035	.067	.05	*	*	*	*	*	*
	.57				0.12	-.30	-.03	.06	.057	.067	.047	.063	.049	*	*	*	*	*	*
	.59				0.12	-.12	-.03	.054	.048	.075	.064	.052	.035	*	*	*	*	*	*

Notes: 1 – U_c = 39 m/sec

2 – NP – Not Present

51
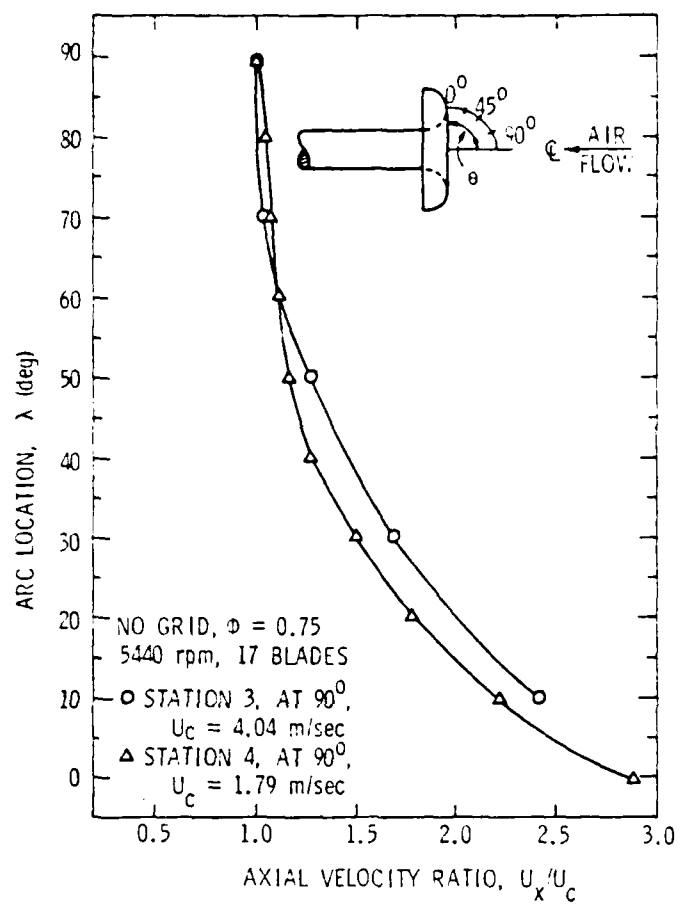
Figure 14.   Mean Velocity Profiles Upstream of the Inlet
(Stations 3 and 4).
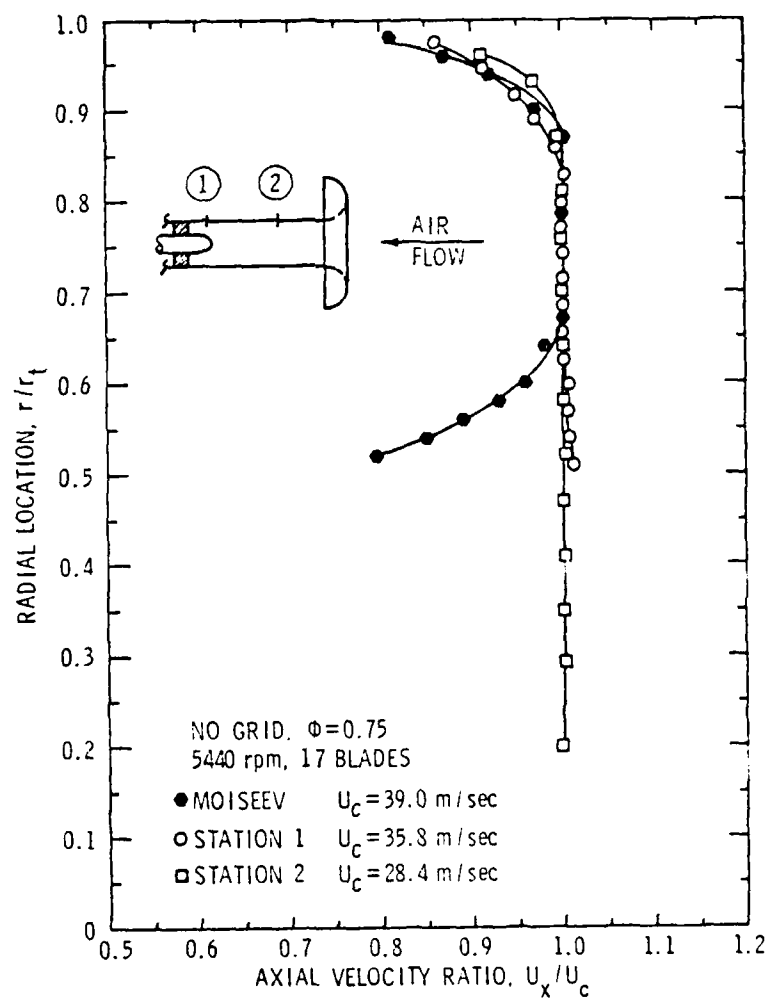
Figure 15. Mean Velocity Profiles Downstream of the Inlet (Stations 1 and 2).

Figure 16. Axial Turbulence Intensities Upstream of the Inlet (Stations 3 and 4).

Figure 17. Tangential Turbulence Intensities Upstream of the Inlet (Stations 3 and 4).

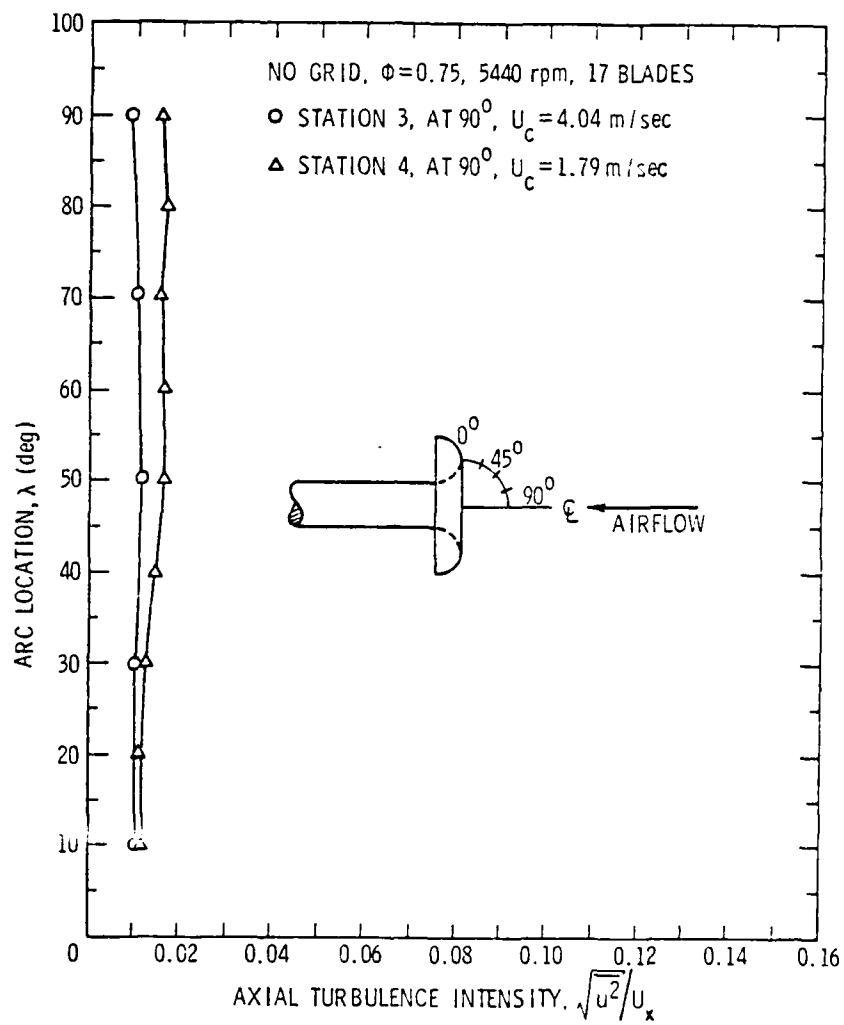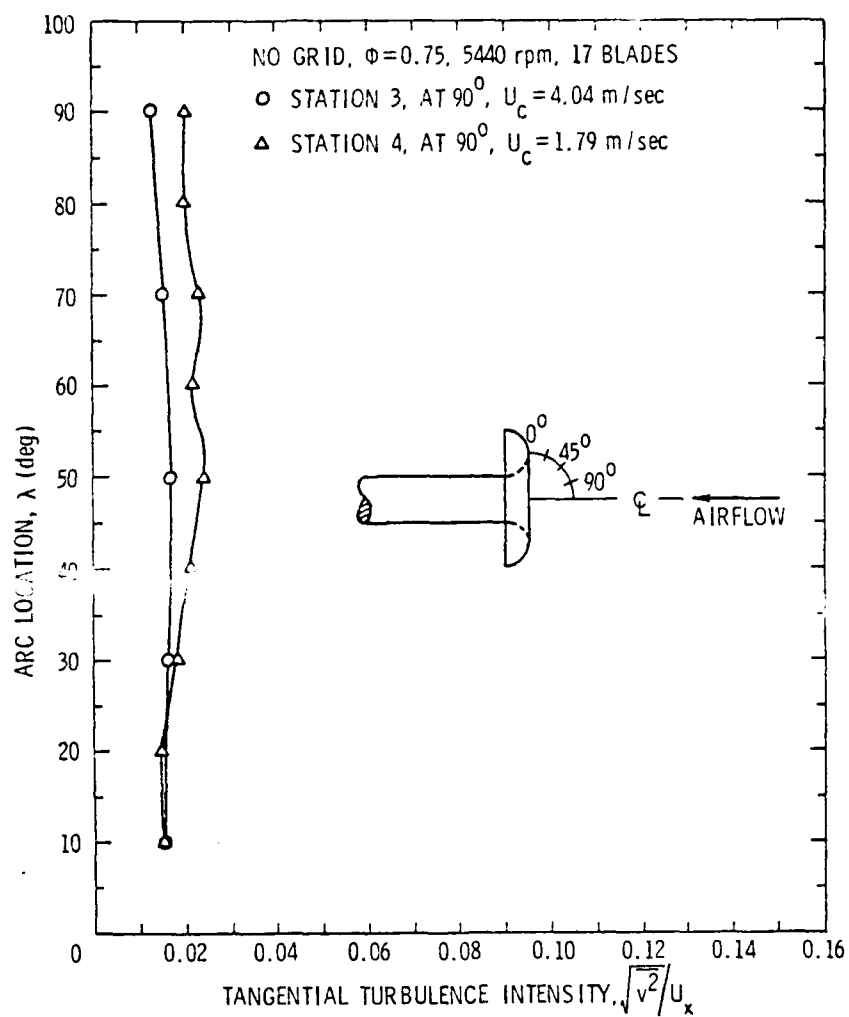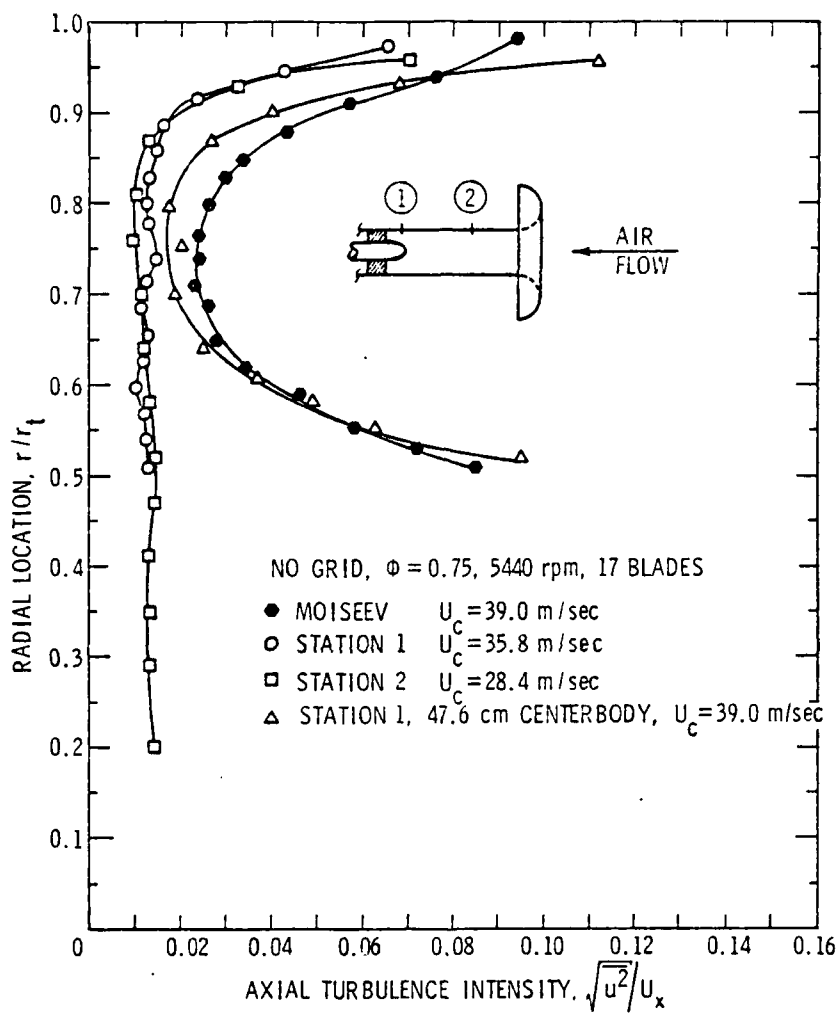Figure 18. Axial Turbulence Intensities Downstream of the Inlet, No Grid (Stations 1 and 2).
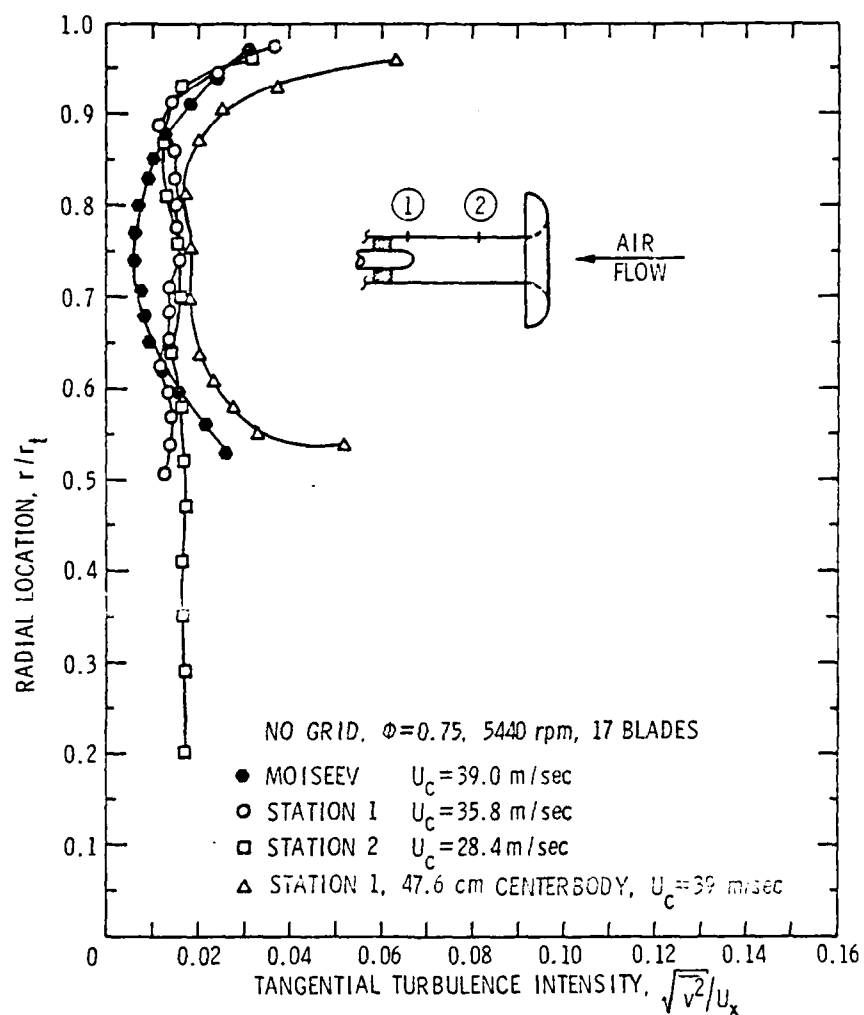
Figure 19. Tangential Turbulence Intensities Downstream of the Inlet, No Grid (Stations 1 and 2).

28.4 m/sec, respectively. No boundary layer is observed in the center

body region at station 1, since the centerbody is rotating. Also shown

in Figure 15 is the velocity profile for the case of a fully developed

boundary layer measured by Moiseev et al.[4]. In this configuration,

the rotating centerbody was replaced with a stationary centerbody

47.63 cm long. The resulting thicker boundary layers on the centerbody

and annulus walls are evident in Figure 15.

The variations of the axial and tangential components of turbulence

intensity as a function of probe immersion are shown in Figures 16, 17,

18, and 19. Starting upstream of the inlet at station 4, the initial

turbulence was found to be weakly nonisotropic.

For the downstream stations 3, 2, and 1, the same degree of non-

isotropy was found. The tangential intensity was slightly higher than

the axial component. The magnitude of the axial turbulence intensity at

the inlet is seen to decrease from 1.7 percent to 1.0 percent at sta-

tion 1. The corresponding change in the tangential component of turbu-

lence was from an inlet value of 2.3 percent to a value of 1.3 percent

at station 1. Finally, the decrease in both axial and tangential tur-

bulence intensities, seen in Figures 16 and 17, as the probe angle λ

decreases is the result of reduced cross sectional area discussed earlier.

Also shown in Figures 18 and 19 are the turbulence intensity pro-

files for the case of a stationary, 47.63 cm long centerbody. Data were

taken at station 1 with the long-centerbody replacing the short rotating

spinner. Both the present set of measurements, as well as those done by

Moiseev et al.[4], are presented. What is evident in these figures is

the increase in both components of turbulence intensity in the boundary

layer regions (centerbody and annulus walls) and the free stream region.

The discrepancy between the present data and that obtained by Moiseev et al.[4] is believed to be due to the modification made to the anechoic chamber air inlet, which was discussed earlier in Chapter III. This modification altered the structure of the atmospheric turbulence from that which Moiseev et al.[4] measured.

To verify whether the trends exhibited by the axial and tangential components of turbulence intensity while passing through a contraction are correct, the data are compared to the theory by Ribner and Tucker[35]. The behavior of turbulent velocities $\overline{u^2}$ and $\overline{v^2}$ in an axisymmetric contraction were determined by the following equations:

$$\frac{\overline{u_B^2}}{\overline{u_A^2}} = \frac{3}{4\ell_1^2} \left[\frac{-1}{1 - \epsilon} + \frac{2 - \epsilon}{(1 - \epsilon)^{3/2}} \tanh^{-1} \sqrt{1 - \epsilon} \right] \qquad (4.1)$$

and

$$\frac{\overline{v_B^2}}{\overline{v_A^2}} = \frac{3}{8\ell_2^2} \left[\frac{2 - \epsilon}{1 - \epsilon} - \frac{\epsilon^2}{(1 - \epsilon)^{3/2}} \tanh^{-1} \sqrt{1 - \epsilon} \right], \qquad (4.2)$$

where $\overline{u_A^2}$, $\overline{u_B^2}$ = mean square of the axial turbulent velocity fluctuation upstream and downstream of the contraction,

$\overline{v_A^2}$, $\overline{v_B^2}$ = mean square of the tangential turbulent velocity fluctuation upstream and downstream of the contraction,

ℓ_1 = axial velocity upstream of the contraction divided by axial velocity downstream of the contraction,

ℓ_2 = width of stream before the contraction divided by width after the contraction,

and ϵ = contraction parameter (ℓ_2^2/ℓ_1^2).

A comparison of experimental measurements with the theory is shown in Figure 20. Results from expressions in Equations (4.1) and (4.2) agree closely with the experimental data.

The effect of a grid placed at the inlet on the turbulence is shown in Figure 21. The axial and tangential components of turbulence intensity are plotted for stations 1 and 2, as well as the data obtained with the long stationary centerbody by Moiseev et al.[4]. By comparing the grid and no grid cases, it is seen that the presence of the grid increases the axial intensities by a factor of six and the tangential intensities by a factor of three in the vicinity of the grid (station 2). This results in a more isotropic flow as indicated by the ratio $\overline{v^2}/\overline{u^2}$ at station 2 (13.6 grid mesh sizes downstream) being 0.72, and at station 1 (2.22 grid mesh sizes downstream) being 0.84. In contrast to this, the long centerbody with grid shows a degree of nonisotropy of $\overline{v^2}/\overline{u^2} = 2.89$. Again, this nonisotropic flow is the result of a fully developed boundary layer present in the annulus.

The measured autocorrelation curves of the inlet turbulence are illustrated in Figures 22, 23, and 24. Using the method described in Chapter III, the length scales were calculated and are presented in Table 6. It is evident from this data that the length scales upstream of the inlet were on the order of the annulus diameter (17.50 cm). The turbulent length scales were drastically increased as the eddies were contracted from stations 4 to 1. The eddies stretched by a factor of 10. Also apparent in the data was a slight increase in the length scales in the region near the annulus wall. This eddy stretching was the result of boundary layer development on the wall.
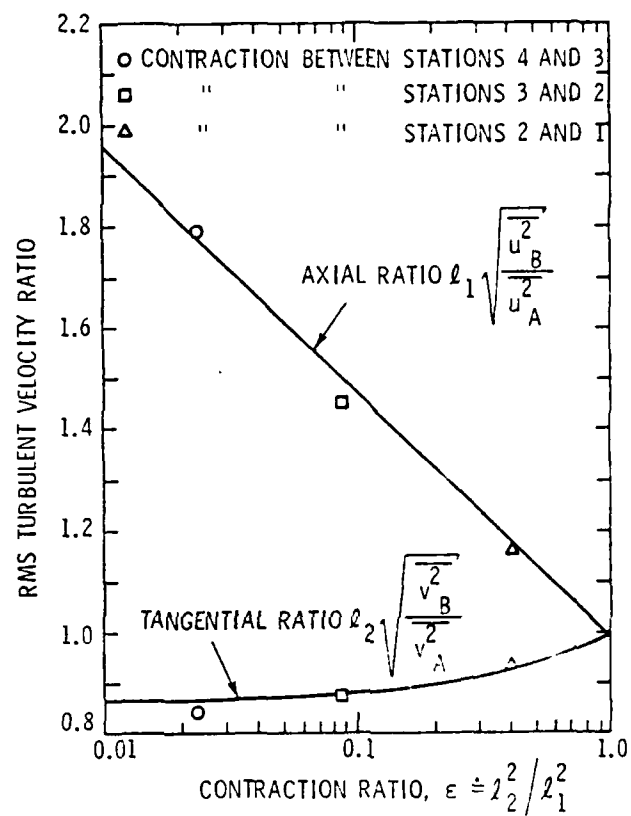
Figure 20. Comparison of Experimental Data to Ribner and Tucker Theory.
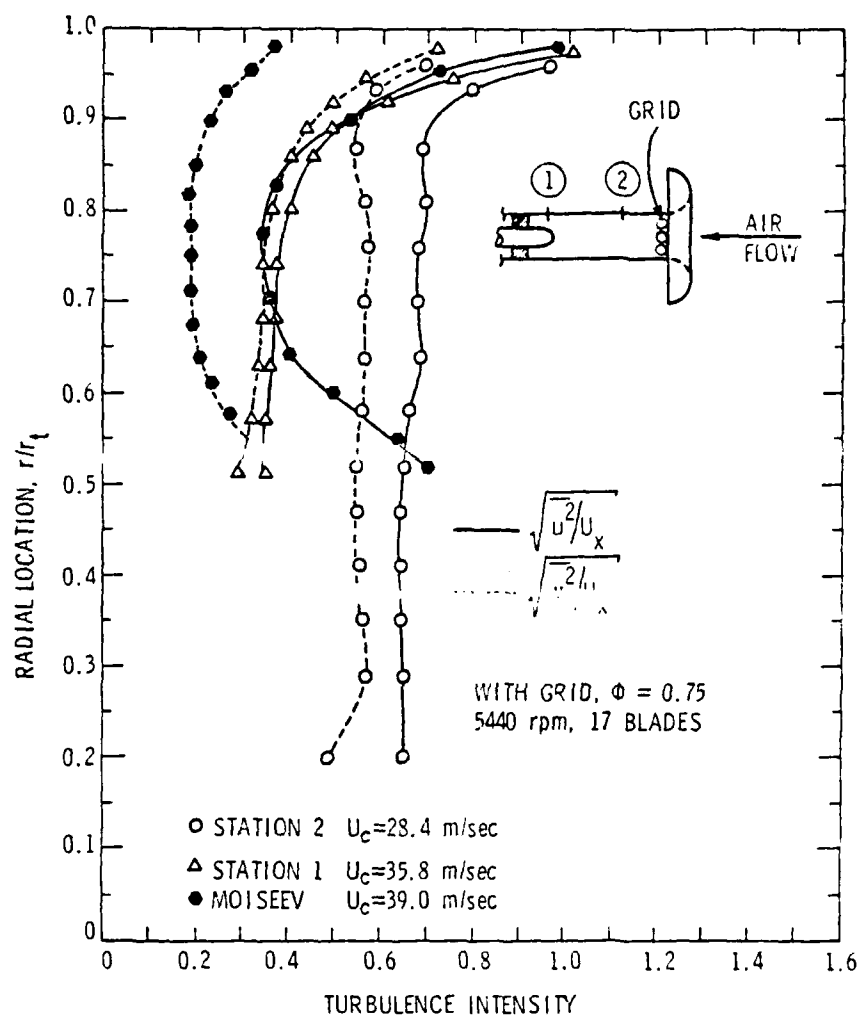
Figure 21. Axial and Tangential Intensities Downstream of Inlet,
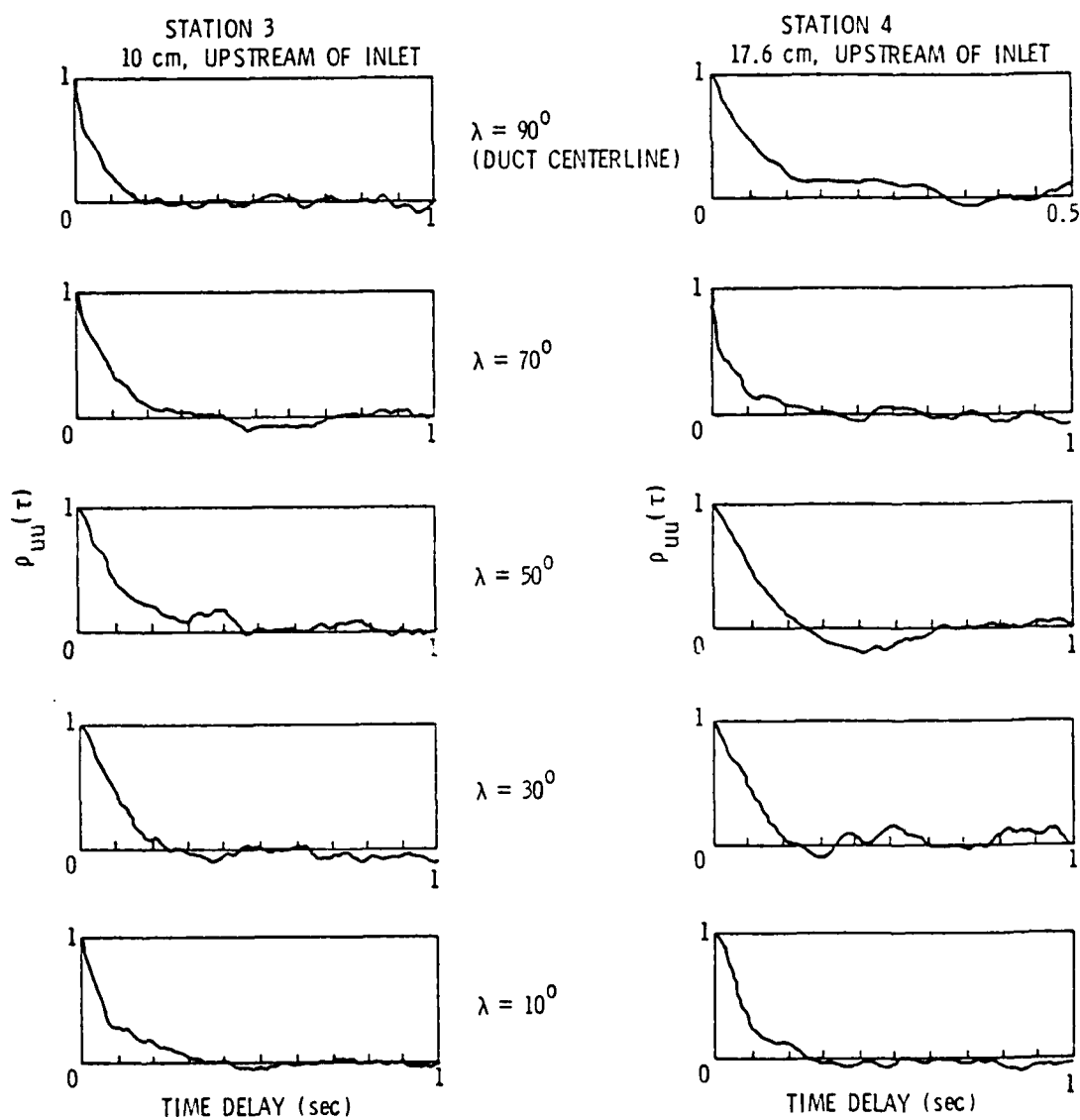With Grid Installed (Stations 1 and 2).

Figure 22. Auto-Correlation Curves for Flow Upstream of the Inlet
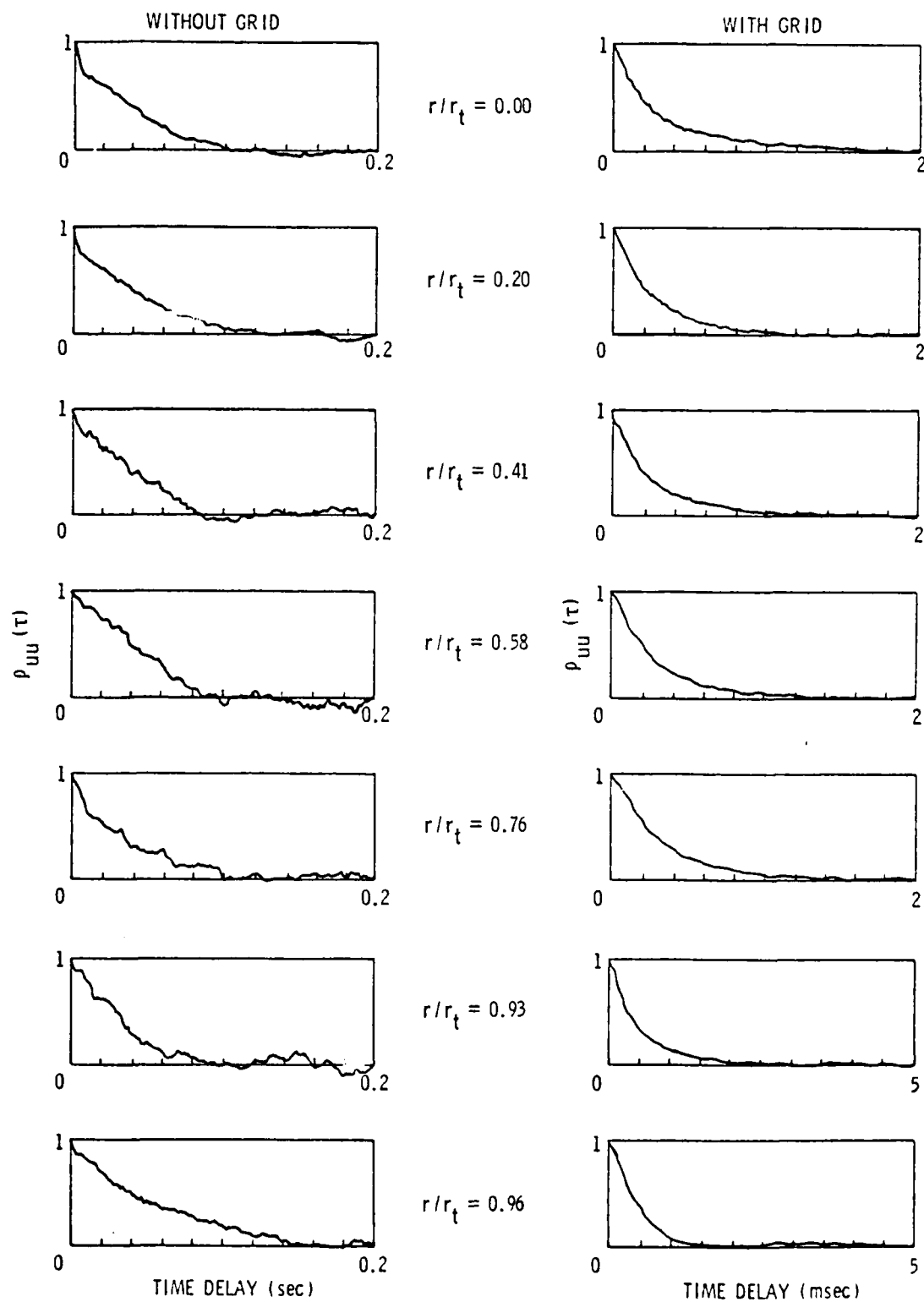(Stations 3 and 4).

Figure 23. Auto-Correlation Curves for Station 2, With and Without the Grid Installed.
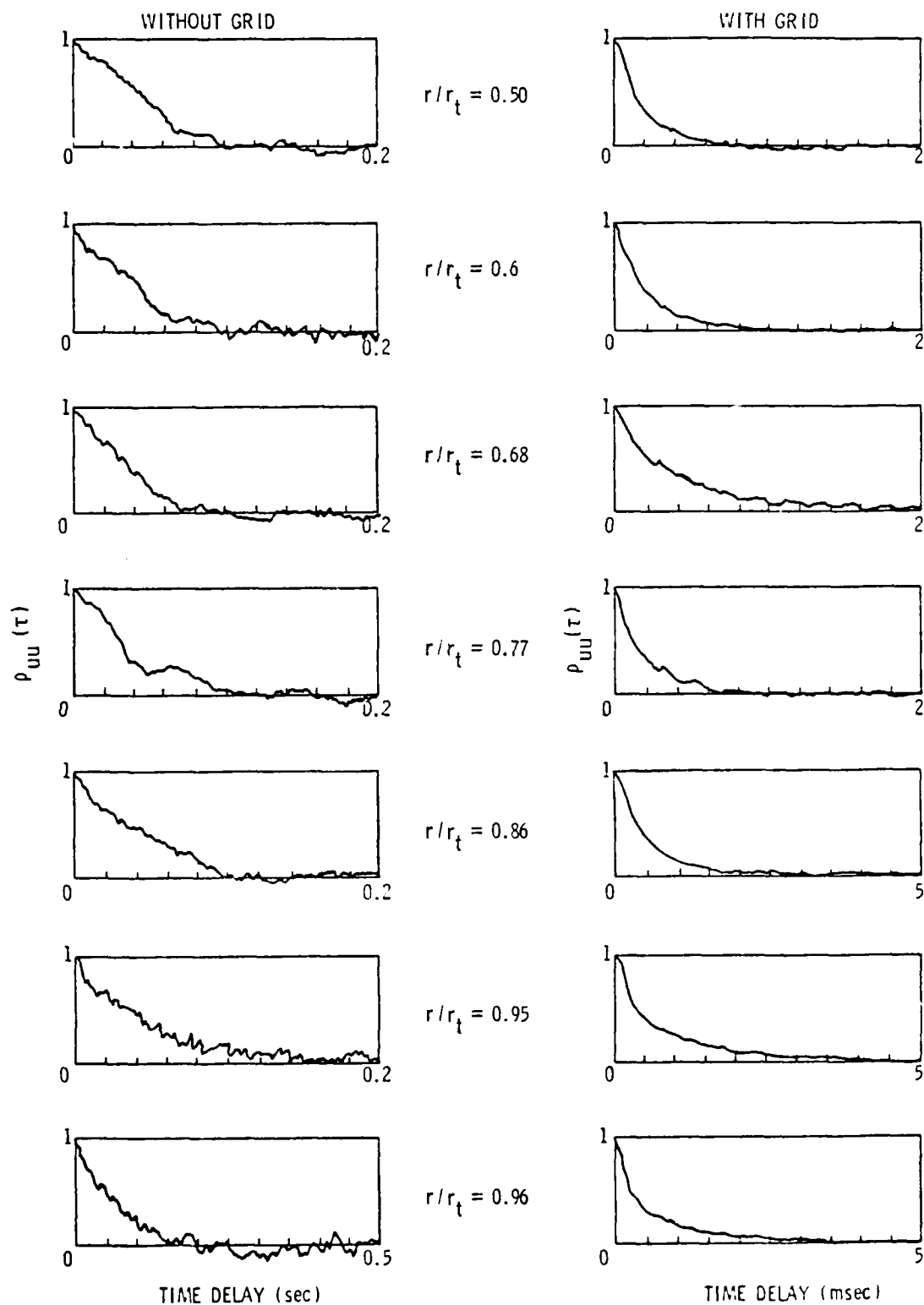
Figure 24. Auto-Correlation Curves for Station 1, With and Without the Grid Installed.

Based on the measurements made herein, a conceptual illustration of the elongation of turbulent eddies is shown in Figure 25.

In Table 6, the axial length scales at stations 1 and 2 are presented for the case of the grid installed. It is apparent that the grid reduced the length scales by tenfold. This data supports the concept that the grid tends to make the turbulence more isotropic by drastically reducing the length scale of the eddies resulting from the contraction.

4.1.1 Comparison of data to previous investigations. A comparison of inflow turbulence data reported here with the data obtained by other investigators is shown in Table 7. Each investigation is classified on the basis of the facility, configuration, data obtained, and other relevant parameters. Also listed for each investigation are the free stream values of both axial and tangential turbulence intensity, axial length scale of turbulence in the free stream velocity, flow coefficient, and the ratio of tip-to-axial Mach numbers.

In the present investigation, the structure of turbulence is seen to be weakly nonisotropic upstream of the inlet. The tangential component of turbulence intensity was found to be 50 percent greater than the axial intensity. Measurements of the axial length scale indicate that turbulent eddies have a significant size prior to distortion by the contracting inlet flow. At present, no prior investigations of the flow field upstream of an inlet are available for comparison with this data. In the region between the inlet and the centerbody, flow contraction results in a decrease in magnitude of both components of turbulence intensity. A greater decrease in the tangential intensity occurs as the turbulent eddy is stretched.

TABLE 6

SUMMARY OF INLET LENGTH SCALE MEASUREMENTS

Station 1 6.7 cm Upstream of Rotor			Station 2 31.4 cm Upstream of Rotor			Station 3 10.3 cm Upstream of Inlet		Station 4 17.6 cm Upstream of Inlet	
Radial Location r/r_t	Axial Length Scale No Grid (cm)	Grid (cm)	Radial Location r/r_t	Axial Length Scale No Grid (cm)	Grid (cm)	ARC Location (deg)	Axial Length Scale (cm)	ARC Location (deg)	Axial Length Scale (cm)
.51	188	7.26	0.00	137	9.23	90°*	57	90°*	16
.54	210	7.42	0.20	133	7.87	70°	53	80°	22
.57	210	7.73	0.29	127	8.28	50°	113	70°	18
.60	179	8.05	0.35	128	8.36	30°	77	60°	27
.63	136	8.11	0.41	131	8.03	8°	93	50°	25
.66	136	8.32	0.47	129	7.32			40°	27
.68	148	7.54	0.52	129	7.91			30°	34
.71	160	7.22	0.58	143	7.56			20°	43
.74	190	7.61	0.64	131	7.75			10°	31
.77	181	8.87	0.70	203	8.46			0°	30
.80	163	7.81	0.76	180	8.86				
.83	165	8.31	0.81	130	8.84				
.86	210	10.40	0.87	155	8.02				
.89	208	12.80	0.93	193	11.50				
.92	242	17.60	0.96	139	12.40				
.95	179	22.00							
.97	209	17.40							

TABLE 7

COMPARISON OF PRESENT DATA WITH THE DATA OF PREVIOUS INVESTIGATIONS

	Facility	Turbulence	Annulus Diameter (d)	Annulus Height Above Floor	Probe Type and Location	$\frac{I_x}{L_0}$	U_x m/sec	$\frac{\sqrt{u'^2}}{U_x}$	$\frac{\sqrt{v'^2}}{V_x}$	$\frac{H_t}{H_d}$	ϕ	N	$\frac{r}{t_L}$
(1) Shaw, Woodward, Glesmer, and Wang (Ref. 36)	Fan	Room	50.8 cm	2d	"X" Array Hotfilm 0.5d Downstream of Inlet Bo Centerbody	9.8-13.8d / N.A.²	116.0	0.5	5.0-5.8%	.62	.73	15	0.46
(2) Bekofske, Sweet and Wang (Ref. 35)	Fan	Room	50.4 cm	5d	"X" Array Hotfilm 1.0 Downstream at Inlet Bo Centerbody	Porous Wall 4.4-8.9d / .6-.3d; Non Porous 17.8-16d / 1.49 0.9d	476.0	1.7 ; 1.7	.6-1.4% ; 1.2-1.7%	$\frac{1.24}{.85}$	1.09	14	0.50
(3) Tronzo (This Investigation)	Fan	Room	17.78 cm	8.5d	"X" Array Hotfilm 2.6-8d Downstream of Inlet Bo Centerbody	7.3-11.4d / N.B.3	28.4	1.1-1.7% ; 1.7%	1.3-1.7%	$\frac{.15}{.11}$	.75	17	0.5
(4) Robbins (Ref. 15)	Fan	Room	17.78 cm	8.5d	"X" Array Hotwire Annulus 4.0/d Downstream at Inlet	N.H. ; N.H.	56.81	1.9%	2.5	$\frac{.15}{.17}$	1.14	17	0.5
(5) Tronzo (This Investigation)	Fan	Room	17.78 cm	8.5d	"X" Array Hotwire Annulus 4.0/d Downstream at Inlet	7.5-13.6d / N.H.	36.9	1.0-1.5%	1.3-1.62	$\frac{.15}{.11}$	0.75	17	0.5

TABLE 7 (continued)

	Facility	Turbulence	Annulus Diameter (d)	Annulus Height Above Floor	Probe Type and Location	$\frac{L_x}{L_0}$	U_x m/sec	$\frac{\sqrt{\overline{u^2}}}{U_x}$	$\frac{\sqrt{\overline{v^2}}}{V_x}$	$\frac{N_t}{M_a}$	ϕ	N	$\frac{r}{r_t}$
(1) Shaw, Woodward, Glasner, and Wang (Ref. 36)	Fan	Room	50.8 cm	2d[1]	"X" Array Hotfilm 0.5d Downstream of Inlet No Centerbody	$\frac{9.8-13.8d}{N.A.[2]}$	116.0	0.5	5.0-5.8%	.62	.73	15	0.46
(2) Bekofske, Sheer and Wang (Ref. 35)	Fan	Room	50.4 cm	5d	"X" Array Hotfilm 1.0d Downstream of Inlet No Centerbody	Porous Wall $\frac{4.4-8.9d}{.6-.3d}$ Non Porous $\frac{17.8-30d}{1.49-0.9d}$	476.0	1.7 1.7	.6-1.4% 1.2-1.7%	$\frac{1.24}{.85}$	1.09	44	0.50
(3) Trunzo (This Investigation) (This Investigation)	Fan	Room	17.78 cm	8.5d	"X" Array Hotfilm 2.68d Downstream of Inlet No Centerbody	$\frac{7.31-11.4d}{N.M.[3]}$	28.4	1.1-1.7%	1.3-1.7%	$\frac{.15}{.11}$	.75	17	0.5
(4) Robbins (Ref. 15)	Fan	Room	17.78 cm	8.5d	"X" Array Hotwire Annulus 4.07d Downstream of Inlet	$\frac{N.M.}{N.M.}$	56.81	1.9%	2.5	$\frac{.15}{.17}$	1.14	17	0.5
(5) Trunzo (This Investigation)	Fan	Room	17.78 cm	8.5d	"X" Array Hotwire Annulus 4.07d Downstream of Inlet	$\frac{2.5-13.6d}{N.M.}$	36.9	1.0-1.5%	1.3-1.6%	$\frac{.15}{.11}$	0.75	.17	0.5

[1]Symbol "d" refers to the outer diameter of the annulus. All distances are expressed in terms of annulus outer diameter.
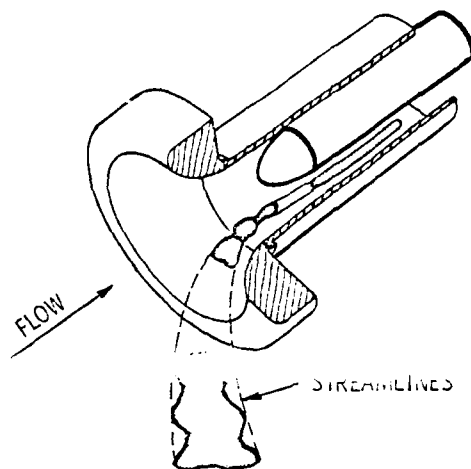
[2]Not Available (N.A.).

[3]Not Measured (N.M.).

Figure 25. Conceptual Illustration of Turbulent Eddy Elongation.

Comparing these data to those of the study conducted by Bekofsky et al.[36] a discrepancy in the relative magnitude of the turbulence intensities emerges. In the two types of inflow turbulence measured by Bekofsky et al.[36], the axial components of turbulence intensity were found to be greater than the tangential components. This result can be explained by considering the generation of the inflow turbulence. Inflow turbulence in the first part of the study was generated by drawing air through the porous ceiling, floor, and walls of the anechoic chamber. Turbulence intensity levels were measured at 1.7 percent and 1.2 percent for the axial and tangential components. The second inflow turbulence investigation closed all air ducts to the walls, ceiling, and floor. Air was admitted only through doors in the wall opposite the fan inlet. The result was an increase in the tangential turbulence intensity from 1.2 percent to 1.6 percent with no increase occurring in the axial intensity. When this is taken into consideration along with the longer axial length scales, it is evident that a larger scale of turbulence is being ingested by the inlet. Thus, a trend is indicated that, with larger room eddies present, a higher tangential intensity is encountered. Based on this idea, a difference in the size of the room turbulence could account for the discrepancy between Bekofsky et al.'s measurements and those of this investigation.

The largest discrepancy between the two components of turbulence intensity is that measured by Shaw, Woodward, Glasner, and Daetoli[37]. In their investigation, the tangential turbulence intensity was ten times larger than the axial intensity. Such a large difference between components could be explained by the subsequent reasoning. First, a large cover for the probe actuator was mounted close (30 cm) to the lip of

the inlet. Disturbances shed from the probe cover could be ingested

into the inlet; and second, the inlet was only two diameters above the

floor and one diameter from the side wall. Work by Hodder[38],

Bekofkse[36], and others have shown that a strong vortex pair forms in-

side the annulus when the inlet is within one to two diameters of the

ground plane. This information, plus the magnitude of the tangential

intensity, strongly suggests the presence of an ingested ground vortex.

Shaw[39] indicated that these areas had not been investigated.

The final class of measurements are those taken in the annular

region between the centerbody and wall. In this class, measurements from

the present investigation are compared to data from studies by Hanson[40],

Robbins[?], and Moiseev [?]. ~~~~~~~ 18 and 19.

data from the present investigation indicated that the tangential compo-

nent of turbulence intensity was found to be 14 percent larger than the

axial component. The 10 percent decrease in both components occurs as

a result of contraction. Finally, the contraction results in a 25 per-

cent increase in axial length scale.

One of the earliest investigations of turbulence in the annulus

region was conducted by Hanson[40]. Hanson measured the axial and tan-

gential intensities to be 0.9 percent and 2.5 percent of the mean flow,

respectively. The axial length scale of this turbulence was found to be

500 cm long. Such a high tangential intensity and a long length scale

can be attributed to the ingestion of atmospheric turbulence. The

upper limit of the characteristic size of a turbulent eddy in Hanson's

investigation is on the order of the thickness of the planetary boundary

layer. Therefore, no quantitative comparison can be made with the pre-

sent results.

Robbins[3] investigated turbulence in the annulus region 17.78 cm
downstream of the inlet. In this region, the tangential intensity was
found to be 30 percent higher than the axial intensity. This trend was
also measured in the present investigation, but at lower levels of in-
tensity. The higher turbulence levels measured in Reference[3] are the
result of the higher flow coefficient at which the rotor was operated.
The flow coefficient used in Reference[3] was double the flow coefficient
used in the present investigation. Finally, since the anechoic enclosure
used by Robbins is similar in size to this investigation's anechoic
chamber, the room turbulence was believed to be the same.

The final study shown in Table 7 is that by Moiseev et al.[4].
Moiseev studied the effect of boundary layer turbulence on the spectrum
of rotor noise. Data on turbulence levels indicated that the axial in-
tensity was 2.5 percent of the mean flow, and the tangential intensity
was 0.5 percent of the mean flow at the center of the annulus. This in-
crease in the axial intensity can be accounted for by the development
of boundary layers on the annulus walls. A comparison of Moiseev et al.'s
measured axial length scale of turbulence to the axial length scales
shown in Table 6 indicates that the presence of boundary layers also
reduces the size of ingested turbulent eddies. Lastly, Moiseev et al.'s
explanation that the shorter length scales they measured were the result
of eddies generated in the boundary layer is verified by the data in
Table 6. Since only one length scale was found at each radius of each
upstream station, it can be concluded that the smaller eddies are not
part of the inflow turbulence. Therefore, it follows that the only
source of these short eddies can be the boundary layer.

4.2 Strut-Generated Disturbances

In this section, the results of the strut wake dominated flow are presented. The various test configurations and aero-acoustic data have been summarized in Table 4. The measured mean velocity profiles, axial length scales, turbulence intensities, and noise spectra are discussed in detail in the following.

4.2.1 Aerodynamic measurements of the strut wake structure

4.2.1.1 Mean velocity profiles. Results of the wake measurements are shown in Figures 26 through 30. The velocity component U_{rx} was nondimensionalized by the free stream velocity and plotted as a function of the normalized tangential probe location Y. The tangential probe location Y was defined by the following equation:

$$Y = \frac{r\vartheta}{S} .$$
(4.3)

In the above equation, r is the radial location of the probe, ϑ is the tangential probe location (in radians), and S is the local rotor blade spacing. By normalizing the tangential probe location in this manner, the difference in two values of Y can be related to the local rotor blade spacing.

Figure 26 illustrates the decay of the strut wake at a radius of $r/r_t = 0.75$. The symmetry of the wake was expected since the strut profile (NACA 0021) was symmetric and at zero incidence to the flow. The velocity defect Λ, defined by Equation (4.4) below, was observed to decrease from a value of 0.32 at Z = 0.18 to a value of 0.06 at Z = 1.82.
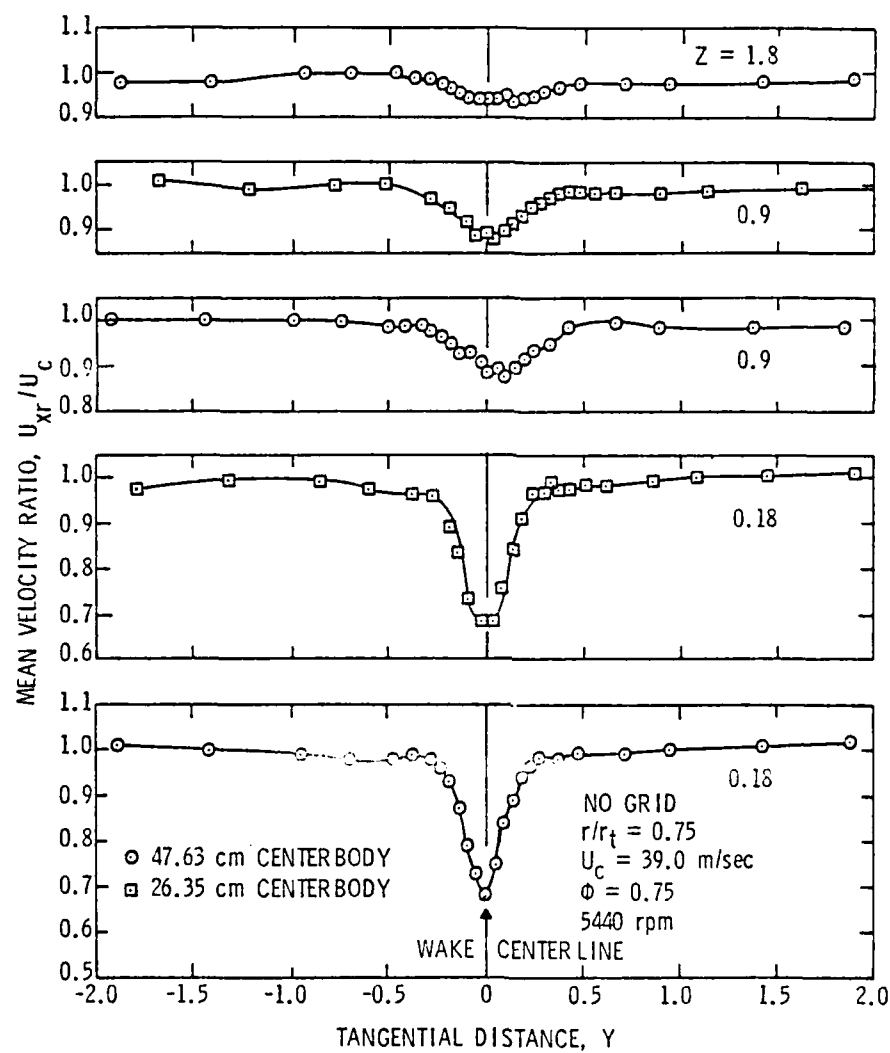
$$\Lambda = 1 - \frac{U_m}{U_c} .$$
(4.4)

Figure 26.   Mean Velocity Profiles at r/r_t = 0.75 as a Function
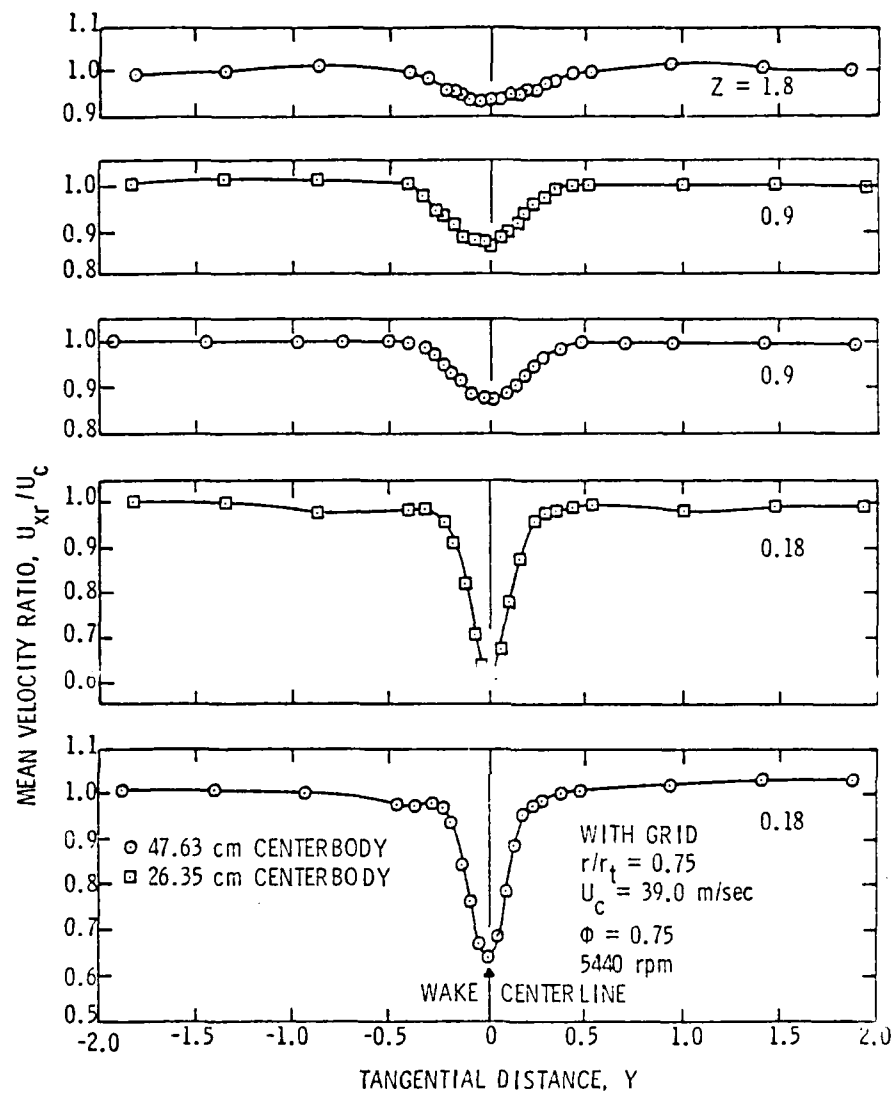of Rotor/Strut Spacing (Z), No Grid Installed.

Figure 27. Mean Velocity Profiles at $r/r_t = 0.75$ as a Function of Rotor/Strut Spacing (Z), Grid Installed.
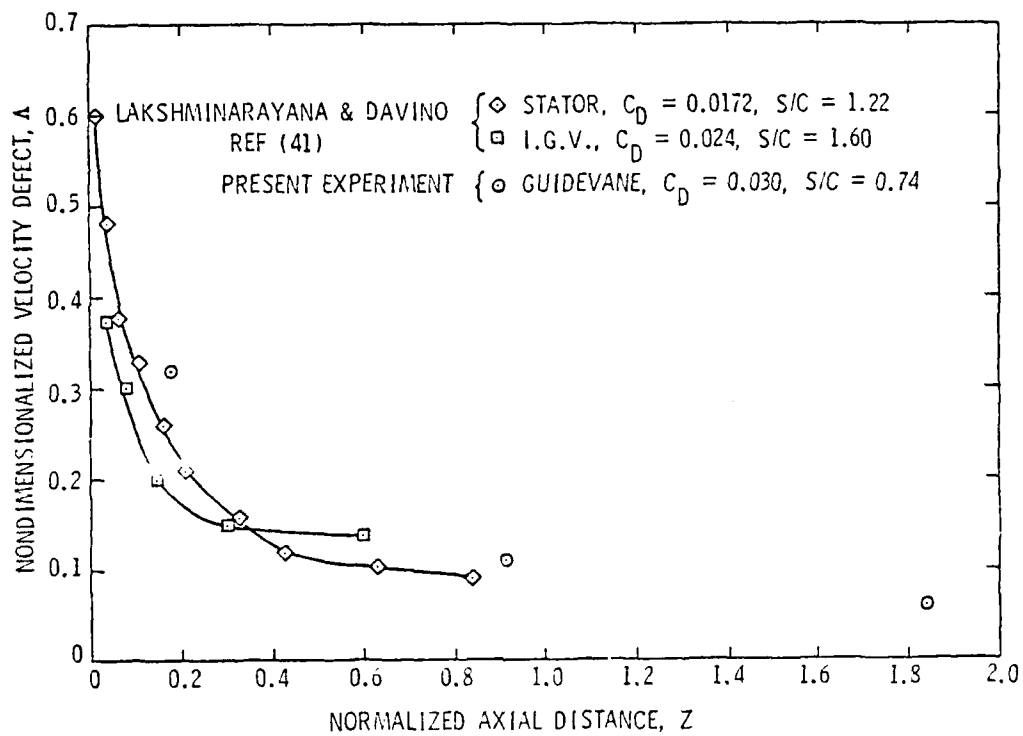
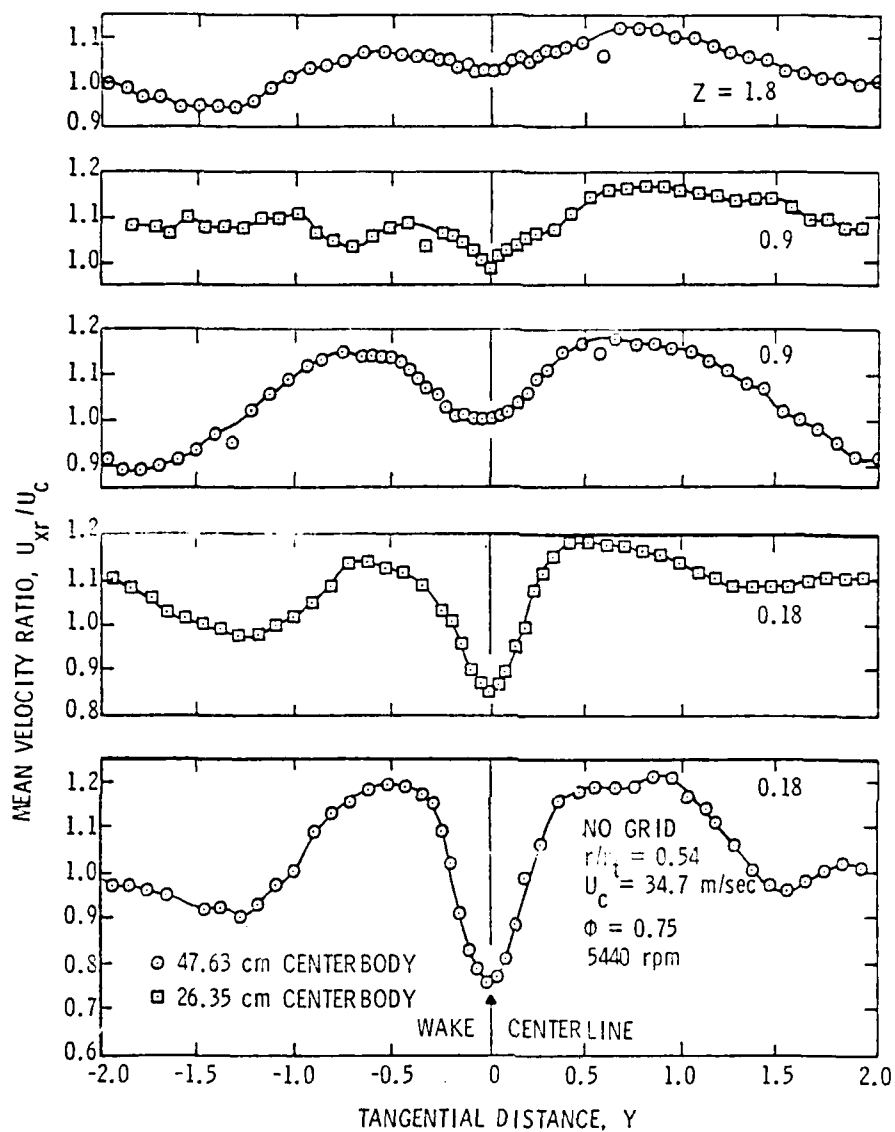Figure 28. Decay of Wake Velocity Defect with Downstream Distance.

Figure 29. Mean Velocity Profiles at $r/r_t = 0.54$ as a Function of Rotor/Strut Spacing (Z), No Grid Installed.
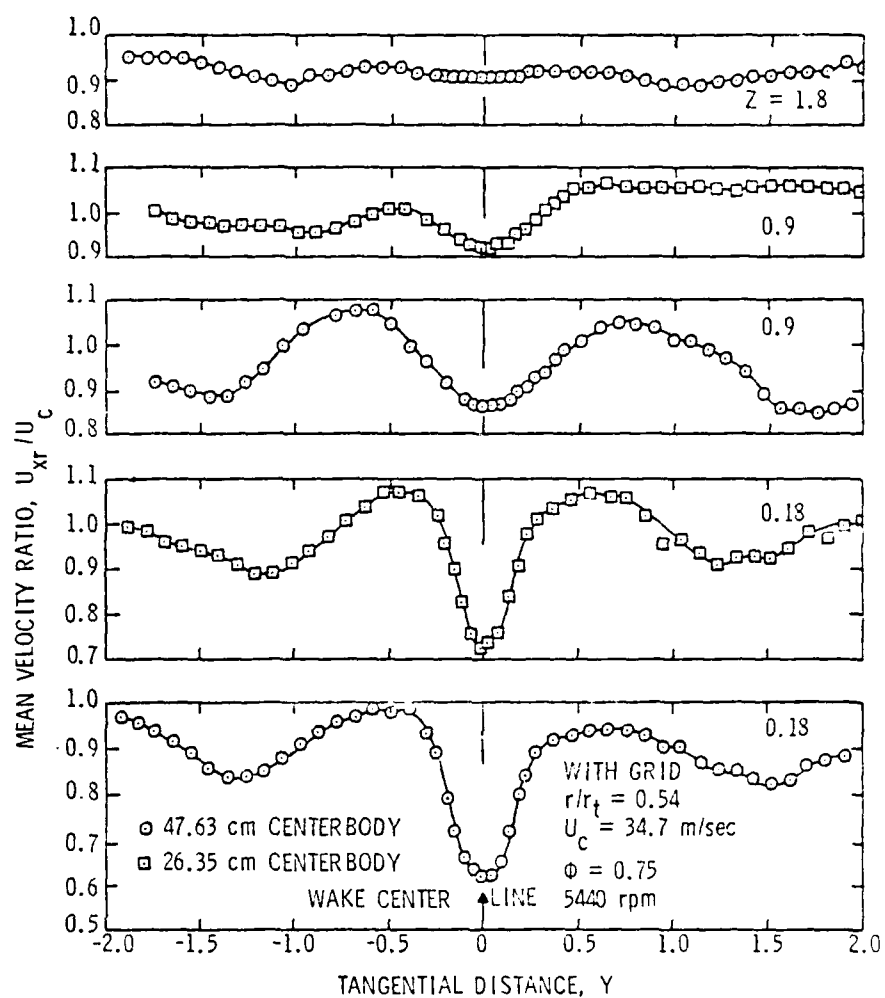
Figure 30.   Mean Velocity Profiles at r/r_t = 0.54 as a Function
of Rotor/Strut Spacing (Z), Grid Installed.

Concurrent with the decay of the velocity defect, the wake width (L_w) was seen to increase from a value of L_w = 0.24 at Z = 0.18 to L_w = 0.57 at Z = 1.82. Figure 27 illustrates that the wake velocity profiles were not significantly altered when the grid was installed. The velocity defect and wake width were similar for both the grid and no grid cases. At this radius, the length of the centerbody did not affect the wake profiles.

Measurements from the present investigation of the velocity defect were plotted against data from the study by Lakshminarayana and Davino[41] in Figure 28. A comparison indicates that the trend shown by the data of Lakshminarayana and Davino was closely matched by that of the present investigation. The higher velocity defect close to the trailing edge of the strut was the result of the low strut solidity.

The wake profiles at a radius of r/r_t = 0.54, which is very near the centerbody wall, are shown in Figures 29 and 30 for the grid and no grid cases. Again, the profiles are symmetric except for the rotor/ strut spacings Z = 0.91 on the 26.35 cm centerbody and Z = 1.82 on the 47.63 cm centerbody. For both of these configurations, the boundary layer at the strut leading edge is on the order of 0.3 cm thick. As reported by Barber[42], the thin boundary layer permits low momentum flow to collect at the trailing edge of the root section of the strut. Since this fluid cannot overcome the adverse pressure gradient developing on the strut surface, flow separation is likely to occur.

The velocity defect and wake width were calculated for these profiles and presented in Table 4. The velocity defect of the wake was measured to be 20 percent higher than those at the strut midspan. This increase was attributed to the contribution to the total velocity vector

by the radial component of velocity. The radial or spanwise velocity generated by vortex flow was responsible for the higher velocities near the wake edge. Again, use of the grid altered the wake decay characteristics only slightly, as shown in Figure 30.

Unlike the velocity profiles at the strut midspan, the length of the centerbody significantly alters the velocity profiles at $r/r_t = 0.54$. As stated earlier, the size of the boundary layer is one of the major factors that controls the vortex flow strength. Thus, shortening the centerbody results in a thinner boundary layer and a weaker vortex flow. This was seen in Figure 29 between the two centerbodies for the case of $Z = 0.18$ and 0.91 as a decrease in the velocity gradient between probe locations $Y = \pm 1.0$ and ± 0.5. This trend was also exhibited for the case of the grid being installed with the exception of the axial spacing $Z = 0.18$.

Based on the velocity gradients in Figures 28 and 29, a calculation was made of the approximate strength of the vortex. The local vortex strength (ξ) is defined by Equation (4.5):

$$\xi = \frac{1}{r}\frac{\partial U_r}{\partial \theta} - \frac{\partial U_\theta}{\partial r} \; .$$

(4.5)

The velocity component measured by the probe is defined by the following equation

$$U_{rx}^2 = U_r^2 + U_x^2 \; .$$

(4.6)

By taking the derivative with respect to θ of both sides of Equation (4.6) and rearranging terms, Equation (4.7) was obtained:

$$\frac{\partial U_r}{\partial \theta} = \frac{1}{U_r} \left\{ U_{rx} \frac{\partial U_{rx}}{\partial \theta} - U_x \frac{\partial U_x}{\partial \theta} \right\} . \tag{4.7}$$

Substitution of Equation (4.7) into Equation (4.5) yields the following equation.

$$\xi = \frac{1}{U_r} \left\{ U_{rx} \frac{\partial U_{rx}}{\partial \theta} - U_x \frac{\partial U_x}{\partial \theta} \right\} - \frac{\partial U_\theta}{\partial r} . \tag{4.8}$$

If Equation (4.8) is evaluated along a line through the vortex core, the last term is small and can be neglected. Of the two remaining terms, it was assumed that the first term was stronger than the second inside the vortex flow region. The̲re̲fo̲re̲ ̲th̲e̲ ̲st̲re̲ng̲th̲ ̲wa̲s ̲es̲ti̲ma̲te̲d by Equation (4.9):

$$\xi_1 = \frac{1}{U_r} U_{rx} \left(\frac{\partial U_{rx}}{\partial \theta} \right) . \tag{4.9}$$

The calculated vortex strengths are compared in Figure 31 to the vortex strength predicted using a theory due to Hawthorne[43]. The strength of the vortex was normalized with respect to the strongest vortex case (47.63 cm centerbody, Z = 0.18). The boundary layer thicknesses were normalized with respect to the thickest boundary later. As illustrated in Figure 31, the trend exhibited by the calculated vortex strength for each configuration agrees well with theory.

4.2.1.2 Turbulence intensity profiles. The measured turbulence profiles of the strut are shown in Figure 32 for $r/r_t = 0.75$. In Figure 32, the wake centerline turbulence intensity at $Z = 1.82$ was
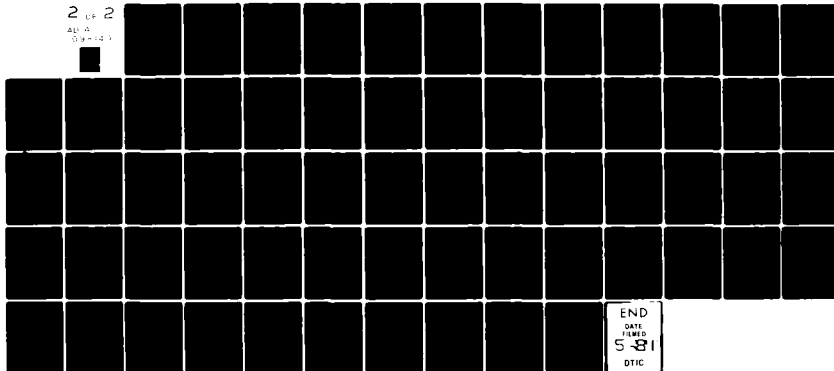
1.0

2.8 2.5

3.2 2.2

3.6

2.0

1.1

1.8

1.25 1.4 1.6
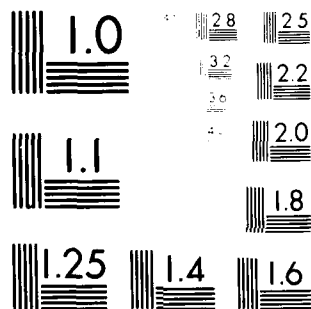
MICROCOPY RESOLUTION TEST CHART

Figure 31. Comparison of Predicted Vortex Strength to Experimentally Calculated Vortex Strength.

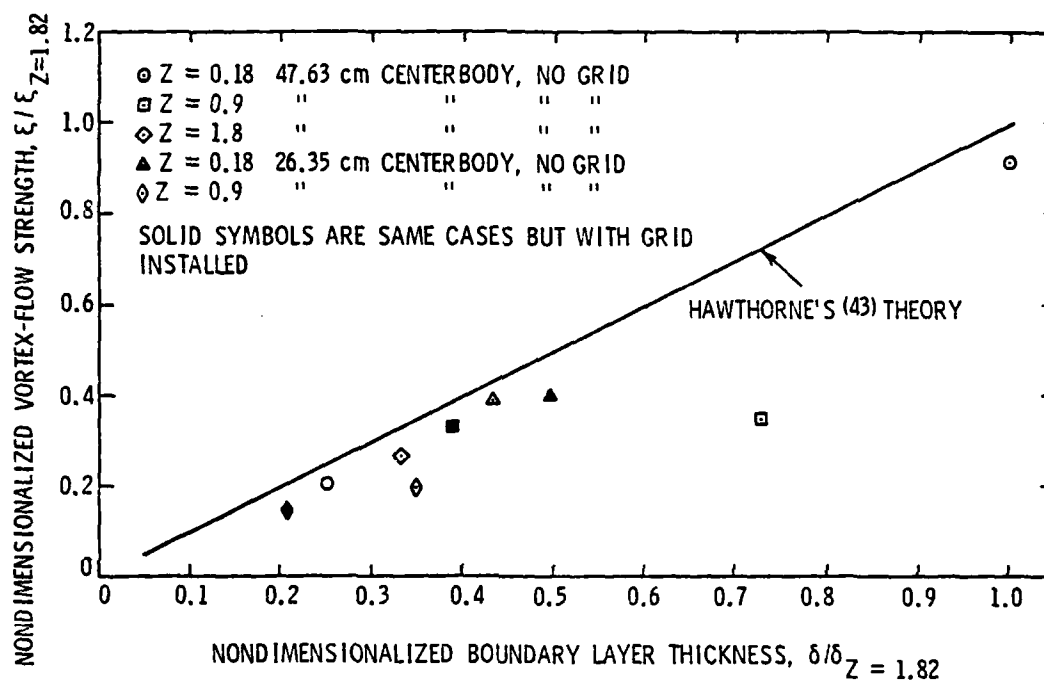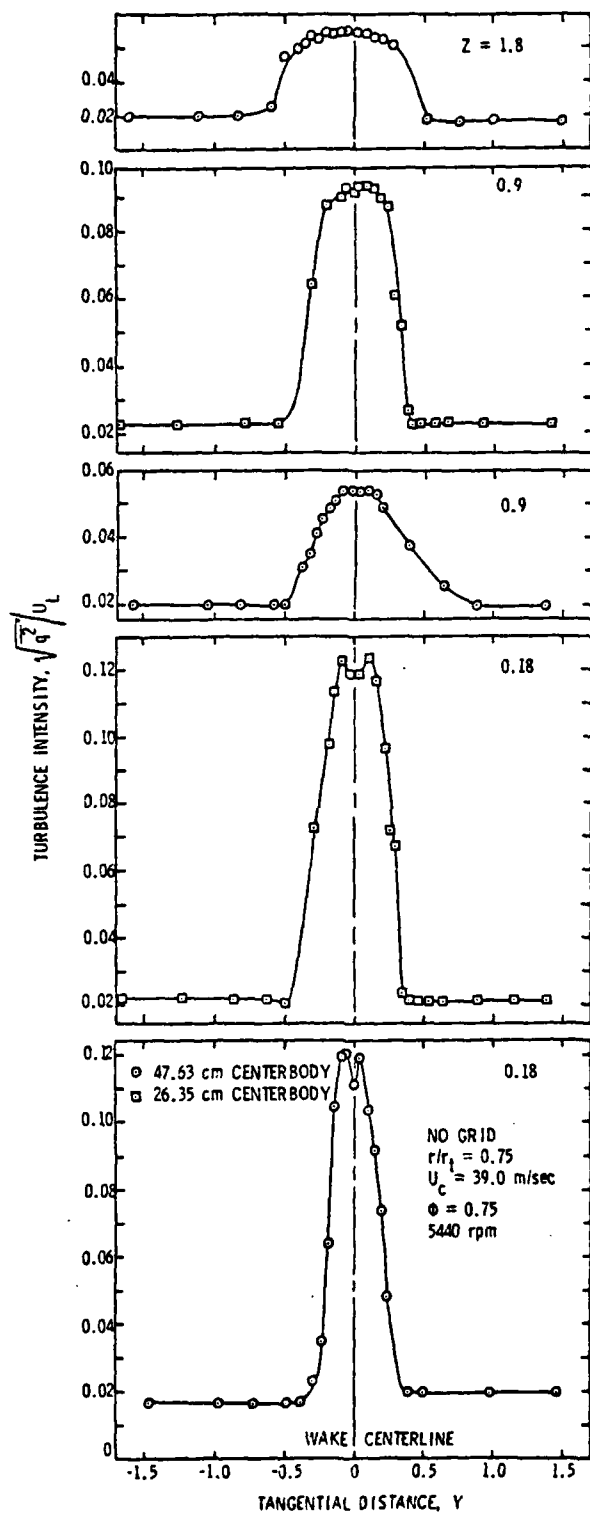Figure 32. Turbulence Intensity Profiles at $r/r_t = 0.75$ as a Function of Rotor/Strut Spacing (Z), No Grid Installed.

approximately 38 percent of the peak intensity at Z = 0.18. This decay
rate, compared to the rate of decay of the velocity defect, indicates
that the wake turbulence decays 20 percent slower than the velocity de-
fect for this configuration. The length of the centerbody did not alter
the turbulence intensities for a rotor/strut spacing of Z = 0.18. The
lower turbulence levels measured on the long centerbody for Z = 0.91
when compared to the same spacing on the short centerbody are the result
of the strong vortex present on the long centerbody. The effect of grid
generated turbulence on the wake turbulence profiles is shown in Fig-
ure 33. Installation of the grid increased the free stream turbulence
intensities from 2 percent to 5 percent. A 14 percent increase in the
intensity levels at the wake centerline was also measured. A comparison
of the turbulence levels at the wake centerline for the Z = 0.18 and
0.91 spacings on the 26.35 cm centerbody indicates that the higher free
stream turbulence results in a faster decay of wake generated turbulence.

Illustrated in Figure 34 are the strut turbulence profiles at a
radius of r/r_t = 0.54 with no grid installed. The appearance of the
peaks on either side of the strut wake peak were the result of strut
generated vortices. The turbulence intensity of these vortices was mea-
sured to be 12 percent of the local free stream flow velocity for
Z = 0.18 for both centerbodies. The measured turbulence intensity at
the wake centerline was slightly higher at 13 percent. Movement down-
stream to Z = 0.91 resulted in a 25 percent decay of the wake. The
effect of installing the grid on the turbulence profiles is shown in
Figure 35. With the grid installed, the turbulence intensity increased
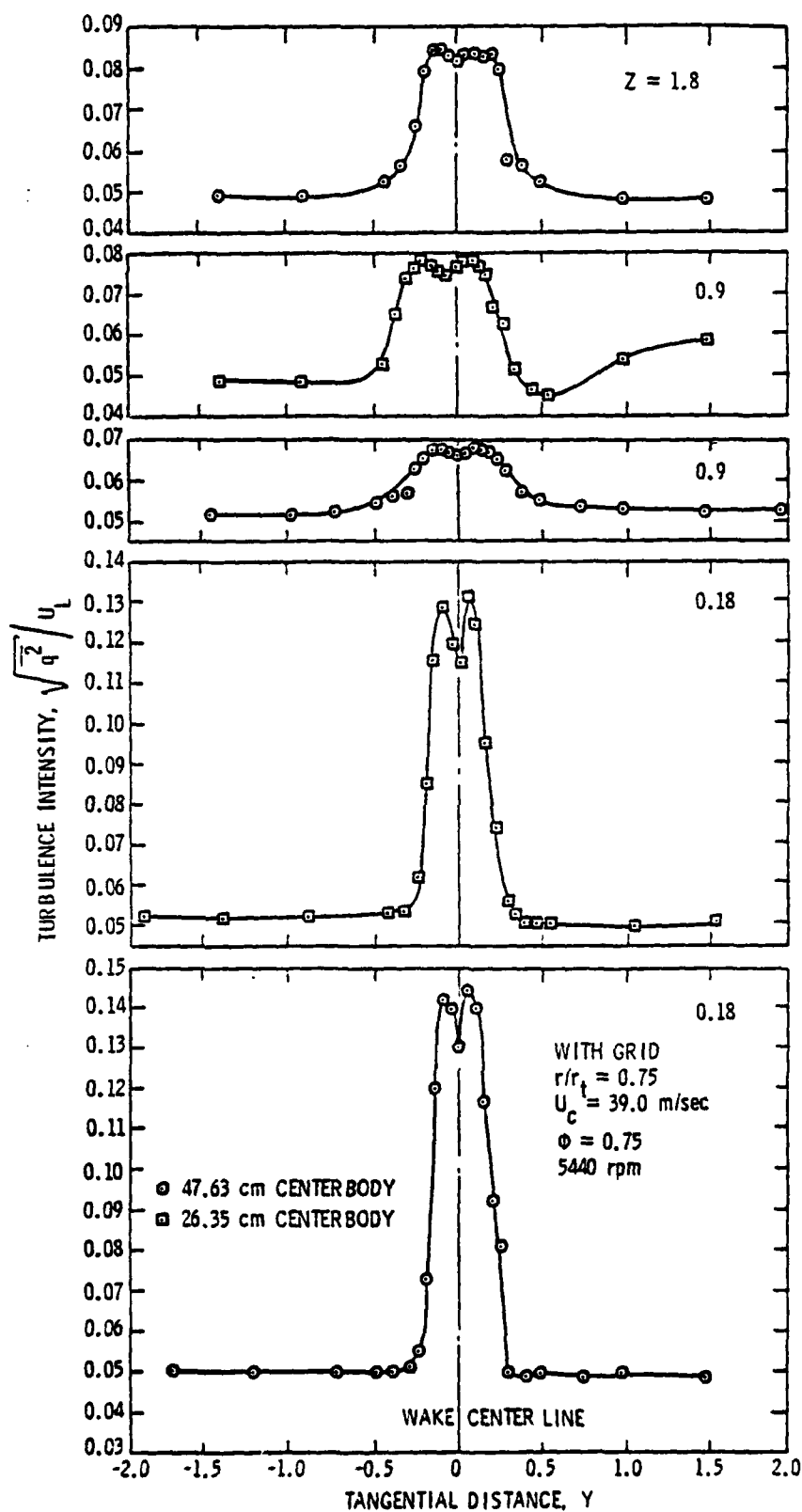by 9 percent. The wake centerline turbulence levels decayed twice as

Figure 33. Turbulence Intensity Profiles at $r/r_t = 0.75$ as a Function of Rotor/Strut Spacing (Z), Grid Installed
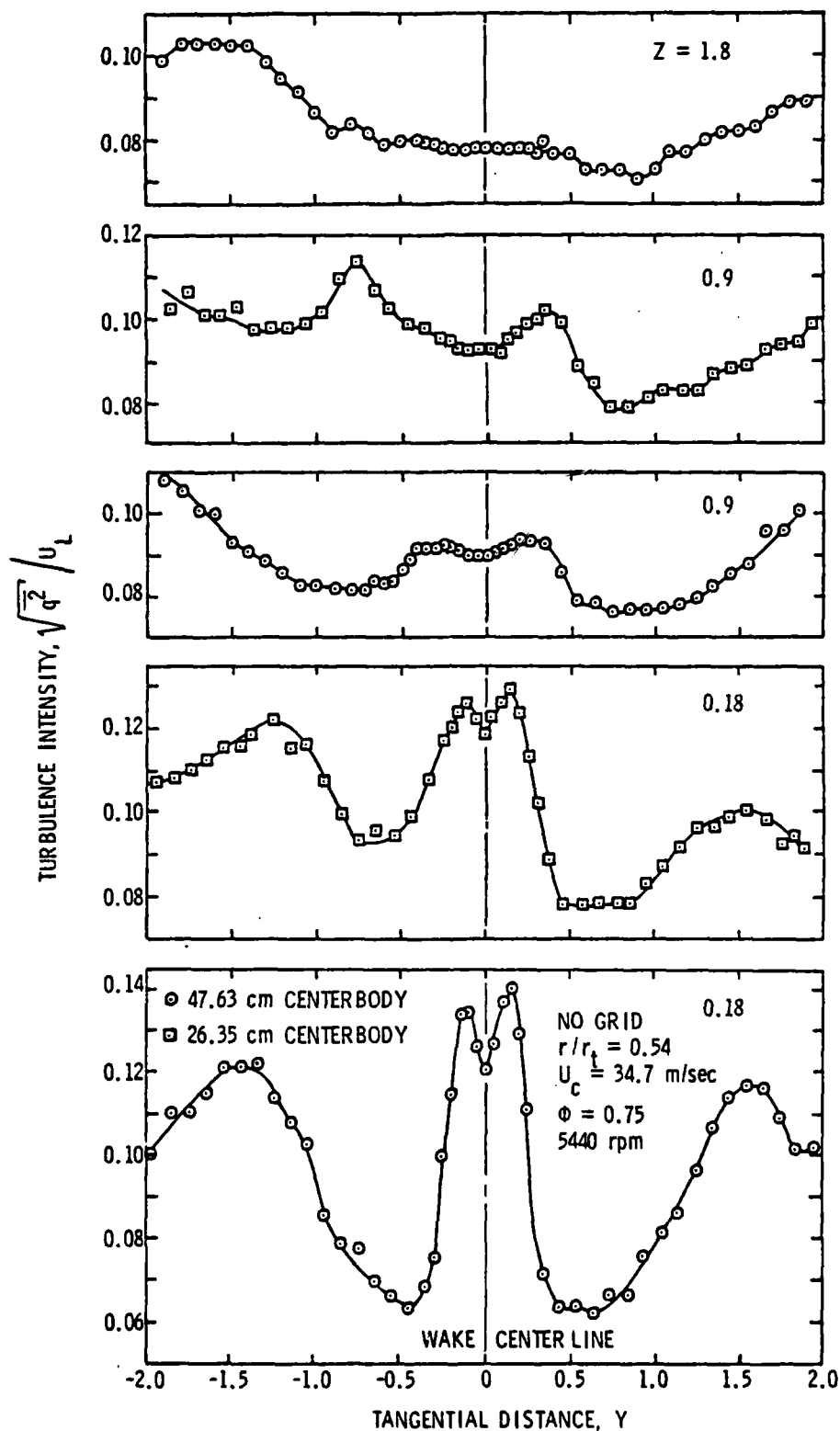
Figure 34.   Turbulence Intensity Profiles at r/r_t = 0.54 as a Function of Rotor/Strut Spacing (Z), No Grid Installed.
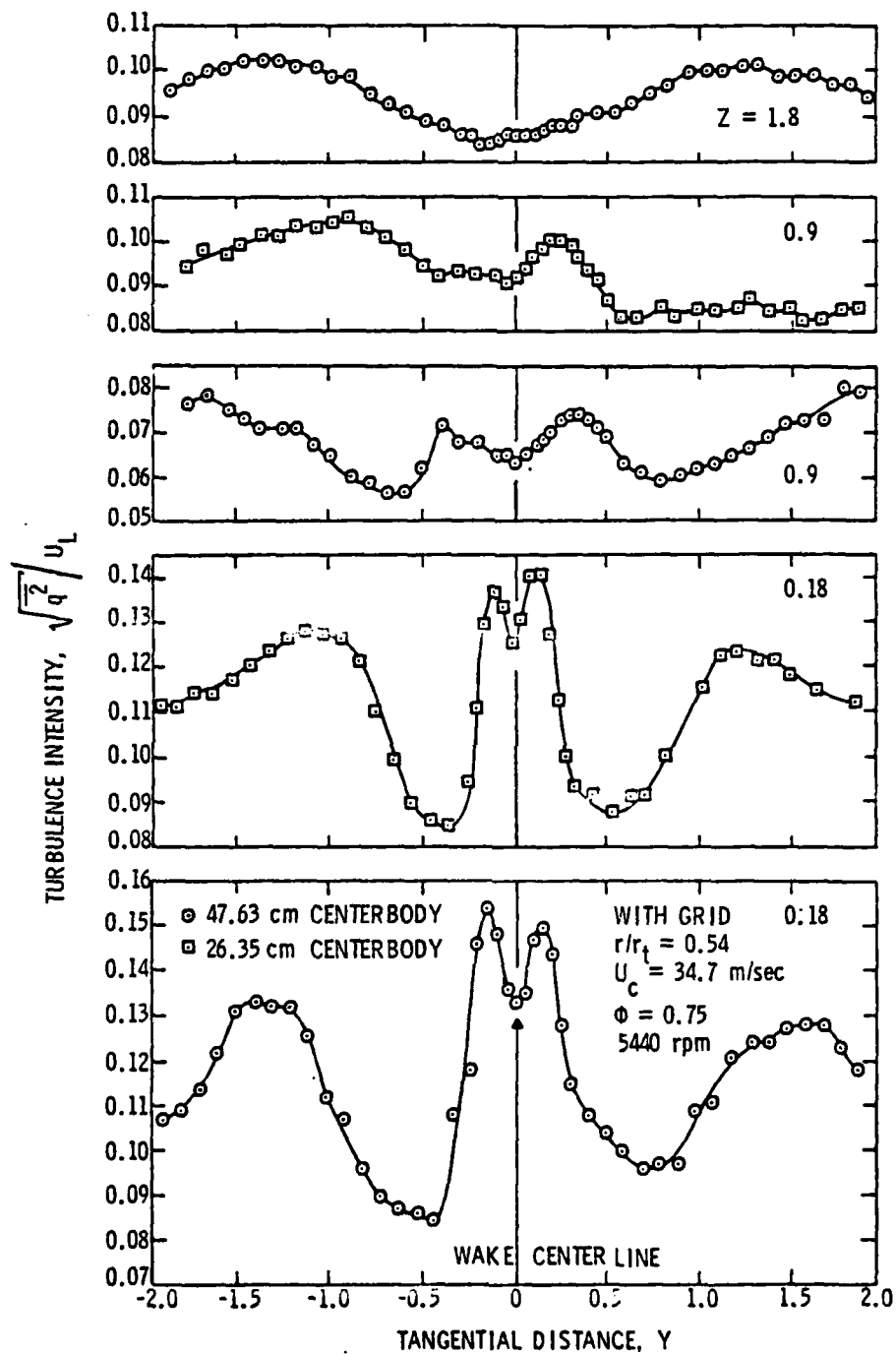
Figure 35. Turbulence Intensity Profiles at $r/r_t = 0.54$ as a Function of Rotor/Strut Spacing (Z), Grid Installed.

fast as those values for the no grid case. This decay rate also applied to the intensities in the vortex region.

Comparing Figure 34 with the mean velocity profiles in Figure 29, it is clear that the core of the vortex region is located near Y = ±1.5, where the velocity was minimum and the turbulence intensity was maximum. The edge of the vortex was located at approximately Y = ±0.5, where the velocity was maximum and the turbulence intensity was minimum.

The wake and vortex regions coexist in the centerbody wall region, thus resulting in a complex flow field (both random and periodic) into the rotor. This complex flow field should contribute not only to the pure tone noise, but also to the broadband noise of the rotor.

4.2.1.3 Axial length scales. The axial length scales of turbulence were measured at the wake center and in the free stream. Typical autocorrelation curves at these positions are shown in Figures 36 through 39 for the various configurations. Analyses of the data summarized in Table 4 indicate the presence of two axial length scales in the strut wake. The first was due to room turbulence present in the anechoic chamber. The presence of the four struts increased the length scale of the eddies due to the room turbulence by 38 percent when compared to the no-strut case (natual boundary layer). The wakes of the struts stretched these eddies as additional 13 percent. Installation of the grid effectively reduced the size of these room eddies.

The second length scale present in the strut wake was that of the boundary layer turbulence shed from the strut. The length scale of these eddies was on the order of 15 cm. Measurements in the strut boundary layer, 0.64 cm upstream of the trailing edge, verified the presence

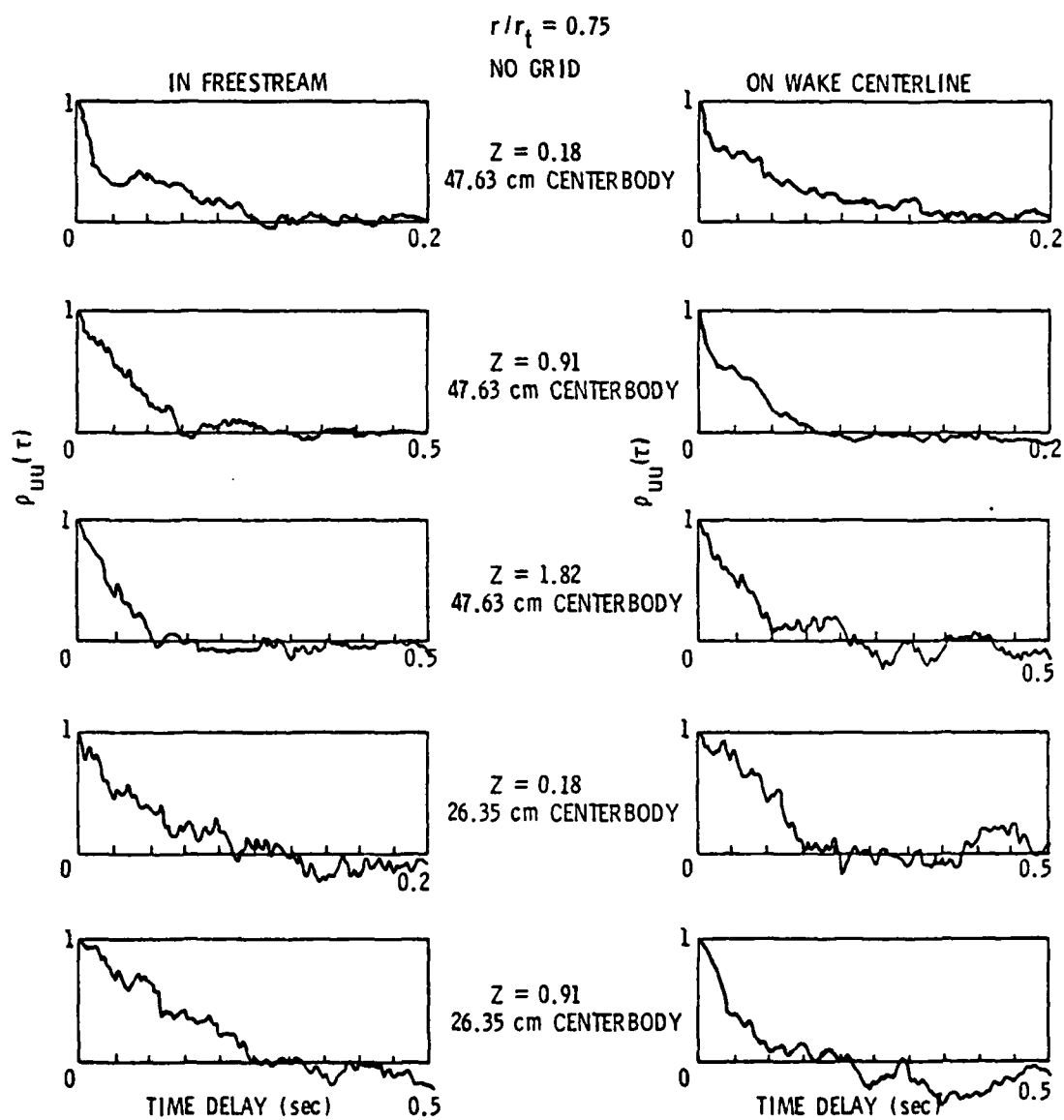Figure 36. Auto-Correlation Curves for Strut Wake Measurements at
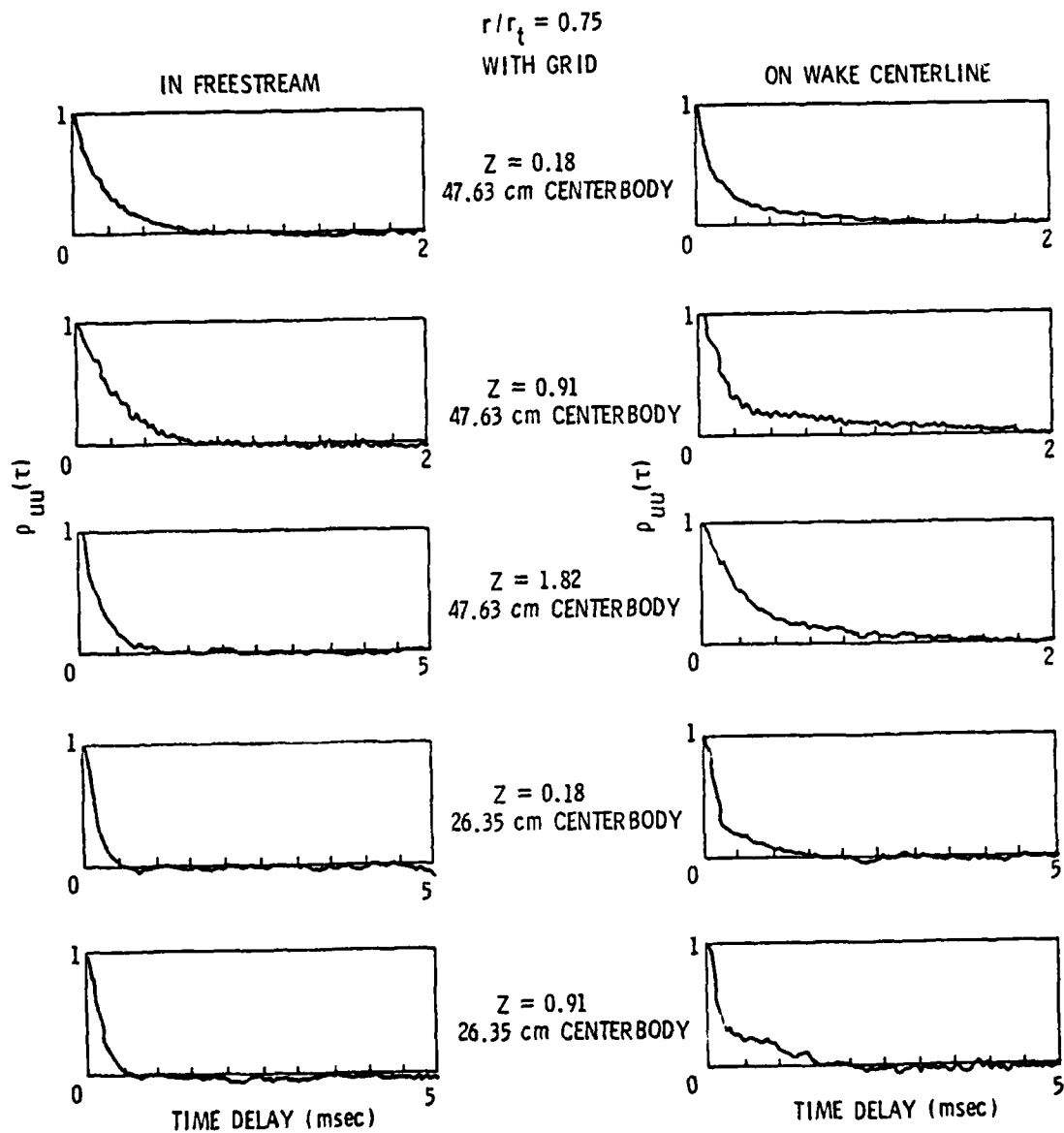$r/r_t = 0.75$, No Grid Installed.

Figure 37. Auto-Correlation Curves for Strut Wake Measurements at $r/r_t = 0.75$, Grid Installed.
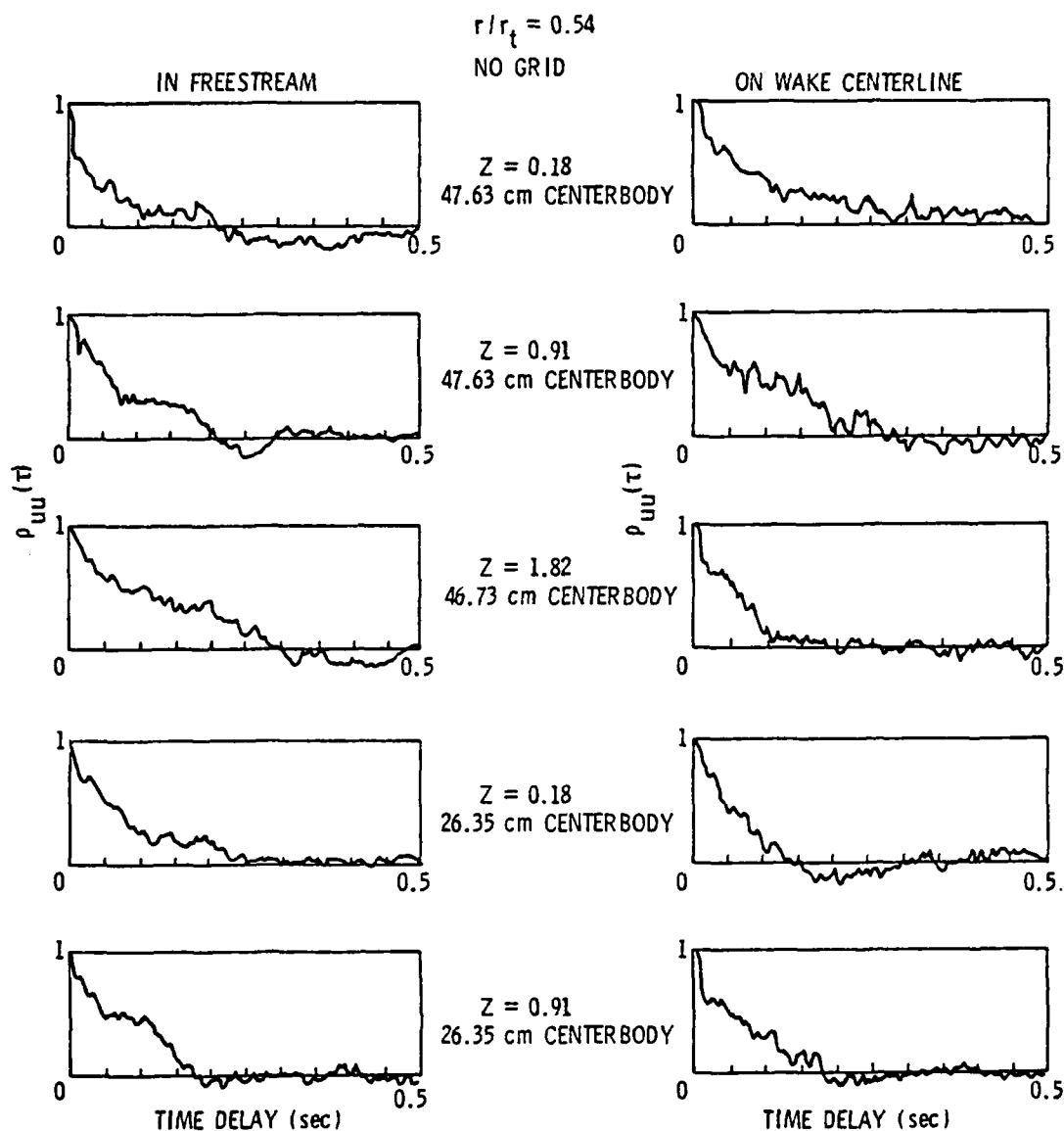
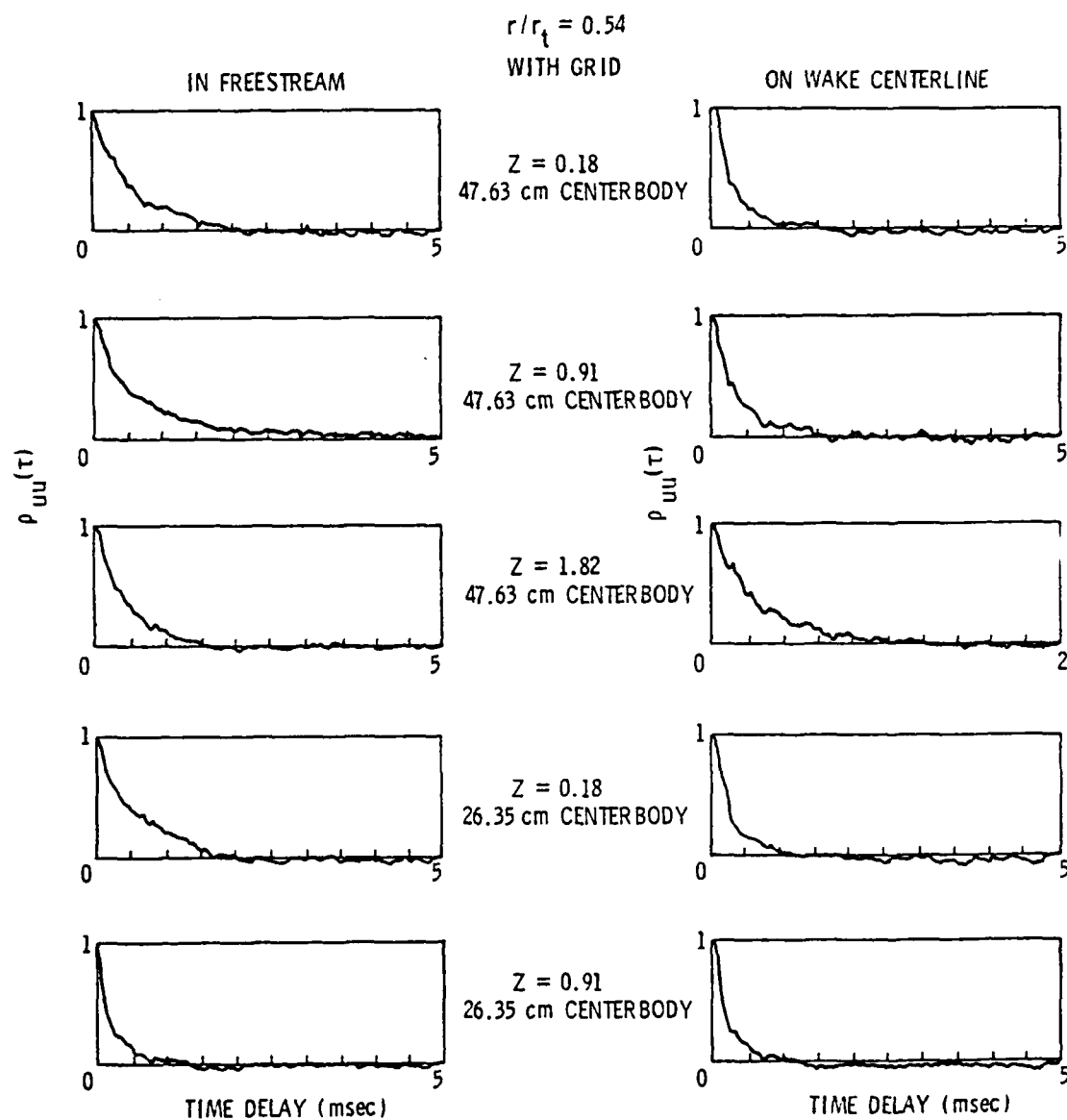Figure 38. Auto-Correlation Curves for Strut Wake Measurements at $r/r_t = 0.54$, No Grid Installed.

Figure 39. Auto-Correlation Curves for Strut Wake Measurements at
r/r$_t$ = 0.54, Grid Installed.

of the short length scale along with length scales of 15.0 cm due to
room turbulence. The axial length scale of the room turbulence entering
the strut boundary layer apparently was not significantly altered as it
moved downstream.

The axial length scales measured in the centerbody boundary layer
were generally longer than the length scales at mid span, but no clear
difference appeared between the length scales of the free stream region
and wake center. This was to be expected, since strong vortices were
present in this region. Again, the grid greatly reduced the axial length
scale of the turbulence.

4.2.2 _Acoustic data and interpretation_. The spectrum of background
noise was measured with the rotor removed and the auxiliary fan running
at its test speed. The background noise level was found to be 10 dB
below the rotor noise spectrum and, therefore, the signal-to-noise ratio
was considered acceptable. The directivity pattern at blade passing
frequency for the 17-bladed rotor was also measured with the microphone
located at a radial position 76.2 cm upstream of the inlet (Figure 4).
The results are shown in Figure 40. Since no lobed pattern was mea-
sured, the sound pressure levels (SPL) measured along the annulus center-
line were considered representative for all angles.

4.2.2.1 _Sound spectra data_. Sound spectra measured for the
47.63 cm centerbody with and without a grid are shown in Figures 41 and
42. With no struts present, the first, second, and third harmonics of
blade passing frequency (BPF = 1541 Hz) were measured at levels of 92 dB,
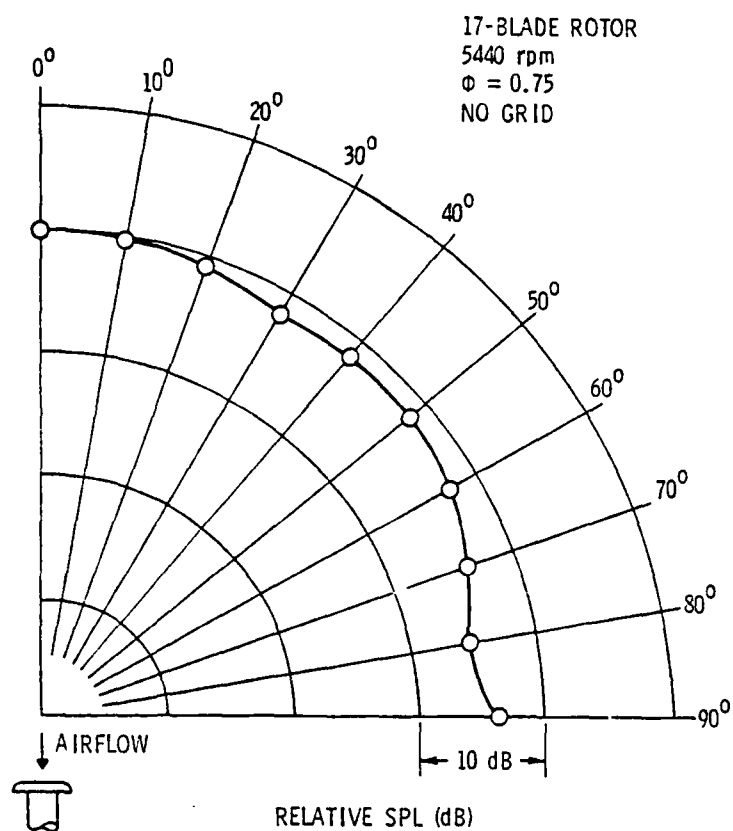78 dB, and 74 dB, respectively. Installation of the four struts at the

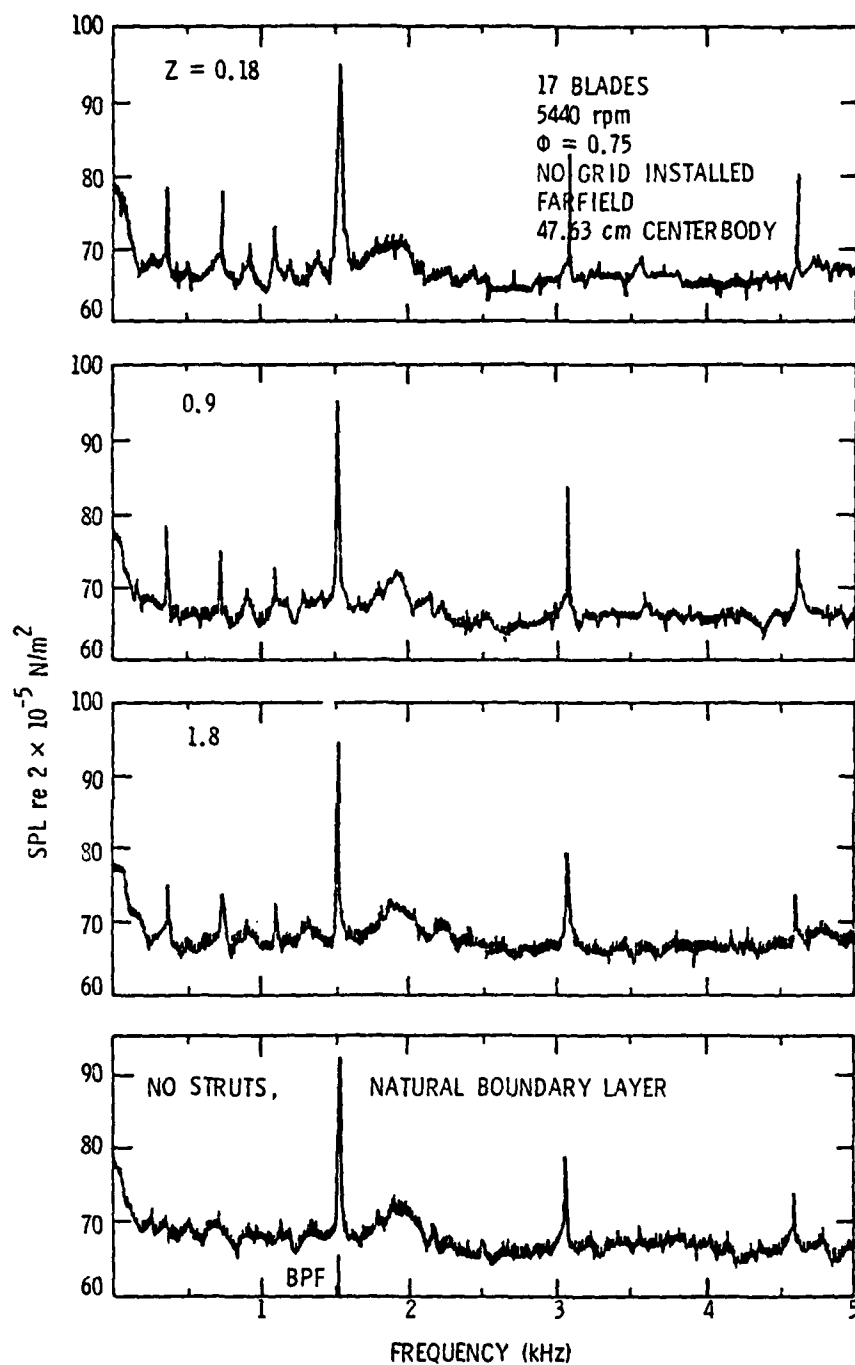Figure 40.   Directivity Pattern for 17-Bladed Rotor, No Grid Installed.

Figure 41. Sound Spectra for 47.63 cm Centerbody, No Grid Installed.

greatest axial spacing of Z = 1.82 resulted in a slight (2 dB) increase in the first harmonic with no increase being measured for the second and third harmonics. The addition of the struts also produced peaks at the first three harmonics of the strut passing frequency (SPF = 363 Hz). The SPL of these peaks was 74 dB. Movement of the struts to the position Z = 0.91 resulted in no noticeable change in the first and third harmonics of BPF. Decreasing the rotor-to-strut spacing resulted in a 4 dB increase in the second BPF and a 3 dB increase in the first harmonic of SPF. At the Z = 0.18 spacing, the first and second harmonics of BPF did not change, but the third harmonic increased by 5 dB. These results seem to indicate that the strut wake has very little effect on the noise generation in this particular case. The dominant noise source is still the inlet turbulence. The second harmonic of SPF shows a 3 dB increase at this spacing, while the first and third harmonics were constant. The broad peak centered at a frequency of 1.8 kHz was the result of a blade vibration.

The effects of the grid on the rotor noise spectra are shown in Figure 42. Two results are immediately apparent: the first was the decrease in number and magnitude of the BPF and SPF harmonics, and the second was the broadening of the peak at the first BPF of 1541 Hz. Beginning with the no strut case, the levels of the first through third harmonics of BPF were 81 dB, 73 dB, and 73 dB, respectively. Thus, the grid reduced the first BPF harmonic by approximately 10 dB and the second harmonic by 5 dB. Addition of the struts at an axial distance of Z = 1.82 resulted in only a 2 dB increase in the first BPF and no increase in the second and third harmonics. No peaks were measured above the broadband level for the strut passing frequencies. This was interpreted
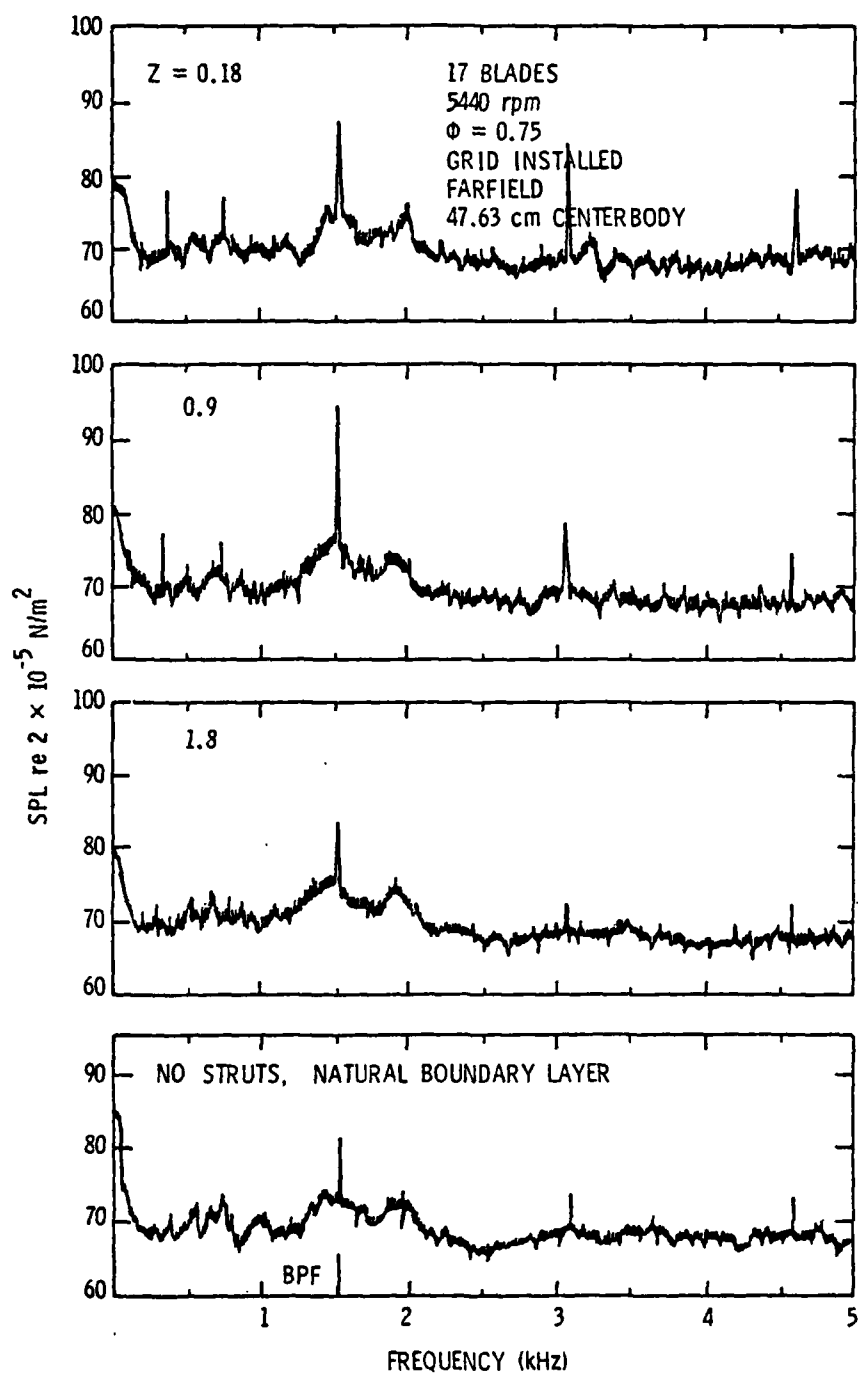
Figure 42.   Sound Spectra for 47.63 cm Centerbody, Grid Installed.

again as a case dominated by inlet turbulence. Movement of the struts
to Z = 0.91 resulted in a dramatic increase in the first harmonic of
BPF to 94 dB. Increases of 5 dB and 2 dB were also measured for the
second and third harmonics of BPF. At this spacing, the first and
second harmonics of SPF had levels of 75 dB. The close spacing of
Z = 0.18 results in a decrease in the level of the first harmonic of
BPF to 83 dB. The SPL of the second and third harmonics increases to
85 dB and 78 dB, respectively. No change was noticed in the first and
third harmonics of SPF. Finally, around the first harmonic of BPF, a
5 dB increase in the broadband signal was measured as a result of the
grid induced turbulence. This turbulence also increased the entire
broadband level by 3 dB.

Effects of the shorter (26.35 cm) centerbody with no grid are shown
in Figure 34. The difference between the long and short centerbodies,
insofar as the flow is concerned, is mainly the alteration of the
strength of the vortex flow. With the exception of the smaller center-
body boundary layer, other parameters such as wake structure and inlet
turbulence should not be changed. With no struts installed, the SPL of
90 dB for the first harmonic and 72 dB for the second and third harmonics
of BPF were recorded. With the struts at Z = 0.91, the first harmonic
increased to 93 dB, and the second harmonic increased to 81 dB. No
change occurred at the third harmonic. The levels of the first, second,
and third harmonics of SPF were 77 dB, 75 dB, and 73 dB, respectively.
Movement of the struts to Z = 0.18 caused no change in the BPF harmonics.
The first and second harmonics of SPF, however, did increase by 2 dB
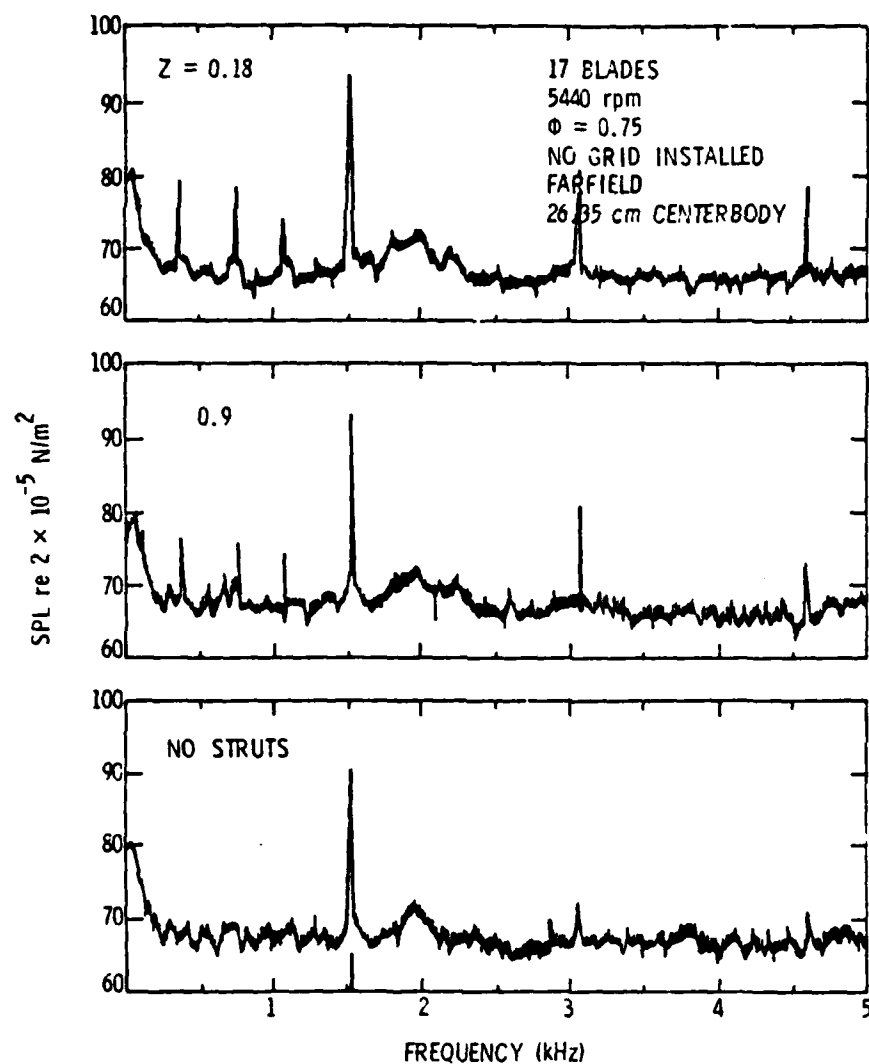each.

Figure 43. Sound Spectra for 26.35 cm Centerbody, No Grid Installed.

The measured spectra with the grid installed are shown in Figure 44. Without struts, the level of the first BPF was 82 dB. The second and third harmonics were 78 dB and 74 dB, respectively. Moving the struts closer resulted in an 8 dB increase in the BPF harmonic. Increases of 3 dB and 9 dB were measured for the second and third BPF harmonics. The first and second SPF harmonics appeared at this spacing with sound pressure levels at 75 dB. The broadband level was measured at 68 dB.

4.2.2.2 <u>Correlation of acoustic data</u>. In the configurations discussed so far, there are three sources of flow disturbances that can generate coherent noise, as follows: long eddies due to the inlet turbulence, turbulence and velocity defects in the strut wake, turbulence and velocity distortions in the vortices at the root of the struts. The purpose of this section is to evaluate the relative importance of these effects based on physical phenomena, flow/noise correlation, and existing theories.

The relative dB levels of the first, second, and third harmonics of BPF are shown in Figures 45a and 45b for the grid and no-grid cases, respectively. In this section, the variation of the SPL of the first harmonic of BPF shown in these figures was correlated with the measured changes in the following parameters: wake velocity profile, wake turbulence, vortex strength, and inlet turbulence. The measured sound pressure levels of the first harmonic of BPF were also compared to the predicted levels obtained by an analytical method due to Homicz[44] and an unsteady thrust analysis due to Thompson[18] to determine which previously mentioned sources make the dominate contribution to rotor noise.
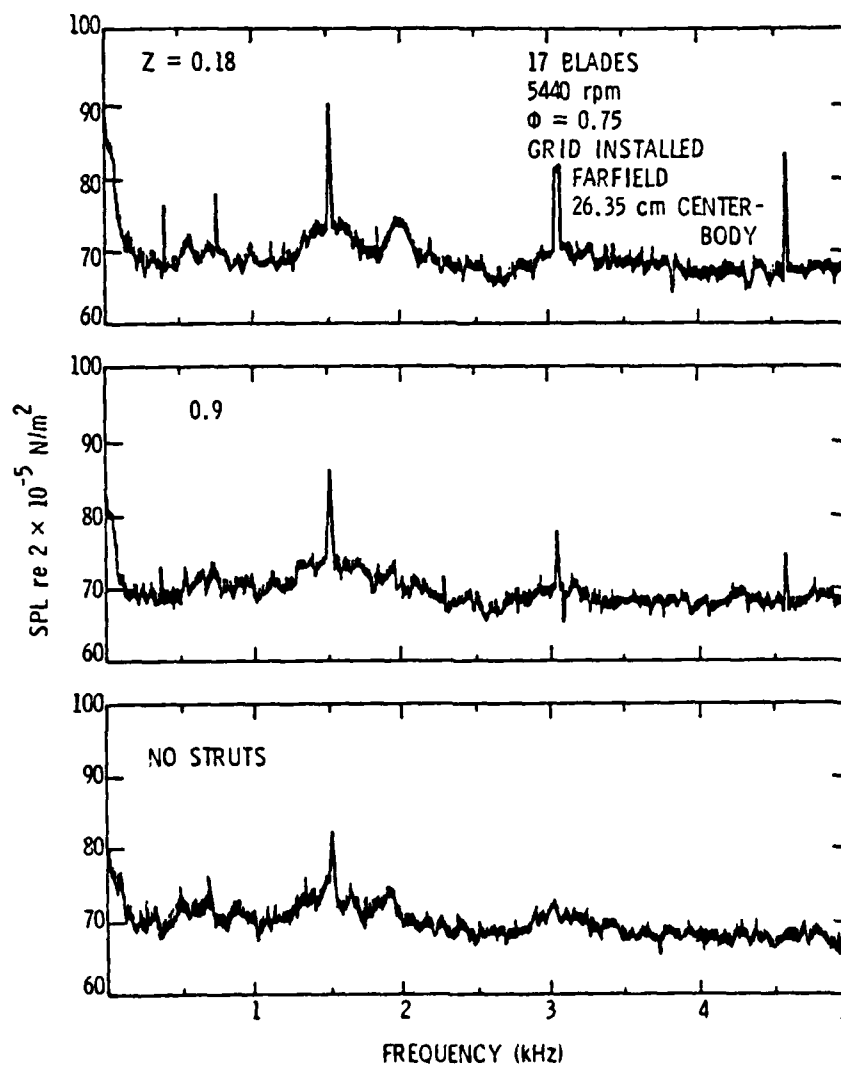
Figure 44. Sound Spectra for 26.35 cm Center body, Grid Installed.
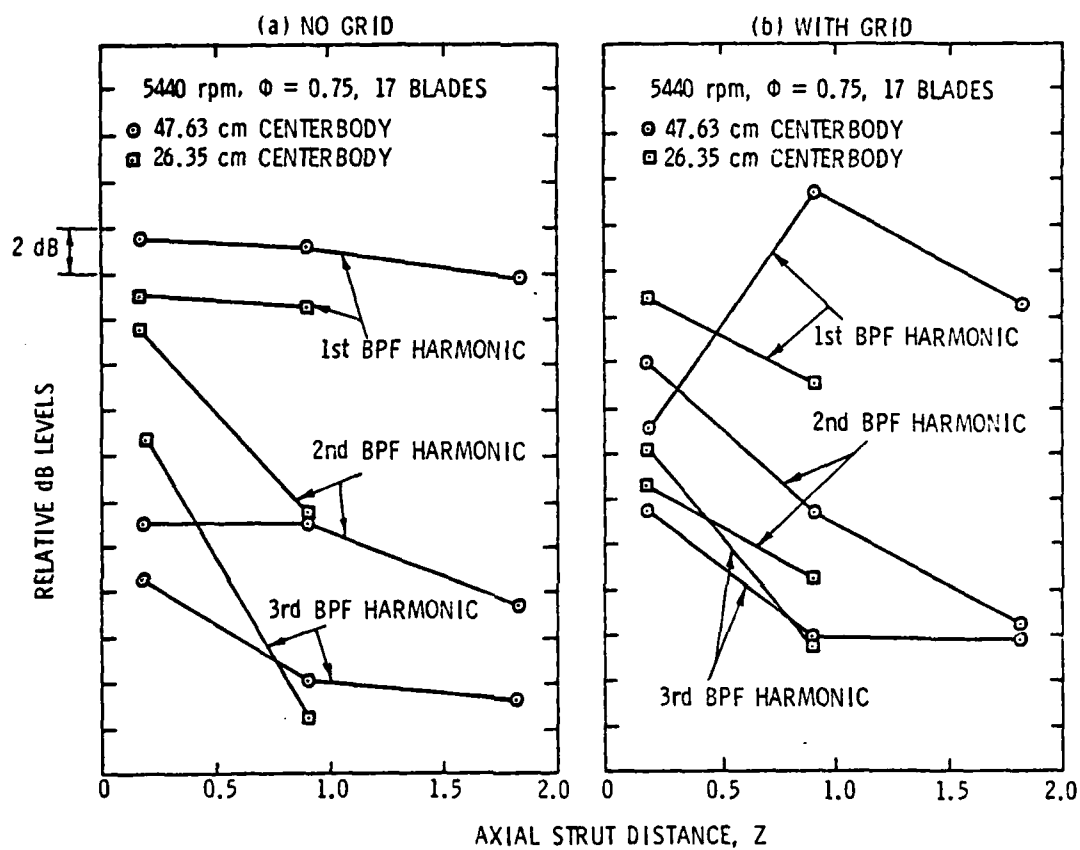
Figure 45. Variation of Blade Passing Frequencies with Strut Spacing, Grid and No Grid Installed.

A comparison of the aforementioned theories with the measured SPL of the first BPF is shown in Figure 46. Homicz's theory, which models the strut wake based on an isolated airfoil wake decay model, predicts that a 20 dB drop should occur with the change in axial separation distance between the strut and the rotor used in this experiment. This drop was not measured in either the grid or the no grid case. Homicz's program was then modified to exclude noise due to potential flow effects and strut noise due to rotor blade passing in an attempt to determine only the noise due to the rotor operating in the strut wakes. Results indicate that, although a lower SPL was obtained, the computed dB change with separation was much higher than measured.

A second attempt to correlate the strut wake with the sound pressure level was conducted by calculating the unsteady thrust of the rotor by using an analysis due to Thompson[18]. The input of this technique required 360-degree wake surveys at three radii: $r/r_t = 0.54$, $r/r_t = 0.75$, and $r/r_t = 0.95$. These data, shown in Figure 47, are similar to those presented in Figures 26 and 27, with the exception of the additional data of the other three strut wakes. Each wake survey was Fourier analyzed to determine the harmonic coefficients. These Fourier coefficients were then used to compute the unsteady rotor thrust[18], and the sound pressure level which is proportional to the square of the unsteady thrust. As shown in Figure 46, the relative change in the sound pressure level due to the unsteady thrust with axial strut spacing indicates a 10 dB drop in SPL. This confirms the earlier conclusion that the velocity defect due to the strut wake was not a major source of rotor noise.

An attempt was made to estimate the trend in the tonal noise generated due to various sources using the experimental flow data. The
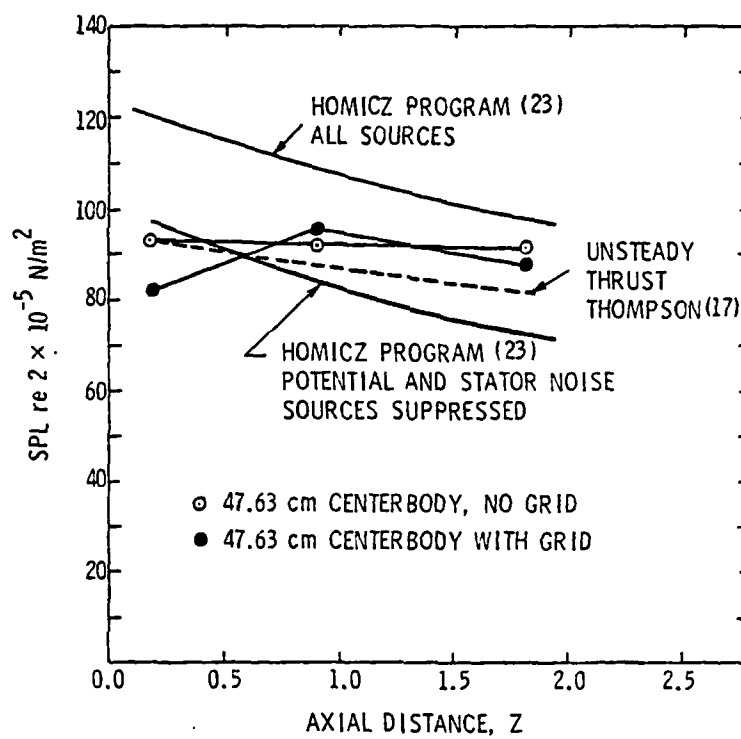
Figure 46. Comparison of Theoretical Noise Predictions to
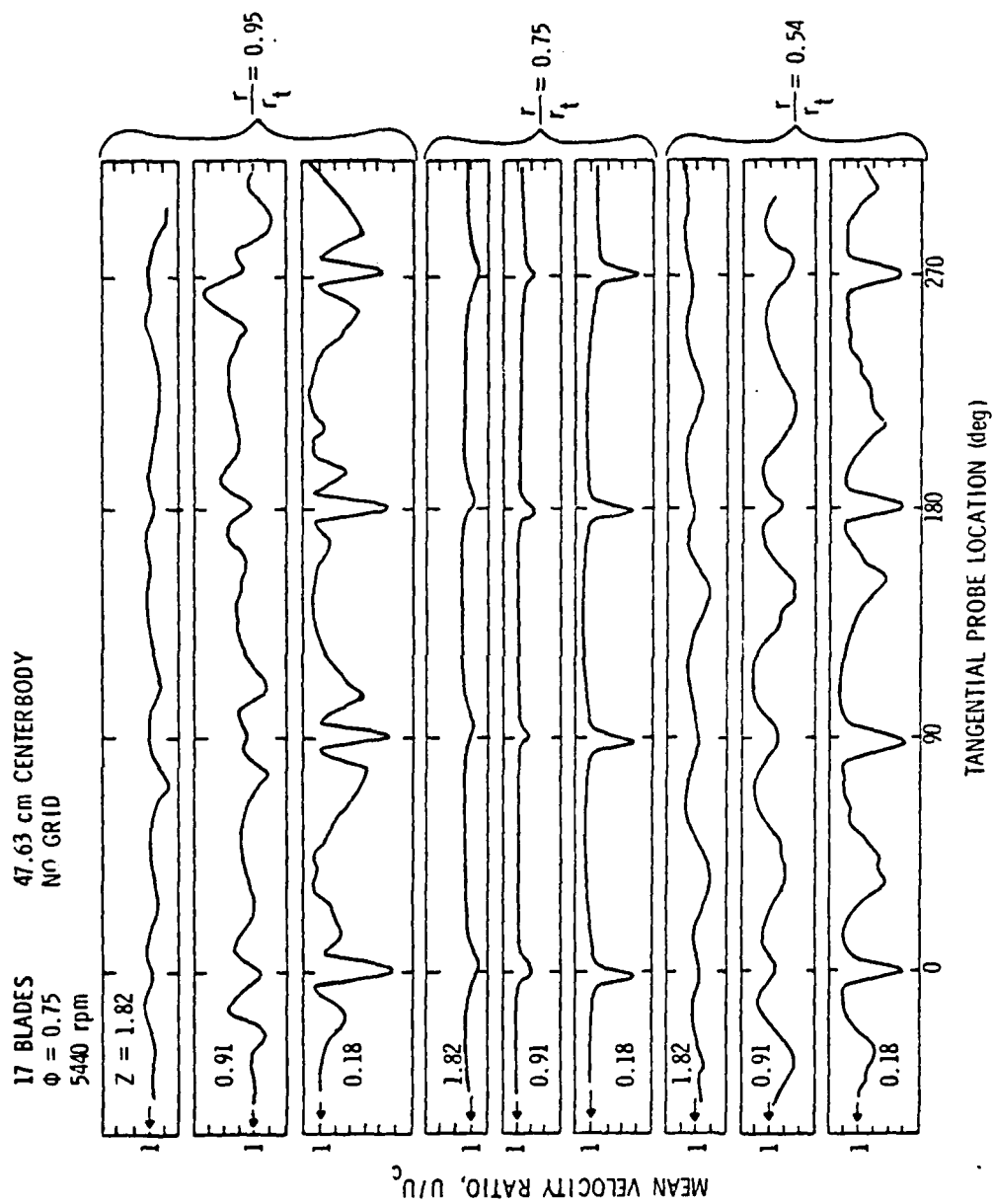Experimental Data.

Figure 47. 360 Degree Wake Survey Mean Velocity Profiles.

sources that were considered were inlet turbulence, wake velocity defect, the maximum turbulence intensity in the strut wake, and the strength of the vortex flow. The noise due to the wake mean velocity defect (Λ) should vary as 20 log Λ when all other blade and flow parameters are held constant. Similarly, the noise due to wake turbulence and the vortex flow should vary as 20 log ($\sqrt{\overline{u'^2}}/U_x$) and 20 log ξ, respectively. The trends estimated from such calculations are shown in Figure 48 along with the measured SPL of the first BPF. While the measured change in tonal intensity is only 2 dB for the range of $Z = 0.18$ to 1.82, the variations estimated due to various sources are substantial. This seems to indicate that the noise due to rotor ingestion of long eddies in the inlet turbulence was the dominate noise source. The observed decrease in tonal noise at BPF with strut spacing is within experimental accuracy. Furthermore, the length scale measurements inside the wake indicate that the long length scales present at the inlet are not shortened as they pass through the strut wake (both free stream and boundary layer eddies).

Installation of the grid has been shown to eliminate the long length scales and is, therfore, more likely to reveal changes in the SPL due to changes in wake parameters. It is evident in Figure 48b that, of the three parameters plotted against the SPL, only the vortex strength shows a similar trend. The vortex strength at an axial spacing of $Z = 1.82$ could not be calculated; however, it is expected that it would have been less than at $Z = 0.18$. Therefore, the wake velocity defect and turbulence intensity are not strong contributors to the rotor noise spectrum.

To determine the effect of vortex flow on the BPF rotor noise, comparisons are made for the flow with the two centerbodies at identical
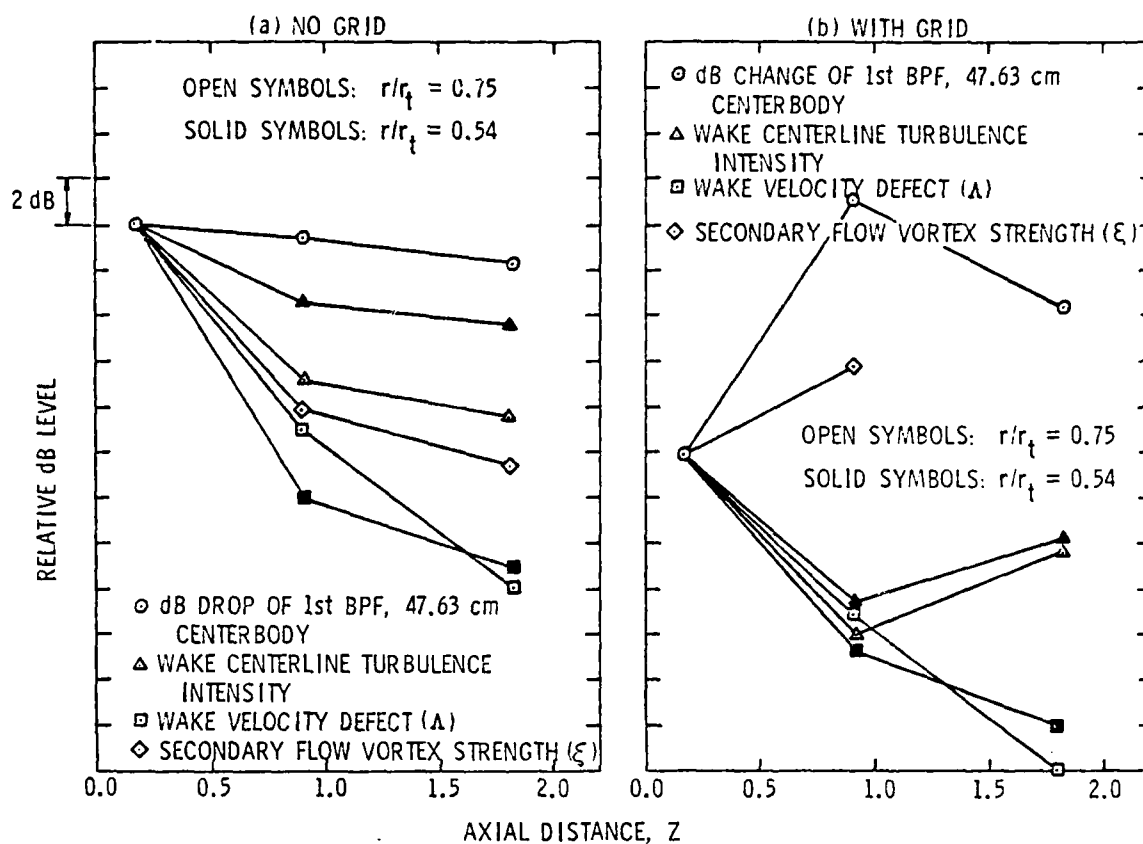
Figure 48. Comparison of Wake Parameters to First BPF, Grid and No Grid Installed.

axial spacings for the case with grid, where the inlet turbulence eddies are short. In Figure 49, the vortex strengths were calculated for the two spacings Z = 0.91 and Z = 1.82 for the long and short centerbodies and plotted against the SPL changes. The wake parameters of velocity profile, wake velocity defect, and wake turbulence are constant between the two centerbodies for a given strut spacing. Good agreement is seen between the vortex strength changes and the SPL. This indicates that noise due to rotor interaction with vortices bould be appreciable in some rotors.

4.3 Aero-Acoustic Measurements of Vortex Flow

In this section, mean velocity profiles and turbulence intensity profiles for various vortex strengths are presented. For all measurements, a grid was installed to decrease the length scales of inlet turbulence. All aerodynamic and acoustic measurements were done using the one strut configuration shown in Figure 7. Figure 50 is a conceptual illustration of the formation of vortex flow. Also shown in Figure 50 is the coordinate system for mean velocities (U_x, U_θ, and U_r) and for the nondimensional tangential probe distance. Tangential velocity was defined positive in the direction of the rotor blade rotation. Typical aeroacoustic data for the various configurations are summarized in Table 5.

4.3.1 Aerodynamic measurements of vortex flow.

4.3.1.1 Mean velocity profiles. The measured axial velocity profiles at r/r_t = 0.55 are shown in Figure 51 as a function of the incidence angle (α). Vortices and the strut wake structure are clearly
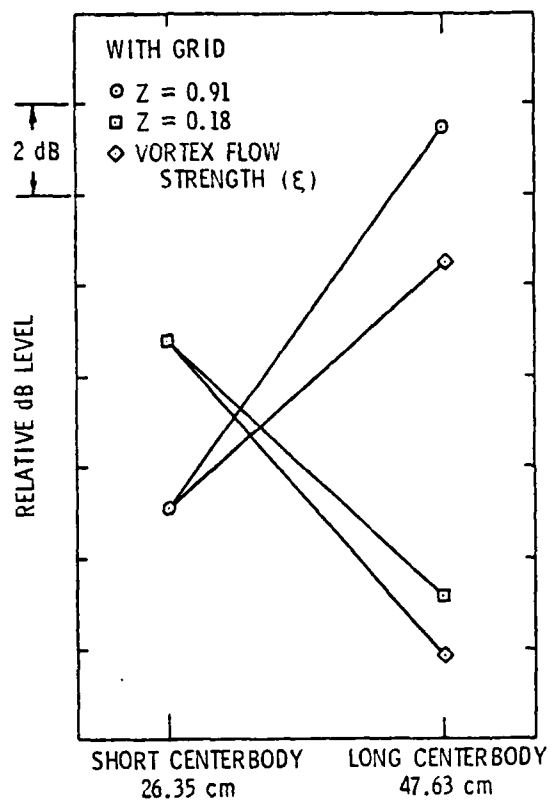
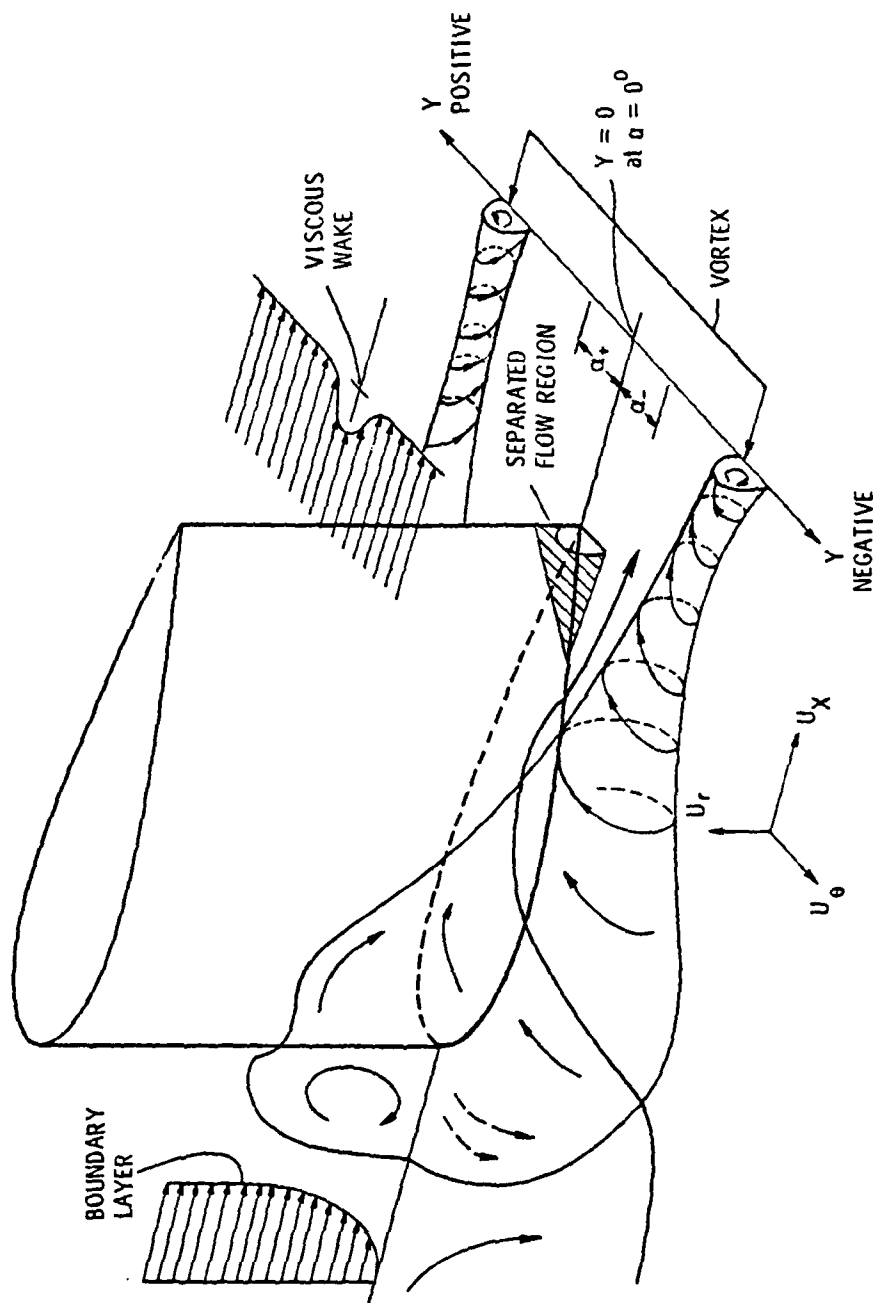Figure 49. Comparison of Vortex Flow Strength to the First BPF,
Grid Installed.

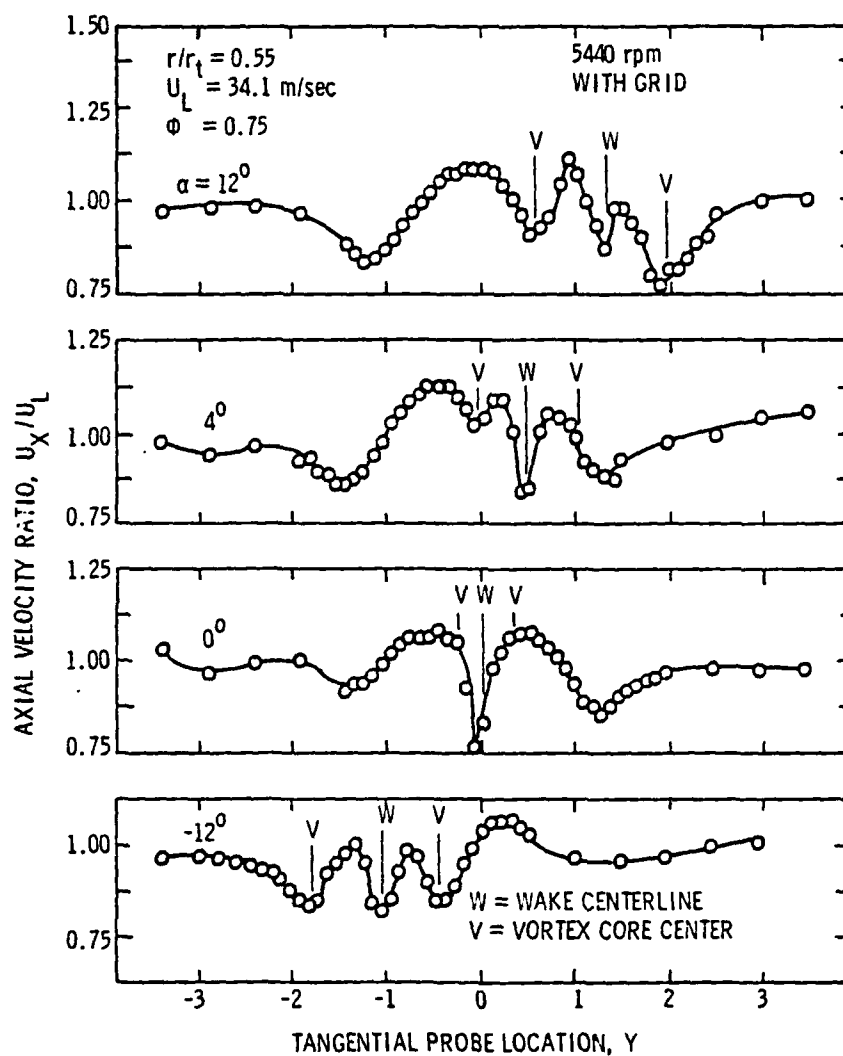Figure 50. Strut Generated Disturbances.

Figure 51. Axial Velocity Profiles at r/r_t = 0.55 for Various Strut Incidence Angles.

apparent in this figure. A comparison of the wake profile (with a short span strut) at $\alpha = 0$ in Figure 51 to the profile at $Z = 0.18$, long centerbody, in Figure 30 revealed a 37 percent reduction in the wake velocity defect due to the decrease in the strut span. No decrease in vortex strength was measured between the two configurations.

Increasing the strut incidence resulted in a stronger vortex on the suction side of the strut. The suction side vortex for the incidence angles of $\alpha = 4$ degrees, 12 degrees, and -12 degrees were located at $Y = -0.1$, 0.6, and -0.6, respectively. The steepening velocity gradient to either side of these locations was an indication of a stronger vortex flow. Concurrent with a stronger suction side vortex was a weaker pressure side vortex. The location of the pressure side vortex core for the incidence angles of $\alpha = 4$ degrees, 12 degrees, and -12 degrees were $Y = 1.0$, 1.9, and -1.7, respectively.

The tangential velocity profiles for the various strut angles are shown in Figure 52. At this radius, the hot wire probe was traversed below the vortex core region. Therefore, the suction side vortex core was located at the maximum value of the nondimensional tangential velocity. At $\alpha = 0$, the vortex cores are located at $Y = \pm 0.6$. The opposite rotation of the vortex pair was clearly measured. Increasing the strut incidence angle increased the magnitude of the tangential velocity from 5 percent at $\alpha = 0$ to 31 percent and 48 percent at incidence angles of $\alpha = 4$ degrees and 12 degrees, respectively. At an incidence of $\alpha = 12$ degrees, a vortex of the same magnitude as the vortex generated by the incidence $\alpha = 12$ degrees was measured, but the vortex rotation was in the opposite direction. The opposite rotation of the vortex was the result of reversing the curvature of the streamline along which vortex
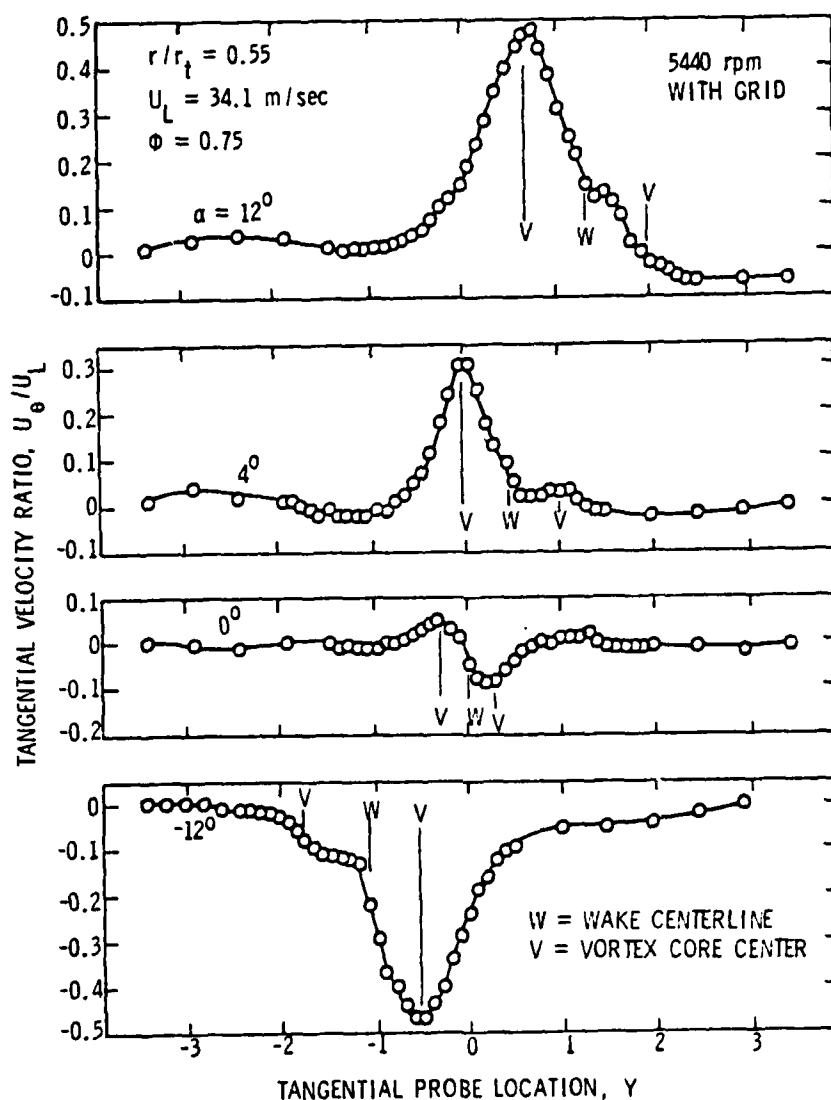
Figure 52. Tangential Velocity Profiles at r/r_t = 0.55 for Various
Strut Incidence Angles.

circulation was developing[43]. The magnitude of the tangential velocity generated by the pressure side vortex was measured to be no greater than 15 percent of the maximum suction side tangential velocity. The point of inflection in the tangential velocity profiles between the suction and pressure side vortices marked the location of the strut wake.

To determine the structure of the vortex, the axial and tangential velocities were measured at various radii for the cases $\alpha = 12$ degrees and $\alpha = -12$ degrees. These strut angles were chosen because they generated the strongest vortices and therefore, were most likely to affect the rotor noise spectra. The measured axial and tangential velocity profiles are shown in Figures 53 through 56.

The axial velocity profiles as a function of radial probe location are shown in Figure 53 for a strut incidence angle of $\alpha = 12$ degrees. The structure of the strut wake was seen to be more coherent in the region near the root of the strut. In the region of the strut tip, flow leakage from the pressure side of the blade to the suction side tended to wash out the strut wake. Velocity measurements at the strut tip revealed no evidence of a strong tip vortex. The wake velocity defect remained nearly constant at 14 percent of the local free stream velocity at the strut root.

The suction side and pressure side vortices are located at $Y = 0.6$ and 1.9, respectively. The size and strength of these vortices are shown in Figure 54. The suction side vortex was found to extend from the strut root to $r/r_t = 0.59$. This corresponds to a vortex diameter of 0.85 cm, or two-thirds the span of the strut (1.27 cm). The vortex diameter was nondimensionalized by the local rotor blade spacing (1.84 cm at $r/r_t = 0.57$) to yield a tangential probe distance of 0.46. This

Figure 53. Axial Velocity Profiles at α = 12 Degrees for Various Radii.

Figure 54. Tangential Velocity Profiles at α = 12 Degrees for Various Radii.
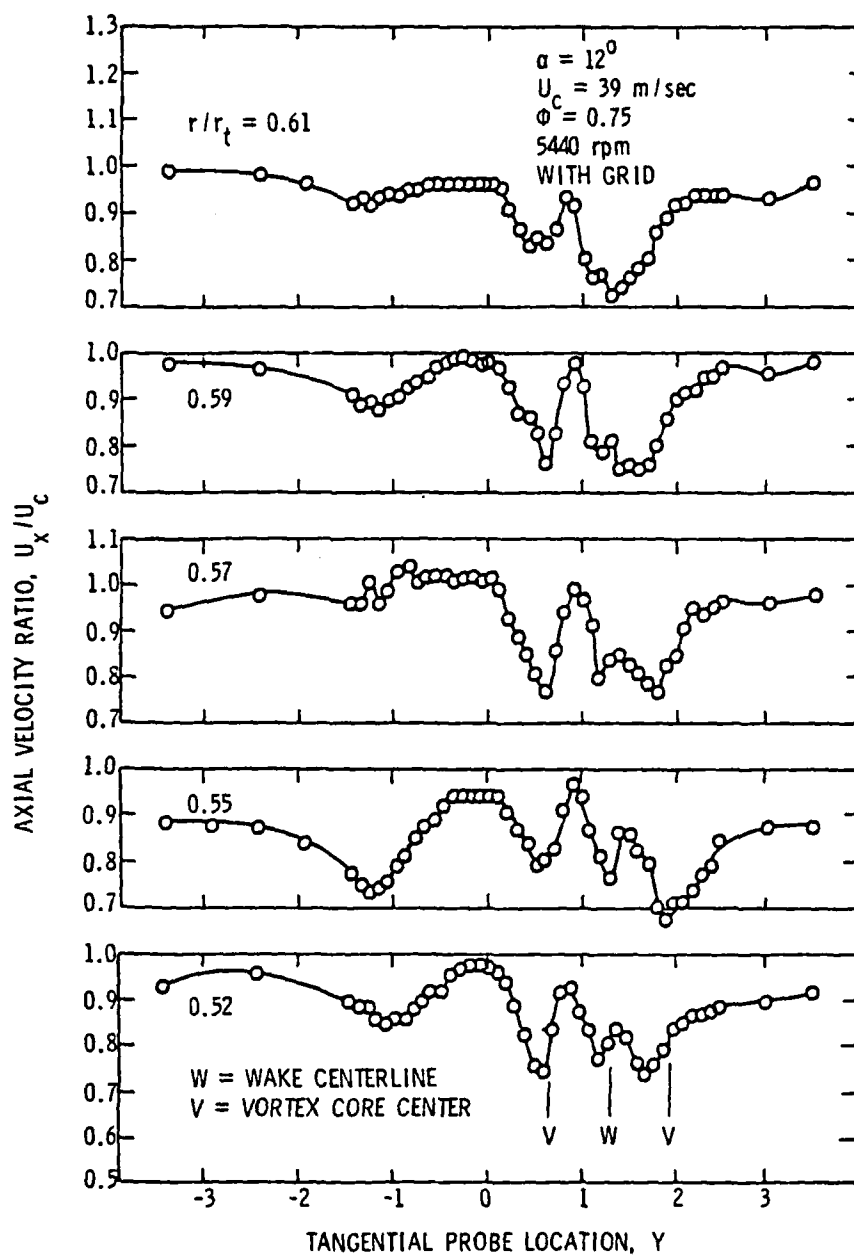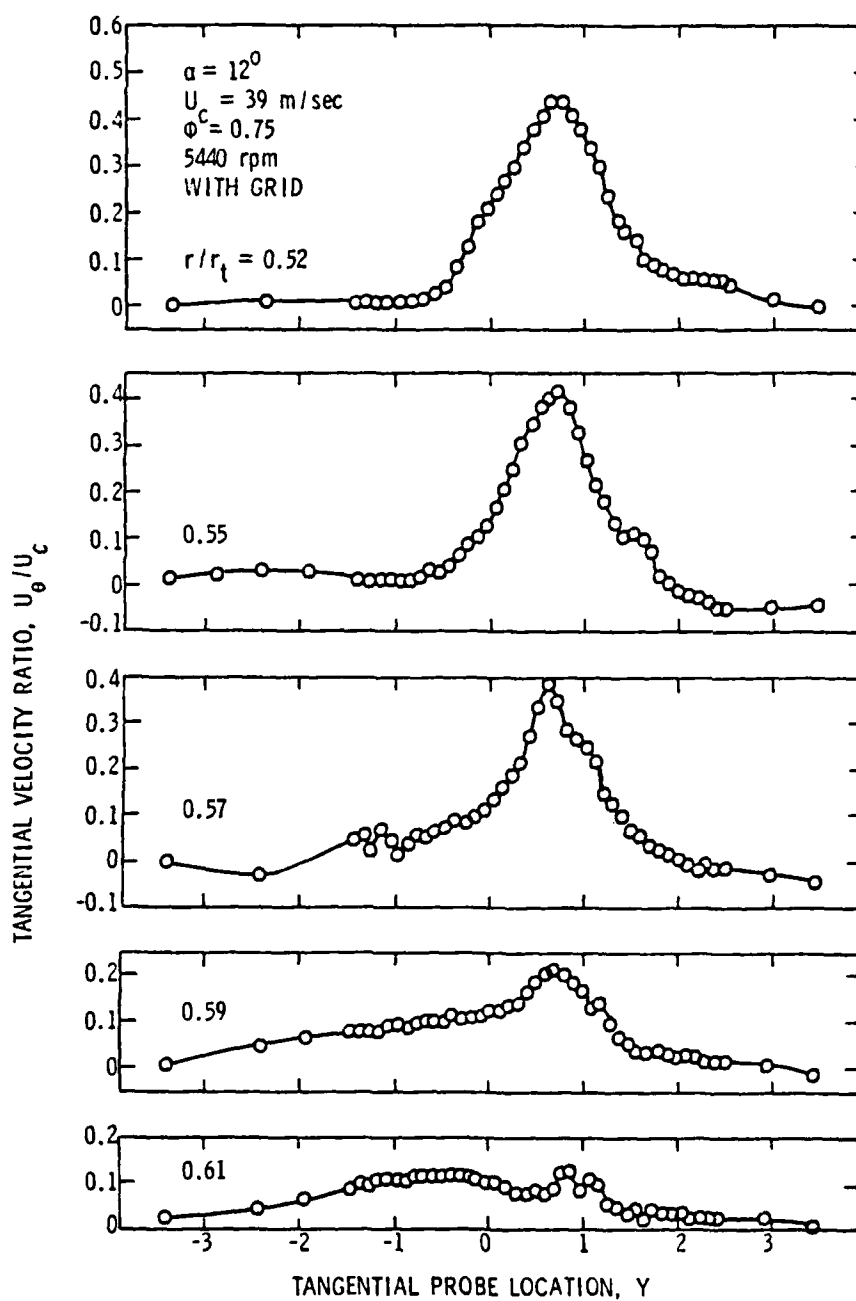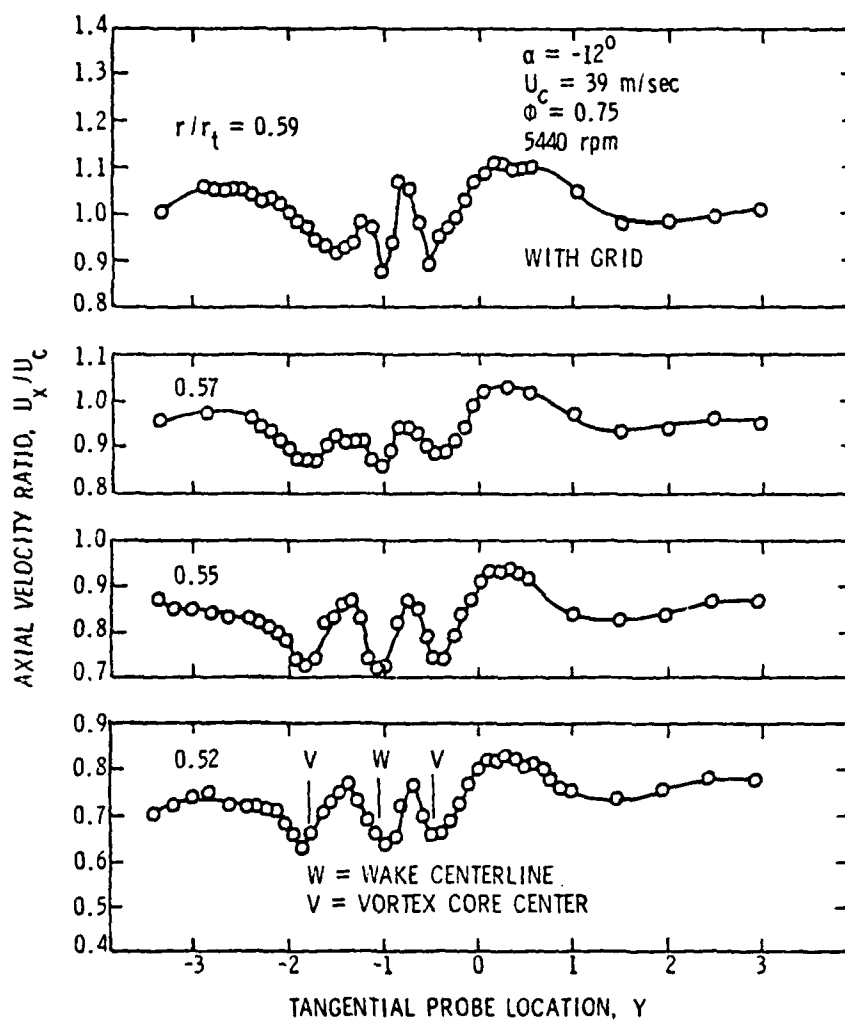
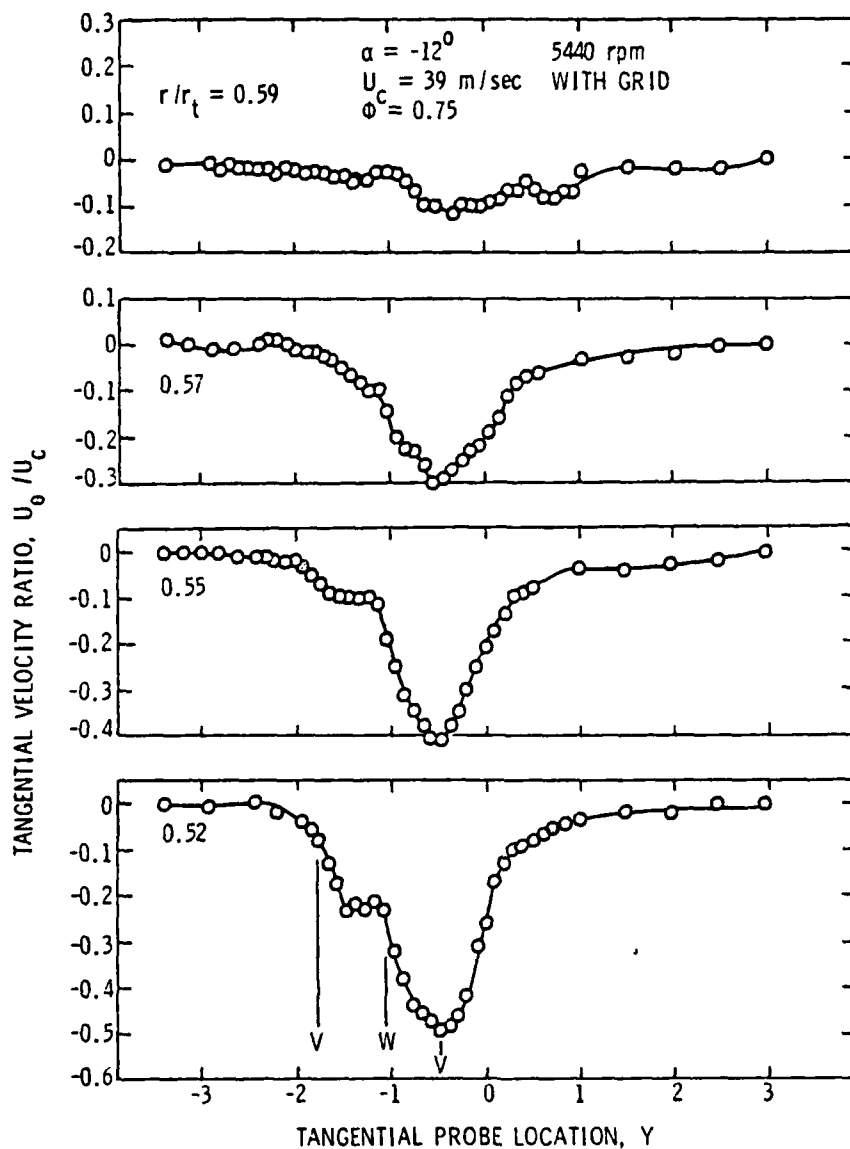Figure 55. Axial Velocity Profiles at α = -12 Degrees for Various Radii.

Figure 56. Tangential Velocity Profiles at $\alpha = -12$ Degrees for Various Radii.

corresponds to the distance measured on the tangential velocity profile at $r/r_t = 0.57$. In contrast to the suction side vortex, the pressure side vortex extended no farther than $r/r_t = 0.55$. Therefore, the size of the pressure side vortex was less than half the size of the suction side vortex. Based on these data, the contribution of the pressure side vortex to rotor noise was believed to be overshadowed by the dominant suction side vortex.

The effect of negative strut incidence ($\alpha = -12$ degrees) on the axial velocity profile is shown in Figure 55. A comparison of Figure 55 to Figure 53 shows the $\alpha = -12$ degree profiles to be reversed from the profiles at $\alpha = 12$ degrees, but otherwise similar. The wake center-line, pressure and suction side vortices are now located at $Y = -1.2$, -1.7, and -0.6, respectively. At the strut tip, the wake structure was again seen to collapse due to tip flow leakage, as in the $\alpha = 12$ degree case. The strut wake velocity defect was 14 percent of the free stream velocity.

The size and strength of the vortices for $\alpha = -12$ degrees are shown in the tangential velocity profiles of Figure 56. A comparison of the tangential velocities of the $\alpha = -12$ degree and $\alpha = 12$ degree cases reveal the vortices to be of the same magnitude, but of opposite rotation (compare Figures 54 and 56). The direction of vortex rotation and, hence, the direction of the tangential velocity is believed to be important by virtue of its effect on the angle of attack at which the rotor blade is operating. Positive tangential velocities vectorially add with the relative velocity due to rotor blade rotation and with the axial velocity to increase the rotor blade angle of attack. The increased angle of attack should increase the rotor blade thrust and, therefore, lead to a

higher noise level. Conversely, a negative tangential velocity (case $\alpha = -12$ degrees) subtracts from the relative velocity due to rotor blade rotation and this reduces the rotor blade angle of attack. A decreased angle of attack reduces the rotor thrust and, therefore, should lead to a lower noise level. Acoustic measurements to be discussed in the following section verify this result.

4.3.1.2 Turbulence intensity profiles. The axial and tangential turbulence intensities are plotted in Figures 57 and 58 for $r/r_t = 0.55$ for various strut incidence angles. In Figure 57, the maximum axial turbulence values were measured at the wake centerline, and at the vortex core when the strut incidence angle is nonzero. The axial peaks occurring at $Y = -1.25$ for the cases $\alpha = 12$ degrees and 4 degrees, $Y = \pm 1.25$ for $\alpha = 0$ degree, and $Y = 1.25$ for $\alpha = -12$ degrees may be due to the presence of the edge of the vortex in these regions. For a combined vortex, the intensities should peak near the outer edge of the core.

The increase in the strut incidence generally resulted in a decrease in the axial turbulence intensity at the wake centerline. The 25 percent decrease in axial intensity at the strut wake center from the $\alpha = 0$ degree to the $\alpha = 12$ degree case is believed to be higher due to the generally lower free stream turbulence levels measured for the $\alpha = 12$ degree case. A more realistic value of 6 percent is obtained if the $\alpha = 0$ degree and $\alpha = -12$ degree cases are compared.

The axial turbulence intensities near the vortex core exhibited a significant rise with increasing strut incidence angle. At $\alpha = 0$ degree the axial intensity of the vortices was 3 percent. The axial turbulence
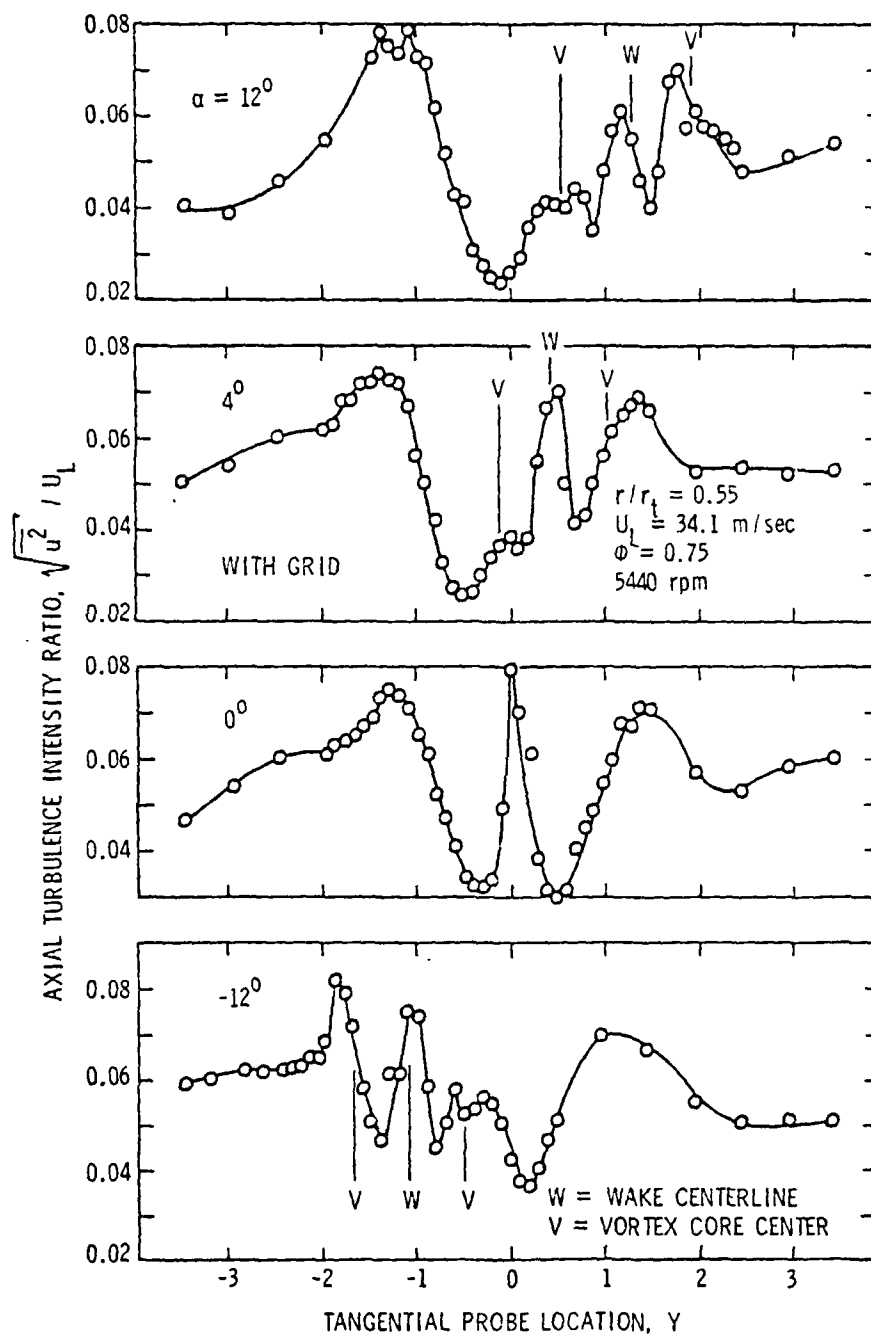
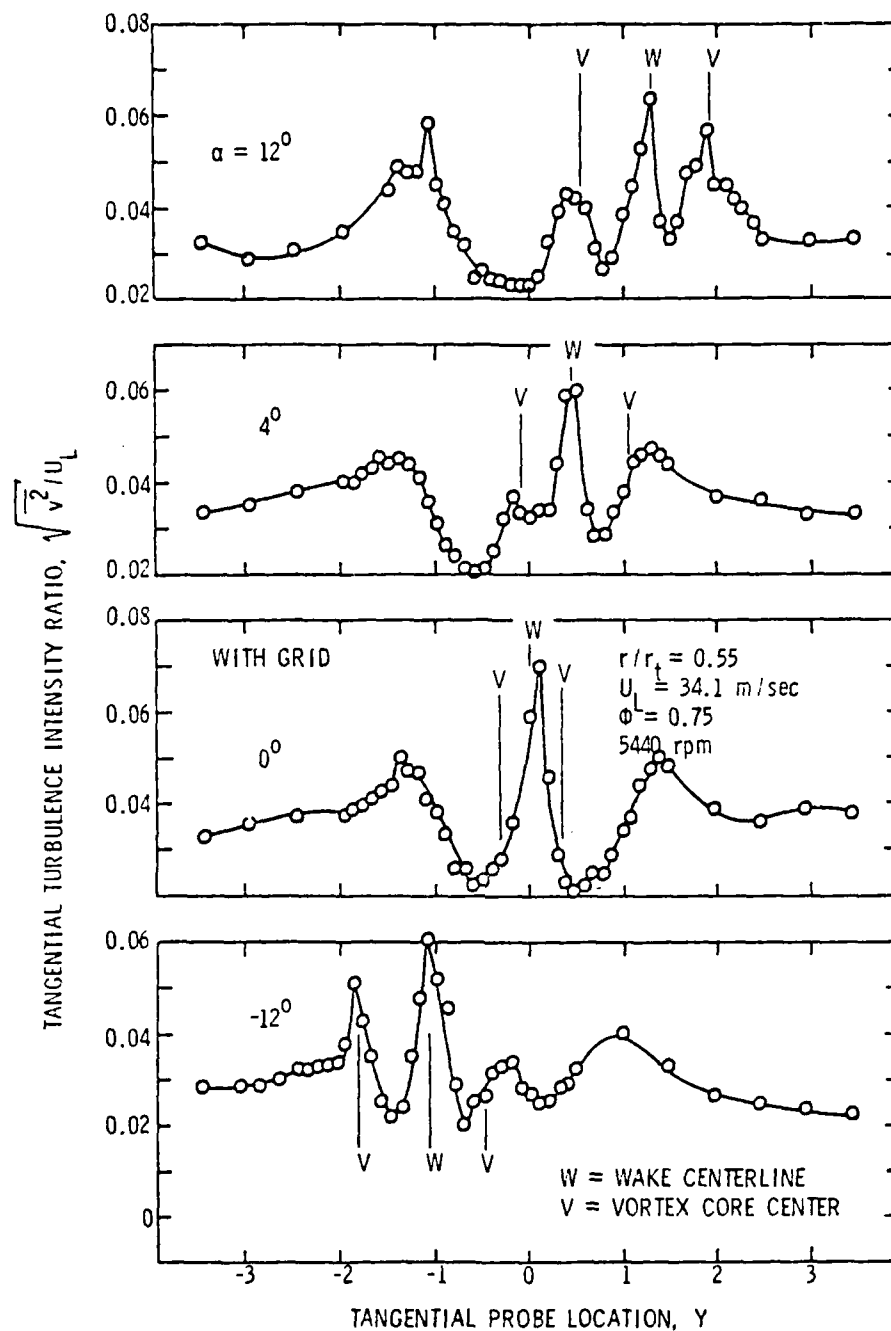Figure 57. Axial Turbulence Intensity Profiles at $r/r_t = 0.55$ for Various Strut Incidence Angles.

Figure 58. Tangential Turbulence Intensity Profiles at $r/r_t = 0.55$ for Various Strut Incidence Angles.

intensity at the suction side vortex core increased by 30 percent as α varied from 0 degree to ±12 degrees. The largest increase in axial intensity, however, occurred at the pressure side vortex core centerline. The axial turbulence intensity near the pressure side vortex core doubled from the α = 0 degree case to the α = ±12 degree cases. The higher turbulence levels of the pressure side vortex are to be expected, because the vortex flow is developing under an adverse pressure gradient.

Meaurements of the tangential turbulence intensities are shown in Figure 58 for various incidence angles. The tangential turbulence intensity in the free stream was 3 percent of the mean velocity. This was 25 percent lower than the free stream axial turbulence intensity. Peaks of 5 percent in the turbulence intensity profile occur at Y = ±1.25. For the strut incidence of α = 0, the measured tangential intensities at the wake and vortex core centerlines were 7 percent and 2.2 percent, respectively.

The effect of increasing the strut incidence angle on the tangential component of turbulence follows the same pattern as was discussed for the axial component of turbulence intensity. The tangential turbulence intensity at the strut wake centerline decreased by 7 percent as incidence angle increased to α = ±12 degrees. Finally, the level of tangential turbulence intensity at both the suction and pressure side vortex cores rises with increasing incidence angle. The tangential intensities in the suction and pressure side vortex cores increased by a factor of 1.0 and 1.5, respectively, with strut incidence angle. This was to be expected, since the high strut incidence angles are producing stronger vortices.

For the cases of α = ±12 degrees, the flow field was measured at various radii to obtain a more complete picture of the turbulence structure generated by the vortex flow. In Figures 59 and 60, the axial and tangential components of turbulence intensity are plotted at various radii for the case of α = 12 degrees. Beginning with the strut wake, the axial and tangential components of turbulence intensity at the wake centerline are fairly constant with radius. Axial and tangential turbulence intensities at the wake centerline were 6.3 percent and 4.9 percent, respectively. The peak intensities due to vortex flow occur at the edge of the core or the mixing region. As can be seen, this occurs at $Y = ±1.0$, their values being maximum near the centerbody. The maximum values of axial turbulence intensity decrease continuously from 0.075 to 0.03 on the suction side and remain fairly constant on the pressure side.

The axial and tangential turbulence intensity profiles at various radii for α = -12 degrees are shown in Figures 61 and 62. At α = -12 degrees, the locations of the wake centerline and the vortices are reversed from those at α = 12 degrees.

The turbulence levels at the strut wake centerline did not show a significant variation with radial probe location. Typical levels of the axial and tangential components of turbulence intensity were 6 percent and 5.7 percent, respectively. These turbulence levels are similar to those in the α = 12 degree case.

In Figures 61 and 62, the turbulence intensities are seen to peak at the edge of the suction and pressure side vortex locations. The suction side vortex core and outer edge region were again found at the radial locations of $r/r_t = 0.55$ and $r/r_t = 0.59$, respectively. The axial and tangential turbulence intensities at the core were 4.7 percent

Figure 59. Axial Turbulence Intensity at α = 12 Degrees for Various Radii.

Figure 60. Tangential Turbulence Intensity at α = 12 Degrees for Various Radii.
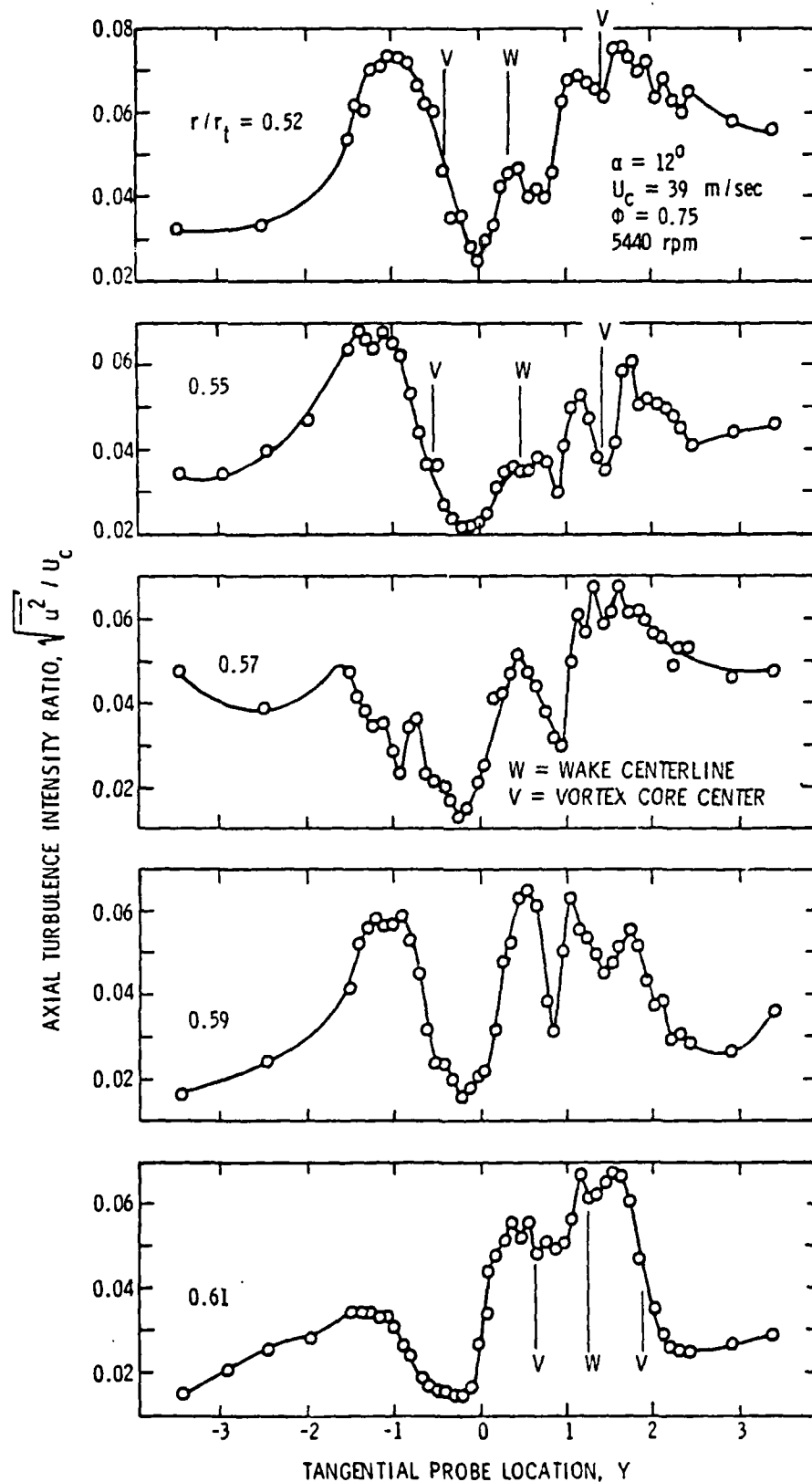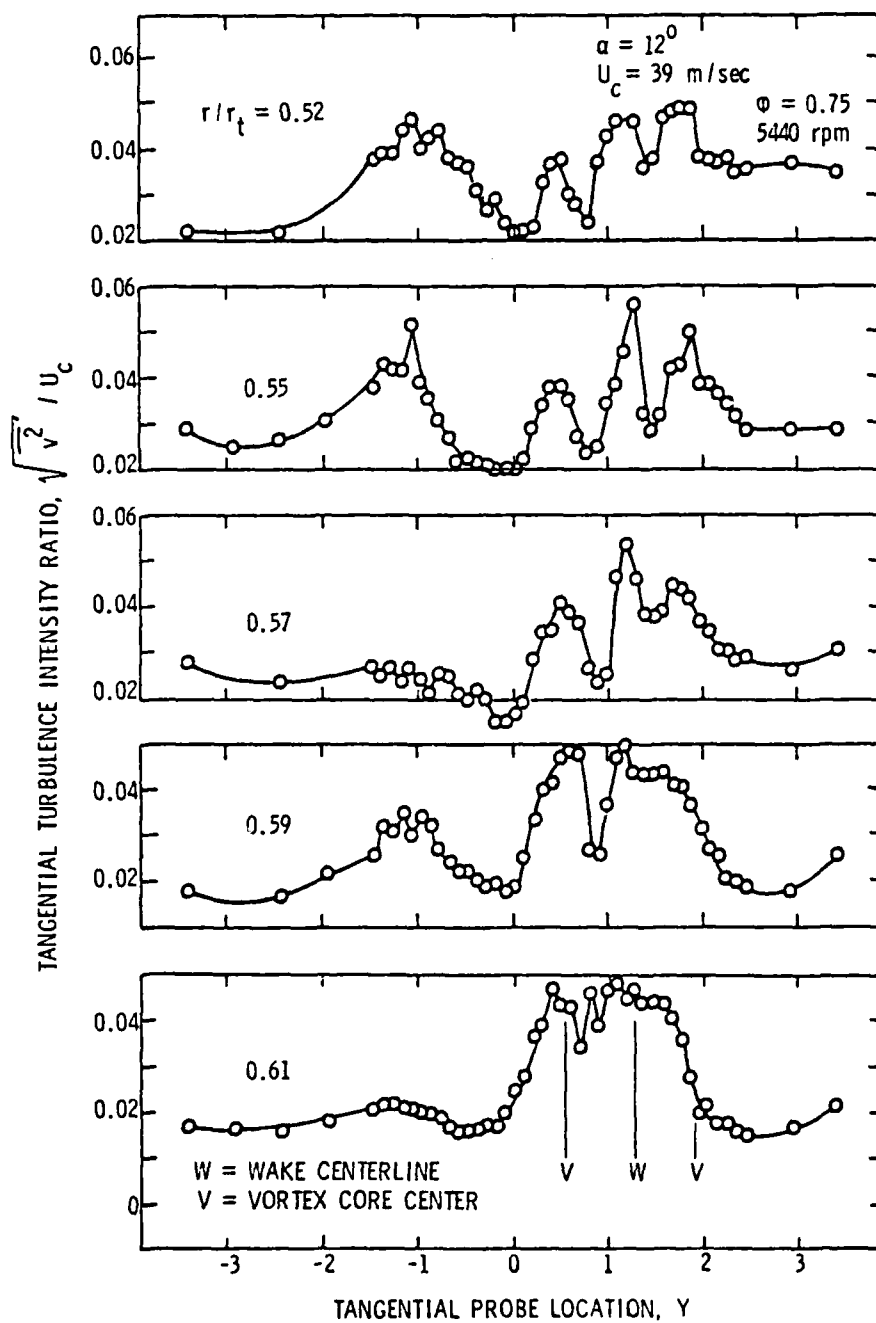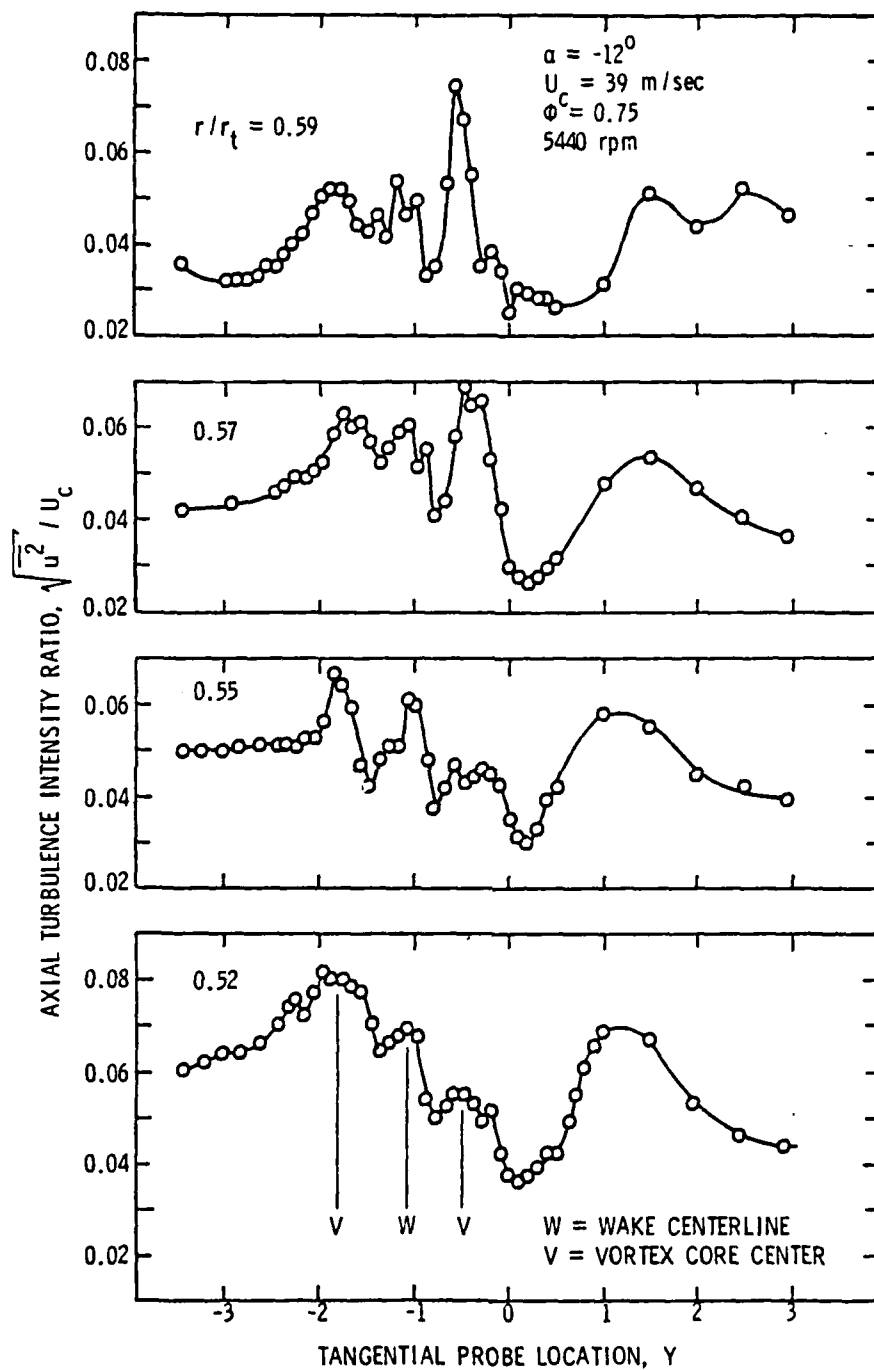
Figure 61. Axial Turbulence Intensity at α = -12 Degrees for Various Radii.

Figure 62. Tangential Turbulence Intensity at $\alpha = -12$ Degrees for Various Radii.

and 3.5 percent of the mean flow velocity. At the outer edge of the

vortex region, the maximum axial and tangential components of turbulence

intensities were 8 and 5 percent, respectively. When these results were

compared to the $\alpha = 12$ degree case, it was found that the turbulence

intensities measured with $\alpha = -12$ degrees were on the order of 10 percent

higher than those for the $\alpha = 12$ degree case. Analysis of the experi-

mental data revealed the free stream axial turbulence intensity for

$\alpha = -12$ degrees to be 4 percent of the mean velocity, as opposed to

3 percent for the $\alpha = 12$ degree case. The free stream tangential tur-

bulence intensity level was the same for both cases. Reviews of the

experimental procedure indicated that the data for the two cases were

recorded on two separate days. Therefore, it was concluded that the

differences noted may be due to different atmospheric conditions which

result in different levels of inlet turbulence.

4.3.2 Acoustic data and interpretation.

4.3.2.1 Sound spectra data. The sound spectra for four

struts at the various incidence angles of $\alpha = \pm 12$ degrees, 4 degrees,

and 0 degree are shown, along with the natural boundary layer (NBL)

case, with the grid installed, in Figure 63. For the NBL case, the SPL

of the first BPF (1541 hz) was 81 dB. Installation of the shorter struts

at $\alpha = 0$ degrees resulted in a 2.6 dB increase in the BPF. The effect

of shortening the strut span on the rotor noise can be determined by com-

paring this case to the case of $Z = 0.18$ with a 57.63 cm centerbody and

with grid installed as shown in Figure 42. Decreasing the strut span

from 4.38 cm to 1.37 cm resulted in a 3 to 4 dB drop in the first BPF

harmonic plus the disappearance of the second and third BPF harmonics
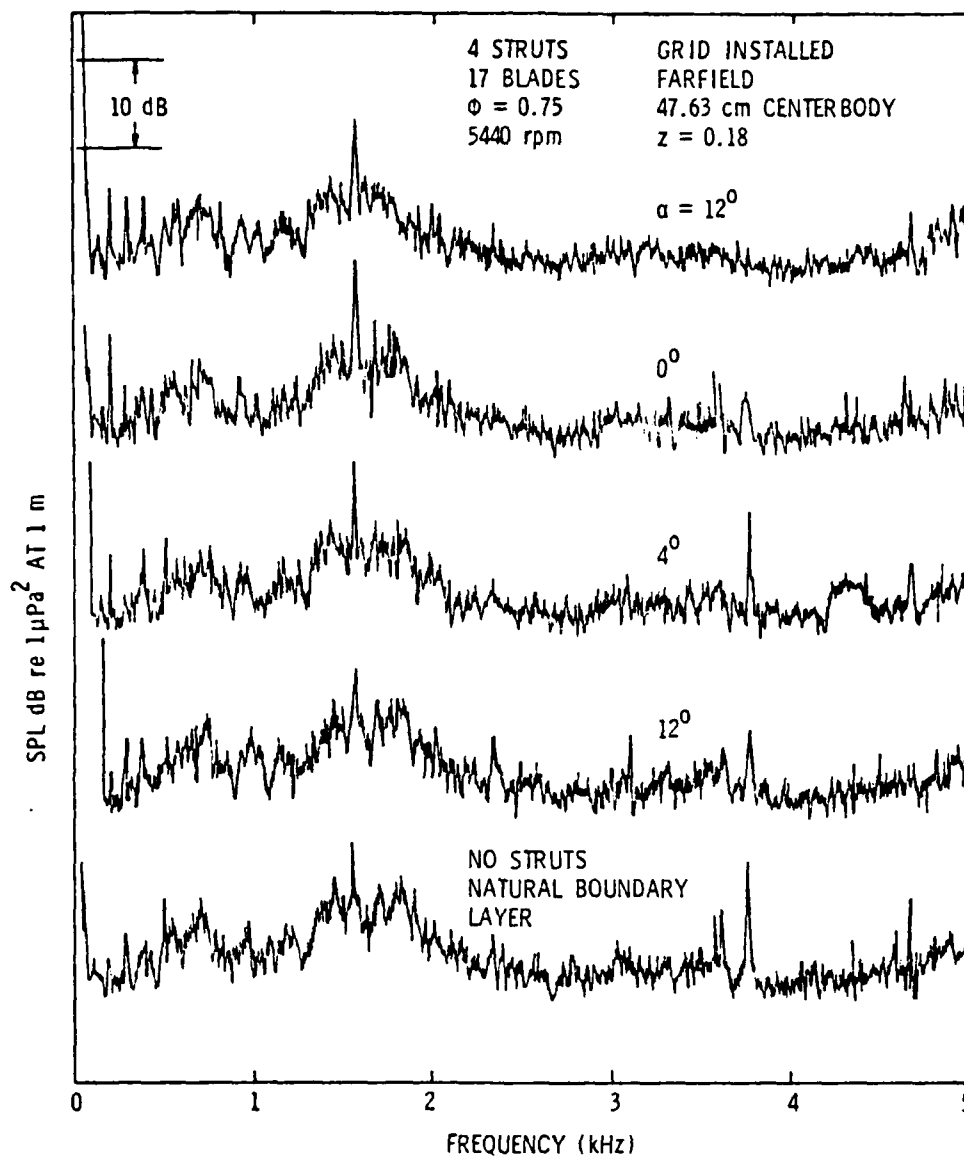
Figure 63. Sound Spectra for Four Struts at Various Incidences With Grid Installed.

and all SPF (strut passing frequency) harmonics. This decrease in the SPL of the first BPF is believed to be due mainly to the removal of the vortex flow generated at the strut tip. The magnitude of the vortex flow at the root of the strut was the same for both cases. Removal of the strut wake was not the source of the noise reduction since data reported in the previous section showed rotor noise to be relatively unaffected by the wake.

Varying the incidence angle of the struts resulted in only a ±1 dB change in the SPL of the first BPF for the cases of ±12 degrees. Because this change in the SPL was on the order of the accuracy of the experimental measurements, it was decided to remove three of the struts to increase the effect of the vortex flow on the first BPF. By varying the strut incidence from α = 12 degrees to α = -12 degrees, the change in the first BPF harmonic was significantly higher.

The sound spectra for the single short strut at incidence angles varying from α = -12 degrees to 12 degrees are shown in Figure 64. At α = 0 degrees the SPL of the first BPF increased less than 1 dB over the NBL case. As the incidence angle was increased in increments of 4 degrees, the SPL of the first harmonic initially increased to 84.6 dB at α = 4 degrees then decreased to 84.3 dB and 83 dB at α = 8 degrees and 12 degrees, respectively. At negative incidence angles, the SPL of the first BPF steadily increased from 83.2 dB at α = -4 to 83.7 dB at α = -8 degrees, and finally, to 87.6 dB at α = -2 degrees. The broadening of the peak at the first harmonic was due to the grid induced turbulence.

4.3.2.2 <u>Correlation of the acoustic data</u>. A comparison is shown in Figure 65 of the measured SPL of the first BPF for the one and
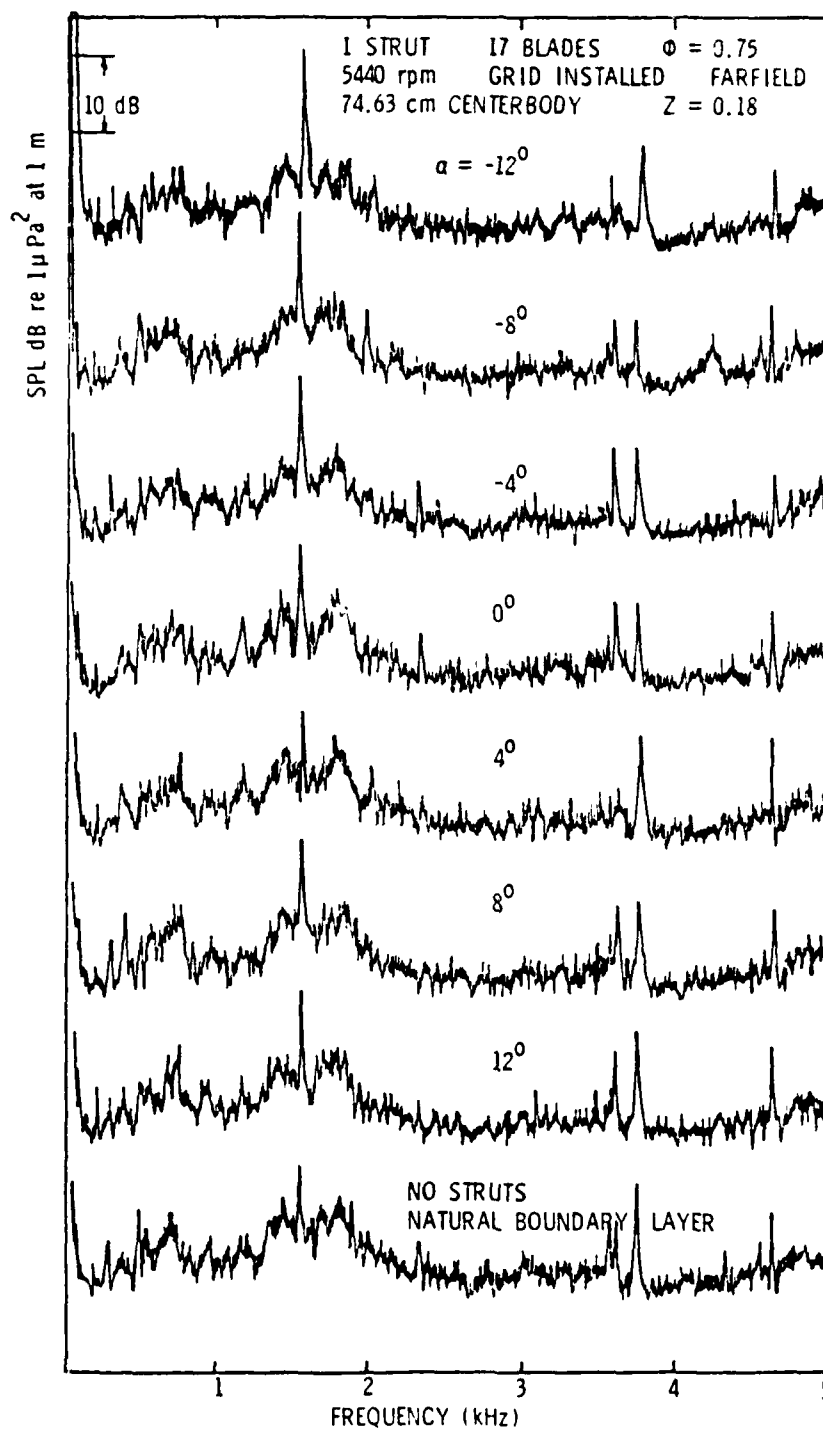
Figure 64. Sound Spectra for One Strut at Various Incidences With Grid Installed.

four strut cases with the unsteady thrust analysis due to Thompson[18] and with the variation of the measured vortex strength. The measured velocity profiles at several radii for the cases $\alpha = \pm 12$ degrees, 4 degrees, and 0 degree were Fourier analyzed to obtain the harmonic coefficients. The calculated trends of unsteady thrust based on these coefficients did not agree with the measured SPL of the first BPF. This confirms the results from the previous section that the limited wake structure was not a major noise source.

The strengths of the vortices for the cases of $\alpha = 12$ degrees were calculated from the variation of tengential velocity with radial location, shown previously in Figures 54 and 56. If the vortex strength is evaluated on a radial line through the vortex core, where the radial component of velocity is zero, the equation for the vortex strength [Equation (4.5)] reduces to the equation shown below.

$$\xi = - \frac{\partial U_\theta}{\partial r} \ . \tag{4.10}$$

The variation of the vortex strength was calculated as 20 log ξ. It is apparent from Figure 65 that, for the cases $\alpha = \pm 12$ degrees, the change in the vortex strength agrees well with the change in the SPL of the first BPF. Therefore, the strength of the vortex was seen as possible as a major rotor noise source. Finally, in comparing trends of possible noise source sound pressure levels at blade passing frequency, one can only eliminate possible sources. In order to truly ascertain a source or sources, a comparison of levels must also be made.
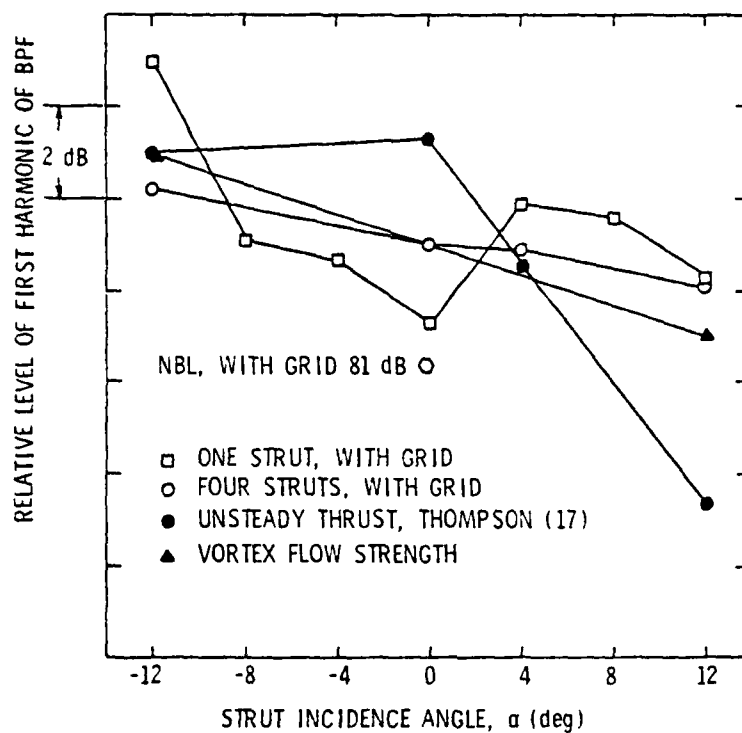
Figure 65. Comparison of Unsteady Rotor Thrust and Vortex Flow
Strength to Experimental Data.

CHAPTER V

CONCLUSIONS

The following major conclusions can be drawn from this study of the behavior of inlet turbulence and strut generated disturbances on a rotor noise spectrum:

1. The hypothesis by earlier investigators on the effect of a statis facility on the elongation of eddies has been confirmed. The measurements indicate that eddies are stretched as much as ten times their original length. This depends on the contraction ratio and the inflow turbulence properties. Long eddies are a major source of BPF noise in this static facility. They overshadow all other sources.

2. In the presence of these long eddies, the strut wake (mean velocity defect) is not a major source of noise.

3. The sound pressure level due to unsteady thrust computed from the measured mean velocity wake profiles does not correlate well with the trend exhibited by the BPF pure tone noise.

4. The vortex flow generated near the intersection of the strut with the inner and outer annulus walls emerged as a possible major noise source in the absence of large inlet turbulence effects (i.e., long turbulent eddies).

5. In addition to the strength of the vortex flow, the direction in which the vortex was rotating was seen as possible important parameter in the magnitude of the

rotor noise generated.

6. These conclusions are valid for low Mach number turbo-machinery. At high Mach numbers, the relative importance of these sources may change.

REFERENCES

1. Tam, C. K. W., "Turbulent Boundary Layer Noise", Journal of the Acoustical Society of America, Vol. 57, 1975, pp. 25-34.

2. Lakshminarayana, B., "Influence of Turbulence on Fan Noise," Proceedings of First Ventilation System/Cooling Fan Noise Workshop, David W. Taylor Naval Ship Research and Development Center, edited by M. Sevik and J. V. Pierpoint, November 1975.

3. Robbins, B. E., "Turbulence Induced Noise in a Single Stage Axial Flow Fan," M.S. Thesis, Aerospace Engineering, The Pennsylvania State University, 1974.

4. Moiseev, N. A., "Noise Due to the Interaction of Boundary Layer Turbulence With a Marine Propulsor or an Aircraft Compressor," M.S. Thesis, Engineering Acoustics, The Pennsyvlania State University, 1977.

5. Ffowcs-Williams, J. E., and Hawkings, D. L., "Theory Relating to the Noise of Rotating Machinery," Journal of Sound and Vibration, Vol. 10, 1969, pp. 10-12.

6. Chandrashekara, N., "Sound Radiation From Random Quadrupole Source Distributions in Axial Flow Fans," Journal of Sound and Vibration, Vol. 19, 1971, p. 133.

7. Sofrin, T. G. and McCann, J. C., "Pratt and Whitney Experience in Compressor Noise Reduction," Acoustical Society of America paper presented at November 1-5, 1966 meeting, Los Angeles, Calif.

8. Sharland, I. J., "Sources of Noise in Axial Flow Fans," Journal of Sound and Vibration, Vol. 1, 1964, pp. 302-321.

9. Curle, N., "The Influence of Solid Boundaries Upon Aerodynamic Sound," Proceedings of the Royal Society, Vol. 231A, 1955, pp. 505-514.

10. Liepmann, H. W., "On the Application of Statistical Concepts of the Buffeting Problem," Journal of Aeronautical Science, Vol. 19, 1952, pp. 793-800.

11. Morfey, C. L., "Broadband Sound Radiated from Subsonic Rotors," in Fluid Mechanics, Acoustics, and Design of Turbomachinery, edited by B. Laksminarayana, W. R. Britsch, and W. S. Gearhart, National Aeronautics and Space Administration Special Publication No. 304 (Part II), 1974, p. 461.

12. Mugridge, B. D., and Morfey, C. L., "Sources of Noise in Axial Flow Fans," Journal of Acoustical Society of America, Vol. 51, 1972, pp. 1411-1426.

13. Sevik, M., "Sound Radiation from a Subsonic Rotor Subject Turbulence," in Fluid Mechanics, Acoustics, and Design of Turbomachinery, edited by B. Laksminarayana, W. R. Britsch, and W. S. Gearhart, National Aeronautics and Space Administration Special Publication No. 304 (Part II), 1974, p. 493.

14. Mani, R., "Noise Due to Interaction of Inlet Turbulence with Isolated Stators and Rotors," Journal of Sound and Vibration, Vol. 17, 1971, pp. 251-260.

15. Sears, W. R., "Some Aspects of Nonstationary Aerofoil Theory and Its Practical Application," Journal of Aeronautical Science, Vol. 8, 1941, pp. 104-108.

16. Robbins, B., and Lakshminarayana, B., "Effect of Inlet Turbulence on Compressor Noise," Journal of Aircraft, Vol. 2, 1974, pp. 273-281.

17. Whitehead, D. S., "Force and Moment Coefficients for Vibrating Aerofoils in Cascade," British ARC R and M 3254, 1960.

18. Thompson, D. E., "Propeller Time-Dependent Force Due to Nonuniform Flow," Ph.D. Thesis, Aerospace Engineering, The Pennsylvania State University, 1976.

19. Pickett, G. F., "Effects of Non-Uniform Inflow on Fan Noise," Acoustical Society of America paper presented at April 23-26, 1974 meeting, New York City, N.Y.

20. Mugridge, B. D., "Gust Loading on a Thin Airfoil," The Aeronautical Quarterly, Vol. 22 (Part III), 1971, pp. 301-310.

21. Lowson, M. V., "Rotor Noise Radiation in Nonuniform Flow," Paper D2, Aerodynamic Noise Symposium, Loughborough University of Technology, England, September 1970.

22. Hanson, D. B., "A Study of Subsonic Fan Noise Caused by Atmosphere Turbulence," Journal of Acoustical Society of America, Vol. 56, 1974, pp. 110-126.

23. Moiseev, N., Lakshminarayana, B., and Thompson, D. E., "Noise Due to Interaction of Boundary-Layer Turbulence with a Compressor Rotor," Journal of Aircraft, Vol. 15, No. 1, 1978, pp. 53-61.

24. Homicz, G. F. and George, A. R., "Broadband and Discrete Frequency Radiation from Subsonic Rotors," Journal of Sound and Vibration, Vol. 36, 1974, pp. 151-177.

25. Lowson, M. V., Whatmore, A. R., and Whitfield, C. E., "Source Mechanisms for Rotor Noise Radiation," National Aeronautics and Space Administration Contract Report No. 2077, August 1973,

26. Dittmar, James H., "Interaction of Rotor Tip Flow Irregularities with Stator Vanes as a Noise Source," National Aeronautics and Space Administration Technical Memorandum No. 73706, October 1977.

27. Cumpsty, N. A., and Lowrie, B. W., "The Cause of Tone Generation by Aero Engines at High Subsonic Tip Speeds and Effect of Forward Speed," Transactions of American Mechanical Engineers, Series B, Journal of Engineering for Power, 1974, pp. 228-234.

28. Goldstein, M. E. Rosenbaum, B. M., and Albers, L. V., "Sound Radiation from a High Speed Axial Flow Fan Due to the Inlet Turbulence Quadrupole Interaction," National Aeronautics and Space Administration Technical Note No. D7667, June 1974.

29. Cumpsty, N. A., "Review--A Critical Review of Turbomachinery Noise," ASME Journal of Fluids Engineering, June 1977.

30. VonFrank, E. D., "Turbulence Characteristics in the Mixing Region of an Unperturbed Round Jet," M.S. Thesis, Aerospace Engineering, The Pennsylvania State University, 1970.

31. Tennekes, H., and Lumley, J. L., A First Course in Turbulence, The MIT Press, 1974.

32. Klatt, F., "The X Hot-Wire Probe in a Plane Flow Field," DISA Information, No. 8, July 1969.

33. Anand, A. and Lakshminarayana, B., "An Experimental and Theoretical Investigation of Three Dimensional Turbulent Boundary Layers Inside the Passage of a Turbomachinery Rotor," National Aeronautics and Space Administration Contract Report No. 2888, 1977.

34. Reynolds, B. and Lakshminarayana, B., "Characteristics of Lightly Loaded Fan Rotor Blade Wakes," National Aeronautics and Space Administration Contract Report No. 3188, 1979.

35. Ribner, H. S. and Tucker, M., "Spectrum of Turbulence in a Contracting Stream," NACA Report No. 1113, August 1951.

36. Bekofsky, K. L., Sheer, R. E., and Wang, J. C. F., "Fan Inlet Disturbances and Their Effect on Static Acoustic Data," American Society of Mechanical Engineers Paper No. 77-GT-63, March 1977.

37. Shaw, L. M., Woodward, R. P., Glaser, F. W., and Daetoli, B. J., "Inlet Turbulence and Fan Noise Measured in an Anechoic Wind Tunnel and Statically with an Inlet Flow Control Device," National Aeronautics and Space Administration Technical Memorandum No. 73723, October 1977.

38. Hodder, Brent K., "An Investigation of Possible Causes for the Reduction of Fan Noise in Flight," AIAA Paper No. 76-585, Third AIAA Aero-Acoustics Conference, Palo Alto, Calif., July 1976.

39. Shaw, Loretta M., private communication, September 1978.

40. Hanson, D. B., "Spectrum of Rotor Noise Caused by Atmospheric Turbulence," _Journal of Acoustical Society of America_, Vol. 56, No. 1, July 1964, pp. 110-126.

41. Lakshminarayana, B., and Davino, R., "Mean Velocity and Decay Characteristics of the Guidevane and Stator Blade Wake of an Axial Flow Compressor," _Journal of Engineering for Power_, Vol. 102, January 1980, pp. 50-60.

42. Barber, T. J., "An Investigation of Strut Wall Intersection Losses," AIAA Paper No. 78-205, AIAA Sixteenth Aerospace Sciences Meeting, January 1978.

43. Hawthorne, W. R., "Secondary Circulation in Fluid Flow," _Proceedings of the Royal Society_, London, England, Series A., Vol. 206, 1951, pp. 374-387.

44. Homicz, G. F., Ludwig, G. R., and Lordi, J. A., "Theoretical and Experimental Studies of Discrete-Tone Rotor-Stator Interaction Noise," AIAA Second Aero-Acoustics Conference, AIAA Paper No. 75-443, March 24-26, 1975.

DISTRIBUTION LIST FOR UNCLASSIFIED TM 80-197, by R. Trunzo, dated 25 September 1980.

Commander
Naval Sea Systems Command
Department of the Navy
Washington, DC 20362
Attn: Library
      Code NSEA-09G32
(Copy Nos. 1 and 2)

Naval Sea Systems Command
Attn: S. M. Blazek
      Code NSEA-05HB
(Copy No. 3)

Naval Sea Systems Command
Attn: H. C. Claybourne
      Code NSEA-05H5
(Copy No. 4)

Naval Sea Systems Command
Attn: F. W. Eissing
      Code NSEA-05H
(Copy No. 5)

Naval Sea Systems Command
Attn: E. G. Liszka
      Code NSEA-63R1
(Copy No. 6)

Naval Sea Systems Command
Attn: T. E. Peirce
      Code NSEA-63R3
(Copy No. 7)

Naval Sea Systems Command
Attn: A. R. Paladino
      Code NSEA-05H1
(Copy No. 8)

Commanding Officer
Naval Underwater Systems Center
Newport, RI 02840
Attn: D. Goodrich
      Code 3634
(Copy No. 9)

Naval Underwater Systems Center
Attn: R. J. Kittredge
      Code 36301
(Copy No. 10)

Naval Underwater Systems Center
Attn: P. Corriveau
      Code 36314
(Copy No. 11)

Commanding Officer
Naval Ocean Systems Center
San Diego, CA 92152
Attn: D. Nelson
      Code 6342
(Copy No. 12)

Commander
David W. Taylor Naval Ship R&D Center
Department of the Navy
Bethesda, MD 20084
Attn: W. K. Blake
      Code 1905
(Copy No. 13)

David W. Taylor Naval Ship R&D Center
Attn: R. W. Brown
      Code 1942
(Copy No. 14)

David W. Taylor Naval Ship R&D Center
Attn: R. A. Cumming
      Code 1544
(Copy No. 15)

David W. Taylor Naval Ship R&D Center
Attn: J. H. McCarthy
      Code 154
(Copy No. 16)

David W. Taylor Naval Ship R&D Center
Attn: T. C. Mathews
      Code 1942
(Copy No. 17)

David W. Taylor Naval Ship R&D Center
Attn: W. B. Morgan
      Code 15
(Copy No. 18)

David W. Taylor Naval Ship R&D Center
Attn: K. D. Remmers
      Code 1942
(Copy No. 19)

David W. Taylor Naval Ship R&D Center
Attn: M. M. Sevik
   Code 19
(Copy No. 20)

David W. Taylor Naval Ship R&D Center
Attn: J. Shen
   Code 194
(Copy No. 21)

David W. Taylor Naval Ship R&D Center
Attn: Code 1505
(Copy Nos. 22 through 36)

David W. Taylor Naval Ship R&D Center
Attn: F. S. Archibald
   Code 1942
(Copy No. 37)

Defense Technical Information Center
5010 Duke Street
Cameron Station
Alexandria, VA 22314
(Copy No. 38)

Dr. A. J. Acosta
Hydrodynamics Lab.
California Institute of Technology
Pasadena, CA 91100
(Copy No. 39)

Mr. A. A. Adamczyk
NASA Lewis Research Center
21000 Brookpark Road
Cleveland, OH 44135
(Copy No. 40)

Dr. H. Atassi
Department of Mechanical and
  Aerospace Engineering
University of Notre Dame
Notre Dame, IN 46556
(Copy No. 41)

Dr. C. Ball
NASA Lewis Research Center
21000 Brookpark Road
Cleveland, OH 44135
(Copy No. 42)

Dr. Tom Booth
93-355-503-4A
Garrett Turbine Engine Company
111 South 34th Street
P.O. Box 5217
Phoenix, AZ 85010
(Copy No. 43)

Dr. Peter Bradshaw
Department of Aeronautics
Imperial College of Science and Technology
London SW7 2AZ, ENGLAND
(Copy No. 44)

Prof. J. Chauvin
Director, Institut de
  Mecanique des Fluides
N° 1, rue Honnart
13003 Marseille, FRANCE
(Copy No. 45)

Dr. James H. Dittmar
MS 501-4
NASA Lewis Research Center
21000 Brookpark Road
Cleveland, OH 44135
(Copy No. 46)

Dr. R. P. Dring
United Technologies Research Lab.
400 Main Street
East Hartford, CT 06108
(Copy No. 47)

Mr. C. Feiler
MS 501-4
NASA Lewis Research Center
21000 Brookpark Road
Cleveland, OH 44135
(Copy No. 48)

Dr. S. Fleeter
Department of Mechanical Engineering
Purdue University
Lafayette, IN 47907
(Copy No. 49)

Prof. H. E. Gallus
Institute for Jet Propulsion
  and Turbomachines
Technical University
Aachen, WEST GERMANY
(Copy No. 50)

DISTRIBUTION LIST FOR UNCLASSIFIED TM 80-197 by R. Trunzo, dated 25 September 1980.

Dr. A. R. George
Sibley School of Mechanical Engineering
Cornell University
Upson Hall
Ithaca, NY 14850
(Copy No. 51)

Mr. Philip R. Gliebe
General Electric Company
Aircraft Engine Group
Cincinnati, OH 45215
(Copy No. 52)

Dr. M. E. Goldstein
NASA Lewis Research Center
MS 301-1
21000 Brookpark Road
Cleveland, OH 44135
(Copy No. 53)

Mr. J. P. Gostelow
Head, School of Mechanical Engr.
The New South Wales Institute
    of Technology
P.O. Box 123
Broadway, N.S.W. 2007
AUSTRALIA
(Copy No. 54)

Dr. E. Greitzer
Gas Turbine Lab.
Room 31-264
Massachusetts Institute of Tech.
Cambridge, MA 02139
(Copy No. 55)

Dr. John Goreneweg
Acoustics Division
NASA Lewis Research Center
21000 Brook Park Road
Cleveland, OH 44135
(Copy No. 56)

Dr. Don Hanson
Mail Stop 1A-3-6
Hamilton Standard
Windsor Locks, CT 06096
(Copy No. 57)

Mr. M. J. Hartmann
NASA Lewis Research Center
21000 Brookpark Road
Cleveland, OH 44135
(Copy No. 58)

Dr. D. Whitehead
Head of Engineering Department
University of Cambridge
Trumpington Street
Cambridge. ENGLAND
(Copy No. 59)

Dr. Loretta M. Shaw
MS 501-4
NASA Lewis Research Center
21000 Brookpark Road
Cleveland, OH 44135
(Copy No. 60)

Dr. W. H. Heiser
General Electric Company
Aircraft Engine Division
Cincinnati, OH 45215
(Copy No. 61)

Dr. H. J. Herring
Dyanalysis
Princeton University
20 Nassau Street
Princeton, NJ 08540
(Copy No. 62)

Dr. C. Hirsch
Faculteit Van de Toegepaste
Wetenschappen
Dienst: Stromingsmechanica
Vrije Universiteit Brussel
Pleinlaan 2
1050 Brussel, BELGIUM
(Copy No. 63)

Dr. G. Homicz
Calspan Corporation
Buffalo, NY 14221
(Copy No. 64)

Dr. J. H. Horlock
Vice-Chancellor
The Open University
Walton Hall
Milton Keynes, MK7 6AA
ENGLAND
(Copy No. 65)

Dr. J. P. Johnston
Stanford University
Mechanical Engineering Department
Stanford, CA 94305
(Copy No. 66)

DISTRIBUTION LIST FOR UNCLASSIFIED TM 80-197 by R. Trunzo dated 25 September 1980.

Dr. J. L Kerrebrock
Director, Gas Turbine Lab.
Massachusetts Institute of Tech.
Room 31-264
Cambridge, MA 02139
(Copy No. 67)

Mr. J. D. Kester
Engineering Building
Pratt & Whitney Aircraft
East Hartford, CT 06108
(Copy No. 68)

Dr. M. Kurosaka
University of Tennessee
Space Institute
Tallahoma, TN 37388
(Copy No. 69)

Dr. J. Mathieu
Lab de Mechanique des Fluides
Ecole Centrale de Lyon
36, Route de Dardilly
69130 Ecully, FRANCE
(Copy No. 70)

Dr. William McNally
NASA Lewis Research Center
21000 Brookpark Road
Cleveland, OH 44135
(Copy No. 71)

Dr. A. A. Mikolaczak
Pratt & Whitney Aircraft
400 Main Street
East Hartford, CT 06118
(Copy No. 72)

Dr. C. L. Morfey
Institute of Sound and Vibration
The University of Southampton
ENGLAND
(Copy No. 73)

Dr. T. H. Okiishi
Dept. of Mechanical Engineering
Iowa State University
Ames, IA 50010
(Copy No. 74)

Dr. K. D. Papailiou
Dept. of Thermal Turbomachines
National Technical University of Athens
42 October 28th Avenue
Athens, GREECE
(Copy No. 75)

Mr. Pramod A. Paranjpe
Head, Propulsion Division
National Aeronautical Lab.
Post Bag No. 1779
Bangalore 560017, INDIA
(Copy No. 76)

Dr. D. C. Prince
Turbomachinery Development Unit
Applied Research Operations
Building 300
General Electric Company
Cincinnati, OH 45215
(Copy No. 77)

Dr. W. C. Reynolds
Dept. of Mechanical Engineering
Stanford University
Stanford, CA 94305
(Copy No. 78)

Dr. Peter Runstadler, Jr.
Creare Inc.
Box 71
Hanover, NH 03755
(Copy No. 79)

Dr. G. K. Serovy
Mechanical Engineering
Iowa State University
Ames, IA 50010
(Copy No. 80)

Dr. L. H. Smith
Turbomachinery Development Unit
Applied Res. Operations Bldg. 300
General Electric Company
Cincinnati, OH 45215
(Copy No. 81)

Mr. P. M. Sockol
Fluid Components Division
NASA Lewis Research Center
21000 Brookpark Road
Cleveland, OH 44135
(Copy No. 82)

Prof. S. Soundranayagam
Mechanical Engineering Department
Indian Institute of Science
Bangalore 560 012, INDIA
(Copy No. 83)

DISTRIBUTION LIST FOR UNCLASSIFIED TM 80-197 by R. Trunzo dated 25 September 1980.

Mr. J. R. Switzer
Garrett Turbine Engine Company
111 South 34 Street
P.O. Box 5217
Phoenix, AZ 85010
(Copy No. 84)

Applied Research Laboratory
Attn: B. Lakshminarayana
(Copy Nos. 95 and 96)

Prof. W. Tabakoff
Dept. of Aerospace Engineering
University of Cincinnati
Cincinnati, OH 45221
(Copy No. 85)

Dr. A. J. Wennerstrom
AFWAL/POTX
Aero Propulsion Lab.
Wright Patterson Air Force Base, OH 45433
(Copy No. 86)

Dr. H. Weyer
Deutsch Forschungs-und
    Versuchsanstalt fur Luft-und
    Raumfahrt E.V.
Institut fur Luftstrohlantriebe
5 Koln 90 - Postfach 906058
WEST GERMANY
(Copy No. 87)

Applied Research Laboratory
The Pennsylvania State University
Post Office Box 30
State College, PA 16801
Attn: R. E. Henderson
(Copy No. 88)

Applied Research Laboratory
Attn: D. E. Thompson
(Copy No. 89)

Applied Research Laboratory
Attn: B. R. Parkin
(Copy No. 90)

Applied Research Laboratory
Attn: W. S. Gearhart
(Copy No. 91)

Applied Research Laboratory
Attn: B. E. Robbins
(Copy No. 92)

Applied Research Laboratory
Attn: G. C. Lauchle
(Copy Nos. 93 and 94)

END

DATE
FILMED

5-81

DTIC